Imaging Novel States in Unconventional Superconductors

BY

MARTIN S GRAHAM

B.S., University of Illinois at Urbana-Champaign, 2013

M.S., Ohio University, 2015

THESIS

Submitted as partial fulfillment of the requirements for the degree of

Doctor of Philosophy in Physics in the Graduate college

of the University of Illinois at Chicago, 2020

Chicago, Illinois

Defense Committee:

      Dirk Morr, Chair and Advisor

      Hyowon Park

      Mark Schlossman

      Mikhail Stephanov

      Petr Král, Chemistry

Acknowledgements

Contribution of Authors

In the following work, Chapter 1 presents a brief overview of the topics in the thesis. Chapter 2 is based on the published manuscript: M. Graham and D. K. Morr, "Imaging the spatial form of a superconducting order parameter via Josephson scanning tunneling spectroscopy," Physical Review B, vol. 96, no. 18, pp. 1-7, 2017. M. G. performed the calculations and D.K. supervised the project. Chapter 3 is based on the published manuscript: M. Graham and D. K. Morr, "Josephson scanning tunneling spectroscopy in $d_{x^2-y^2}$-wave superconductors: A probe for the nature of the pseudogap in the cuprate superconductors," Phys. Rev. Lett., vol. 123, p. 017001, Jul 2019. M. G. performed the calculations and D. K. M. supervised the project. Chapter 4 is based on the unpublished manuscript: E. Mascot, J. Bedow, M. Graham, S. Rachel, and D. K. Morr, "Topological superconductivity in skyrmion lattices," 2020. E. M. finalized the model and performed topological phase, band structure, and LDOS, supercurrent, and superconducting correlation calculations. J. B. performed topological phase and band structure calculations. M. G. performed LDOS, superconducting correlation, and critical Josephson current calculations. D. K. M. supervised the project. Chapter 5 is based on two manuscripts. The first is published as: Z. Wang, J. O. Rodriguez, L. Jiao, S. Howard, M. Graham, G. D. Gu, T. L. Hughes, D. K. Morr, and V. Madhavan, "Evidence for dispersing 1D Majorana channels in an iron-based superconductor," Science, vol. 367, no. 6473, pp. 104–108, 2020. Z. W., J. O. R., L. J., and S. H. performed the experimental

measurements. M.G. performed the numerical calculations discussed in the text. G. D. G, T. H., D. K. M. supervised the project. The second is an unpublished manuscript by S. Cocklin, M. Graham, E. Mascot, S. Rachel, and D. K. Morr. S. G. performed the phase diagram calculations. M. G. performed the domain wall calculations. D. K. M. supervised the project.

TABLE OF CONTENTS

List of Tables

List of Figures

Abbreviations

BCS Bardeen-Cooper-Schrieffer

DOS density of states

DW domain wall

FFLO Fulde-Ferrel-Larkin-Ovchinnikov

FFT fast Fourier transform

FOV field of view

JSTS Josephson scanning tunneling spectroscopy

LDOS local density of states

MSH magnetic hybrid superconductor

STM scanning tunneling microscopy

STS scanning tunneling spectroscopy

Summary

A comparison of simulated Josephson scanning tunneling current against spatial superconducting order parameter fluctuations was performed in the context of several distinct superconducting models. In each case, the Josephson current was calculated using a Keldysh Green's formalism to first-order in the superconductor-tip tunneling. In the case of an isotropic s-wave superconductor, the atomically-resolved superconducting correlations were self-consistently calculated to produce fluctuations consistent with magnetic and non-magnetic impurities. These characteristic fluctuations were imaged by the Josephson critical current.

For a $d_{x^2-y^2}$-symmetric superconductor, the nonlocal nature of superconductivity dictated a spatially-extended superconducting tip. Investigating the spatial extent and possible disorder of the superconducting tip demonstrated that these variations did not qualitatively change the ability of the Josephson critical current to image the $d_{x^2-y^2}$-wave superconducting correlations. In addition, the high resolution of the imaging ability of JSTS allowed for identification of the Fulde-Ferrel-Larkin-Ovchinnikov phase, and its sensitivity to superconducting correlations allowed it to predict a signature for a precursor pairing-mediated pseudogap phase based on a realistic model of inhomogenous superconducting and pseudogapped regions.

In a skyrmion system, the rich phase diagram obtained through the combination of skyrmion magnetic moments and induced Rashba spin-orbit coupling

was demonstrated. In that system, topological superconductivity was visualized as p-wave spin-triplet superconducting correlations. Using an extended tip with corresponding spin-triplet correlations, a Josephson critical current was measured that identified regions with spin-triplet superconductivity in a phase- and spatially-resolved way.

In the context of topological superconductivity in an $FeSe_{0.45}Te_{0.55}$-hosted domain wall with a possible a Majorana zero mode, a 5-band model was constructed. When topologically trivial, the 5-band model of $FeSe_{0.45}Te_{0.55}$ was demonstrated to be incapable of matching experimental evidence for a zero-energy mode arising for either a step-edge commensurate domain wall or a domain wall with a half-unit cell shift. Revising the topologically trivial model using surface magnetism and the Rashba spin-orbit effect produced the necessary topological superconductivity in $FeSe_{0.45}Te_{0.55}$. In this revised model, detection of a Majorana zero mode using scanning tunneling spectroscopy was compared to a method of detection using equilibrium current measurement, with the latter demonstrating qualitatively different results in the presence of a Majorana zero mode.

Chapter 1

Introduction

In s-wave superconductors, the explanation of superconductivity in terms of charge screening and an electron-phonon interaction leads us to suppose that its origin in high-temperature superconductors may have an intuitive underlying mechanism as well. This tantalizing possibility, coupled with the advantages a high-temperature superconductor could bring, has led to intense research into how "unconventional" high-temperature superconductors behave, and is a key factor motivating our models of a copper-oxide (Chapter 3) and iron-pnictide (Chapter 5) superconductor. For these materials, the usual isotropic s-wave symmetry of superconductivity no longer holds – in the iron pnictide $FeSe_xTe_{1-x}$, a spin-fluctuation between nearly nested hole-like and electron-like Fermi surfaces leads to a sign-changing s-wave symmetry[1]. In the high-temperature copper-oxide (cuprate) superconductor $YBa_2Cu_3O_{7-\delta}$, we have learned that superconductivity has a $d_{x^2-y^2}$ symmetry[2] based on a phenomenon with unique insight into the pair correlations responsible for superconductivity – the Josephson effect[3]. This crucial connection between superconductivity's pair correlations and a Josephson effect-derived observable is the one of the key ideas we investigate in the following text.

As Bardeen, Cooper, and Shrieffer's model[4] demonstrated, an arbitrarily weak

e-e attraction will couple electrons into Cooper pairs at low temperatures, resulting in a gapped ground state, superconductivity, and a built-in way to describing the resulting electron-pair correlations in terms of a superconducting order parameter (SCOP). However, despite the fact that the SCOP underlies the electronic definition of superconductivity and its spatially averaged magnitude even appears as the superconducting gap, it could not be directly measured until the discovery of the Josephson effect.

In the Josephson effect, a persistent current is predicted to be present between two superconducting electrodes coupled by an insulating link even in the absence of an applied voltage[5]. The simplest example of this effect occurs when the two electrodes are embedded on a substrate in a Josephson junction (the method used in the discovery of $d_{x^2-y^2}$ symmetry in YBa$_2$Cu$_3$O$_{7-\delta}$), where the flow of current is governed by the Josephson equations,

$$I_S = I_C \sin \Delta\psi \tag{1.1}$$

$$\frac{d\Delta\psi}{dt} = \frac{2eV}{\hbar} \tag{1.2}$$

Here, I_S represents the Josephson current, I_C the maximum current the link can support, known as the critical current, V is the voltage across the junction, and $\Delta\psi = \psi_L - \psi_R$ is the difference in the phases of the SCOP's between the left and right sides of the junction[3, 5].

In a Josephson scanning tunneling spectroscopy (JSTS) configuration (see Fig. 1.1), a superconducting tip separated from a superconducting substrate by a small air gap exhibits the Josephson effect in a different way than a junction. In our results for a single- or multi-atomic JSTS tip, the form of Eq. 1.1 changes (see for example Eq. 2.1) to reflect the atomic geometry of the tunneling sites. Instead of the broad tunneling interface provided by the terminals of a junction, the atomic
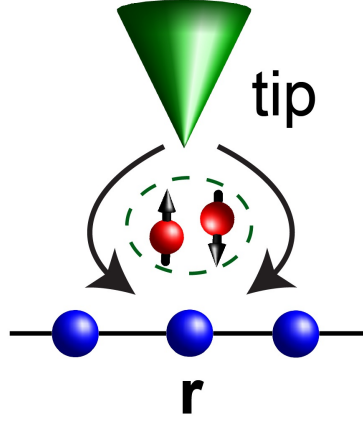
Figure 1.1: Schematic tunneling picture of a superconducting tip at site r above the system.

tip in JSTS allows for a measurement of I_C with up to atomic precision[6]. In addition, in a similar way as scanning tunneling microscopy, Josephson scanning tunneling spectroscopy (JSTS) experiments (see for example [7, 8, 9]) produce a spatial current distribution that – as we will show – images the spatial superconducting correlations in a superconductor. In this respect, JSTS may be contrasted with electron scanning tunneling spectroscopy (STS), where it is possible to extract a gapmap from the coherence peaks in a measurement of the single-particle dI/dV. Although these techniques can provide superficially similar measurements, the gap obtained from measuring superconducting coherence peaks in STS does not typically reflect the atomically-resolved variations of the SCOP[10, 11, 12]. On the other hand, JSTS is a probe of the SCOP with atomic resolution as well as a complex phase. In the results we present in Chapters 1-3 we use these unique features of JSTS to identify novel phenomena like the long-sought Fulde-Ferrel-Larkin-Ovchinnikov[13, 14] phase in cuprate superconductors and the emergence of the spin-triplet superconducting correlations essential for the presence of topological superconductivity.

In a topological superconductor, the bulk of the superconductor is characterized by a topological invariant based on the dimensions and symmetries of the

material[15]. Furthermore at the superconductor's edge, the change in its topological invariant produces a gapless boundary state (a result known as the bulk-boundary correspondence)[16]. Research into topological superconductivity exploded after Alexei Kitaev pointed out that a topologically superconducting 1D chain of atoms[17] is able to host a collective electronic state at zero energy (a Majorana zero mode) at its ends that is protected from decoherence by its topological phase, making it ideal for a qubit used in quantum computing. To make useful qubits, however, they must be manipulable – a feat hard to accomplish in a topological bulk-boundary mode where the topological phase is determined by a material's inaccessible bulk. As we show, however, a skyrmion lattice (see Chapter 4) offers the capability to tune between topological phases. Furthermore, $FeSe_xTe_{1-x}$ has emerged as a rare material capable of hosting these exotic topological zero-energy modes[18]. The ambiguity surrounding the microscopic origin and experimental detection of Majorana zero modes, however, has led us–in chapter 5–to extend previous efforts[19, 20] to model the electronic structure of $FeSe_{0.45}Te_{0.55}$ with the goal of identifying a domain wall-localized Majorana zero mode in this system.

Investigating the topics detailed in the following chapters has lead to some interesting results, but also many more interesting questions. We hope, however, that the results we present will provide some insight into the incredible potential offered by transport experiments on unconventional superconductors.

Chapter 2

Josephson spectroscopy in an s-wave superconductor

This work was previously published as: M. Graham and D. K. Morr, "Imaging the spatial form of a superconducting order parameter via Josephson scanning tunneling spectroscopy," Physical Review B, vol. 96, no. 18, pp. 1-7, 2017.

2.1 Introduction to Josephson scanning tunneling spectroscopy

As we recall from Chapter 1, the Josephson effect in a superconductor-insulator-superconductor junction led to the following equations,

$$I_S = I_C \sin \Delta\psi \tag{2.1}$$

$$\frac{d\Delta\psi}{dt} = \frac{2eV}{\hbar} \tag{2.2}$$

Here, I_S represents the Josephson current, I_C the maximum current the link can support, known as the critical current, and $\Delta\psi = \psi_L - \psi_R$ the difference in

the phases of the SCOP's between the left and right sides of the junction [3, 5].
Shortly after Josephson's 1962 paper, Ambegaokar and Baratoff[21] connected
the Josephson current I_S in Eq. (1.1) to the magnitude of the superconducting
order parameter. In their result for a system of two symmetric superconductors
connected by a weak link, they found[22],

$$I_c R_n = (\pi\Delta/2e)\tanh(\Delta/2kT) \tag{2.3}$$

This general result for a Josephson junction showed that the critical Josephson
current I_C scales linearly with the SCOP at increasing temperatures, and, more-
over, is proportional to the magnitude of the SCOP at $T = 0$[5].

Motivated by the general result in Eq. 2.3 for a junction, the assumption that
the Josephson current produced at zero bias in superconducting STM will im-
age the magnitude of the SCOP has been used extensively in recent experiments
[23, 7, 24, 25, 26, 27]. However, while the ability of the Josephson effect to pro-
vide information about a system's SCOP is well-established, the correspondence
between the tunneling current in an STM configuration and the magnitude of varia-
tions in the substrate SCOP is in general not understood. To resolve this ambiguity
and as a building block to considering more complex systems, this chapter studies
the correspondence between the JSTS critical current and the SCOP with a s-wave
superconductor, which can already host atomic-scale fluctuations in the SCOP as
a result of impurity scattering[28] that are in general invisible from regular STS
measurements[10].

2.2 Constructing a model superconductor

The starting point for investigating the relation between the spatial form of the critical Josephson current and the superconducting order parameter around defects in an s-wave superconductor is the Hamiltonian $H = H_{\text{S}} + H_{\text{tip}} + H_{\text{tun}}$ where,

$$H_S = -t \sum_{\langle \mathbf{r},\mathbf{r'} \rangle,\sigma} c_{\mathbf{r}\sigma}^\dagger c_{\mathbf{r'}\sigma} - \mu \sum_{\mathbf{r},\sigma} c_{\mathbf{r}\sigma}^\dagger c_{\mathbf{r}\sigma} - \sum_{\mathbf{r}} \left(\Delta(\mathbf{r}) c_{\mathbf{r}\uparrow}^\dagger c_{\mathbf{r}\downarrow}^\dagger + \text{h.c.} \right) \quad (2.4)$$

$$+ \sum_{\mathbf{R},\alpha,\beta} (U_0 \hat{1}_{\alpha\beta} + J_0 \sigma_{\alpha\beta}^z) c_{\mathbf{R}\alpha}^\dagger c_{\mathbf{R}\beta} \quad (2.5)$$

Here, $-t$ is the electronic hopping between nearest-neighbor sites $\mathbf{r}$ and $\mathbf{r_0}$, μ is the chemical potential, and $c_{\mathbf{r}\sigma}^\dagger$ ($c_{\mathbf{r}\sigma}$) creates (annihilates) an electron with spin σ at site $\mathbf{r}$. $\Delta(\mathbf{r})$ is the superconducting order parameter with s-wave symmetry at site $\mathbf{r}$ in the superconductor and U_0 and J_0 are the non-magnetic and magnetic scattering strengths of a defect located at site $\mathbf{R}$, with the last sum running over all defect sites.

Unless otherwise noted, we set $\mu = -3.618t$, yielding the circular Fermi surface shown in Fig. 2.1. In the presence of defects, we self-consistently compute the local superconducting order parameter in the superconductor using

$$\Delta(\mathbf{r}) = -\frac{V_0}{\pi} \int_{-\infty}^{\infty} d\omega n_F(\omega) \text{Im}[F_s(\mathbf{r},\mathbf{r},\omega)] \quad (2.6)$$

where V_0 is the superconducting pairing potential, $n_F(\omega)$ is the Fermi distribution function, and $F_S(\mathbf{r},\mathbf{r},\omega)$ is the local, retarded anomalous Green's function of the s-wave superconductor. We model the JSTS tip as an atomically sharp site, described by the Hamiltonian $H_{\text{tip}} = H_{\text{tip}}^n + H_{\text{tip}}^{\text{SC}}$, where H_{tip}^n represents the normal
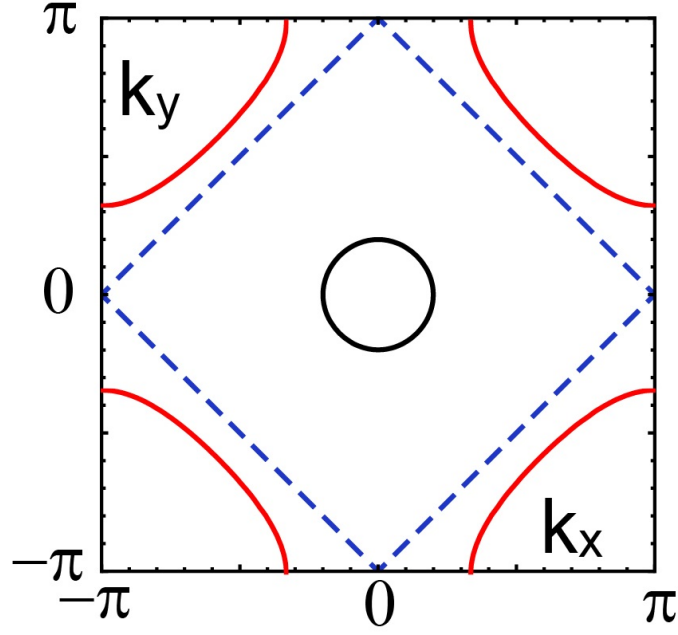
Figure 2.1: Fermi surfaces representing several different electronics structures, with $\mu = t$ (red), $\mu = 0$ (dashed blue), $\mu = -3.618t$

state electronic structure of the tip, and

$$H_{\text{tip}} = -\Delta_{\text{tip}} d_\uparrow^\dagger d_\downarrow^\dagger - \Delta_{\text{tip}} d_\downarrow d_\uparrow$$

its superconducting correlations. Here, Δ_{tip} is the superconducting s-wave gap in the tip and $d_\sigma^\dagger$ (d_σ) creates (annihilates) an electron with spin σ in the tip. Finally, the tunneling of electrons between the tip and a site $\mathbf{r}$ in the s-wave superconductor is described by

$$H_{\text{tun}} = -t_0 \sum_\sigma (c_{\mathbf{r}\sigma}^\dagger d_\sigma + d_\sigma^\dagger c_{\mathbf{r})\sigma}$$

2.3   Definition of Green's functions in real space

To compute the spatial dependence of the local s-wave order parameter, $\Delta(\mathbf{r})$, as
well as the critical Josephson current, $I_C(\mathbf{r})$, in the presence of defects, we rewrite
the Hamiltonian in Eq. 2.4 in matrix form by introducing the spinor

$$\Psi^\dagger = \left(c_{1\uparrow}^\dagger, c_{1\downarrow}, ..., c_{i\uparrow}^\dagger, c_{i\downarrow}, ..., c_{N\uparrow}^\dagger, c_{N\downarrow} \right) \tag{2.7}$$

where N is the number of sites in the s-wave superconductor, and $i = 1, ..., N$ is
the index for a site $\mathbf{r}$ in the system. The Hamiltonian in Eq. 2.4 can then be written
as,

$$H_S = \Psi^\dagger \hat{H}_s \Psi$$

We define a retarded Green's function matrix of the system via,

$$\hat{G}_{SC}(\omega + i\delta) = \left[(\omega + i\delta)\hat{1} - \hat{H}_s \right]^{-1}$$

where $\hat{1}$ is the $(N \times N)$ identity matrix and $\delta = 0^+$. The local anomalous Green's
function at site $\mathbf{r}$ (with index i), $F_s(\mathbf{r}, \mathbf{r}, \omega)$, is then given by the $(2i - 1, 2i)$ element of
$\hat{G}_s$ corresponding to the Fourier transform of $-\langle T c_{i\uparrow}(\tau) c_{i\downarrow}(0) \rangle$. Moreover, we take
the anomalous Green's function of the tip (which will enter the Josephson current
in Eq. 2.11) to be that of a bulk system given by

$$F_t(\omega) = -N_0 \Delta_{tip} \frac{\pi i}{\sqrt{(\omega + i\delta)^2 - \Delta_{tip}^2}} \mathrm{sgn}(\omega) \tag{2.8}$$

where N_0 is the density of states in the tip. This form implies that F_t possess
a non-zero real part only for $|\omega| < \Delta_{tip}$, and a non-zero imaginary part only for

$|\omega| > \Delta_{tip}$.

2.4 Extraction of Josephson current

A DC Josephson current [3] arises from a phase difference between the super-
conducting order parameters of the tip and the s-wave superconductor, described
by

$$\Delta(\mathbf{r}) = |\Delta(\mathbf{r})|e^{i\Phi_s} \qquad \Delta_{tip} = |\Delta_{tip}|e^{i\Phi_t} \qquad (2.9)$$

This phase difference can be gauged away [29], yielding a tunneling parameter
that depends on the phase difference

$$t_0 \rightarrow t_0 e^{i(\Phi_s - \Phi_t)/2} = t_0 e^{i\Delta\Phi/2} \ . \qquad (2.10)$$

allowing us to take $\Delta(\mathbf{r})$ and Δ_t as real parameters below. In the self-consistent
solution of Eq.(2.6), we therefore assume that the phase of $\Delta(\mathbf{r})$ does not vary,
and consider only spatial variations in its magnitude. Using the Keldysh Green's
function formalism [30, 31], we then obtain that the DC-Josephson current between
the tip and a site $\mathbf{r}$ in the s-wave superconductor to lowest order in the hopping t_0
(i.e., in the weak-tunneling limit) is given by [29]

$$I_J(\mathbf{r}) = 8\frac{e}{\hbar}t_0^2 \sin\left(\Delta\Phi\right) \int \frac{d\omega}{2\pi} n_F(\omega)\mathsf{Im}[F_s(\mathbf{r},\mathbf{r},\omega)F_t(\omega)] \qquad (2.11)$$

$$\equiv I_c(\mathbf{r})\sin\left(\Delta\Phi\right) \qquad (2.12)$$

where F_t is the retarded anomalous Green's function of the tip, I_c is the critical
Josephson current, and we set $T = 0$ below. In the weak-tunneling limit, possible
effects of the JSTS tip on $\Delta(\mathbf{r})$ can be neglected. While current JSTS experiments
can only measure the magnitude of $I_c(\mathbf{r})$, future advances could open the possibil-
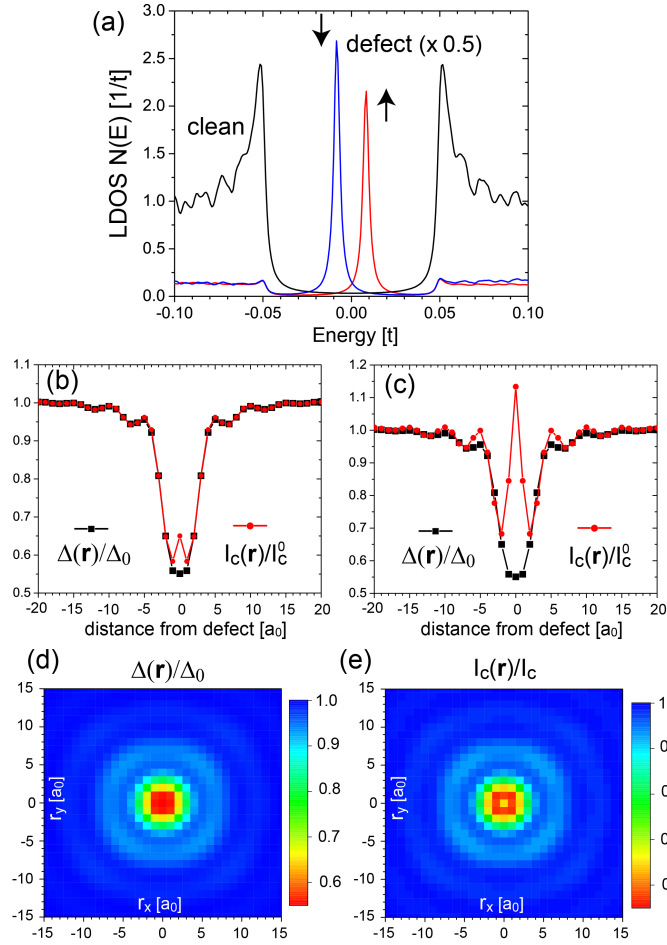
Figure 2.2: a.) spin-selective LDOS taken at $\mathbf{r} = (+1, 0)$ away from a magnetic defect of magnitude $\mathbf{J} = 2t$. The substrate is a 401x401 s-wave superconductor with a gap $\Delta_0 = 0.05t$. $\Delta(\mathbf{r})$ and I_C are calculated along the x-axis for $\Delta_{\text{tip}} = 4.0\Delta_0$ and $\Delta_{\text{tip}} = 0.5\Delta_0$ in (b) and (c), respectively. (d) presents the normalized spatial dependence of $\Delta(\mathbf{r})$ and (e) of $I_C(\mathbf{r})$ for $\Delta_{\text{tip}} = 5.0\Delta_0$

ity to measure $I_J(\mathbf{r})$ as well, providing insight into spatial variations of $\Delta\Phi$.

2.5 Magnetic point defects

Magnetic and non-magnetic defects exert qualitatively different effects on an s-wave superconductor: the former induce impurity bound states inside the super-conducting gap - Shiba states [32, 33, 34] - while the latter do not. Nevertheless, the spatial oscillations in the superconducting order parameter, $\Delta(\mathbf{r})$, induced by

either type of defect, can be imaged through the critical Josephson current $I_c(\mathbf{r})$,
as shown below. Moreover, the presence of Shiba states results in a characteristic
signature in $I_c(\mathbf{r})$ that allows one to distinguish between these two types of defects.

To demonstrate this, we begin by considering the spatial form of $\Delta(\mathbf{r})$ and of
$I_c(\mathbf{r})$ around a magnetic defect. In Fig. 2.2(a), we present the local density of
states (LDOS) in the vicinity of the defect together with that in a clean system.
The magnetic defect induces, as expected an impurity (Shiba) state inside the su-
perconducting gap, whose particle- and hole-like branches possess well-defined,
but opposite spin-polarizations. In Fig. 2.2(b), we present the normalized super-
conducting order parameter, $\Delta(\mathbf{r})/\Delta_0$, and the Josephson current, $I_c(\mathbf{r})/I_c^0$ along
$r_y = 0$ for $\Delta_{tip} = 4\Delta_0$. Here, Δ_0 and I_c^0 are the superconducting order parameter
and the critical Josephson current in a clean system. The defect-induced oscilla-
tions of $\Delta(\mathbf{r})$ are very well spatially imaged by the Josephson current, despite the
very rapid oscillations of the former around the defect. This result theoretically con-
firms the assumption underlying the JSTS experiments by Hamidian *et al.*, [7] and
Randeria *et al.* [23]. To gain analytic insight into the spatial relation between $\Delta(\mathbf{r})$
and $I_c(\mathbf{r})$, we consider the limit of large tip gap $\Delta_{tip} > \omega_D$ where ω_D is the Debye
energy of the s-wave superconductor. In this case, we have for the integrand in
Eq. (2.11), $\mathrm{Im}[F_s\, F_t] = \mathrm{Re}F_t \mathrm{Im}F_s$, and $\mathrm{Re}F_t(\omega)$ can be approximated by a constant
$\mathrm{Re}\bar{F}_t$ over the energy range where $\mathrm{Im}F_s$ possesses the largest spectral weight (see
Fig. 2.3.

Using Eq.(2.6) we then obtain from Eq.(2.11)

$$I_c(\mathbf{r}) \sim \mathrm{Re}\bar{F}_t \int \frac{d\omega}{2\pi} n_F(\omega)\mathsf{Im}[F_s(\mathbf{r},\mathbf{r},\omega)] \sim \Delta(\mathbf{r}) \,. \tag{2.13}$$

Thus, $I_c(\mathbf{r})/I_c^0 = \Delta(\mathbf{r})/\Delta_0$, and $I_c(\mathbf{r})$ possesses in general the same spatial de-
pendence as $\Delta(\mathbf{r})$. There exists, however, an interesting exception to this result at
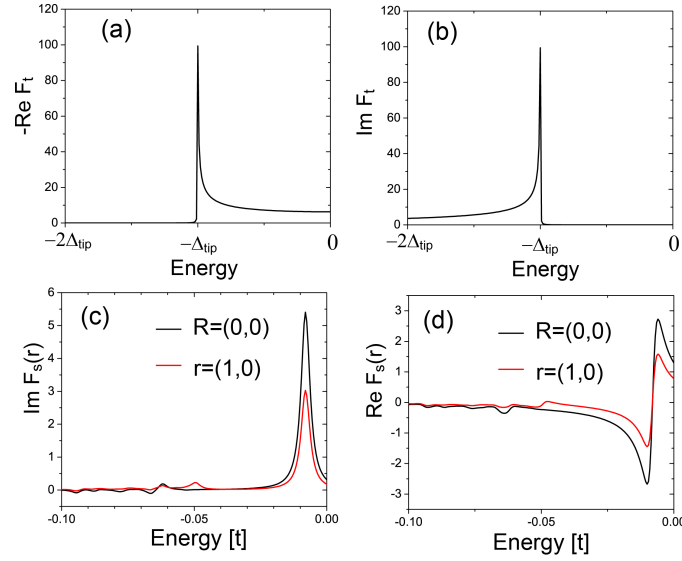
Figure 2.3: Anomalous Green's functions in the integrand of Eq.(2.11), calculated at a distance $\mathbf{r} = (+1, 0)$ from a $J = 2t$ magnetic defect. (a) $-\text{Re}[F_t(\omega)]$, (b) $\text{Im}[F_t(\omega)]$, (c) $\text{Im}[F_s(\mathbf{r}, \omega)]$, (d) $\text{Re}[F_s(\mathbf{r}, \omega)]$.

the site of the magnetic defect, where $I_c(\mathbf{r})$ exhibits a weak peak while $\Delta(\mathbf{r})$ does

not [see Fig. 2.2(b)]. This peak arises from an enhanced tunneling of Cooper pairs

from the tip into the Shiba state, whose largest spectral weight resides at the site of

the defect, and thus counteracts the general suppression of $\Delta(\mathbf{r})$ in the vicinity of

the defect. As the main contribution to this peak arises from $\text{Re}[F_t]\text{Im}[F_s]$ in the in-

tegral of Eq. (2.11) (see Fig. 2.3), we expect that the peak height further increases

as Δ_{tip} (and hence the enhancement of $\text{Re}[F_t]$ near Δ_{tip}) approaches the energy

of the Shiba state. This expectation is borne out by our results for a smaller tip gap

$\Delta_{tip} = 0.5\Delta_0$ [see Fig. 2.2(c)], which shows an even stronger enhancement of the

peak in I_c near the defect. This peak in I_c is therefore a direct signature of the im-

purity induced Shiba state and thus absent for non-magnetic defects (see below).

The peak's height is not only affected by the value of Δ_{tip}, but also the strength of

the magnetic scattering as well as the electronic structure of the superconductor.

However, even in presence of a strong peak in I_c at the defect site, the spatial de-

pendence of I_c in all other regions still reflects that of $\Delta(\mathbf{r})$. This is also confirmed
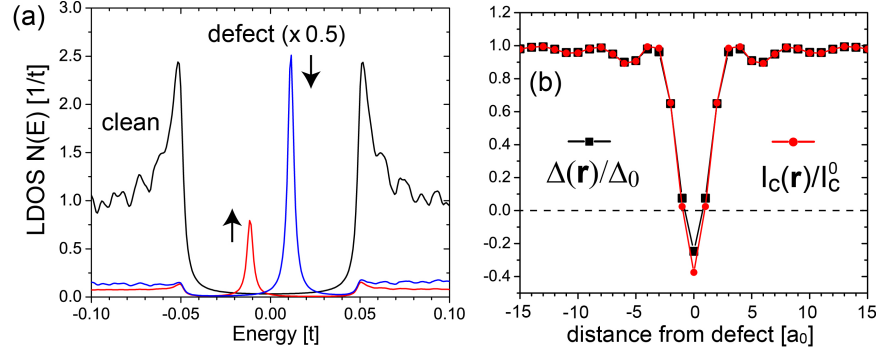
Figure 2.4: a.) Shiba states in a system with $J = 2.5t$ b.) $\Delta(\mathbf{r})$ and I_C calculated along the x-axis in a system with $\Delta_{\text{tip}} = 4.0\Delta_0$, showing a sign change at the site of the magnetic defect.

by the spatial plots of the normalized $\Delta(\mathbf{r})$ and $I_c(\mathbf{r})$, shown in Figs. 2.2(d) and (e), respectively. Here, the spatially circular oscillations in $\Delta(\mathbf{r})$ and of $I_c(\mathbf{r})$ reflect the form of the underlying circular Fermi surface [see Fig. 2.1], with their wavelength of $\lambda_F/2$ arising from $2k_F$ scattering.

As the magnetic scattering strength, J_0, is increased and exceeds a critical value, J_c, the superconductor undergoes a phase transition in which its ground state changes from a singlet $S = 0$ state to a doublet $S = 1/2$ state [35, 36, 37, 28]. Simultaneous with this phase transition, the particle- and hole-like branches of the Shiba state cross at zero energy [34], and the superconducting order parameter changes sign at the site of the defect [36, 37, 28]. A comparison of the LDOS near a magnetic defect with $J_0 = 2.5t > J_c$ in Fig. 2.4(a) with the LDOS for $J_0 = 2.0t < J_c$ in Fig. 2.2(a) shows that the two branches of the Shiba state have crossed zero energy, as the particle-like (hole-like) branches for $J_0 < J_c$ and $J_0 > J_c$ possess different spin character.

Moreover, the sign of the superconducting order parameter changes at the site of the defect [see Fig. 2.4(b)], which is mirrored by a sign change in the Josephson current. This sign change in I_c as a function of distance from the defect is a direct signature of the $S = 1/2$ ground state of the superconductor. While current JSTS

experiments can only measure the magnitude of I_c, they can still detect the $S =$
$1/2$ ground state, as $|I_c|$ would exhibit a line of zeros around the defect, which
is qualitatively different from the from of I_c shown in Figs. 2.2(b) and (c). Thus,
the spatial form of the Josephson current not only reflects that of $\Delta(\mathbf{r})$, but it is
also a probe for the spin ground states of the superconductor, and hence can
be employed to detect a quantum phase transition of the system. This opens up
the possibility to investigate more complex ground states with even larger spin
polarizations, as arise, for example, from quantum interference effects in multi-
defect systems [37].

2.6   Non-magnetic scattering defects

In contrast to magnetic defects, non-magnetic (potential) defects do not induce
impurity states inside the superconducting gap [38], as follows from a plot of the
LDOS near the site of a repulsive potential defect with $U_0 = 2t$ in Fig. 2.5(a). How-
ever, the scattering off non-magnetic defects induces oscillations in the electron
charge density, n_e, [Fig. 2.5(b)] which in turn give rise to spatial variations of the
superconducting order parameter [Figs. 2.5(c) and (d)].

   While magnetic defects lead to an overall suppression of the superconduct-
ing order parameter, non-magnetic defects, through oscillations in $n_e(\mathbf{r})$, give rise
to spatial regions in which $\Delta(\mathbf{r})$ is enhanced or suppressed. These spatial oscil-
lations can again be imaged by the Josephson current, as demonstrated by the
spatial contour plots of $\Delta(\mathbf{r})$ and $I_c(\mathbf{r})$ in Fig. 2.5(d) and (f), respectively, and the
line cut in Fig. 2.5(c). Due to the absence of a Shiba state, the tunneling of Cooper
pairs from the tip into the superconductor is not enhanced at the site of the defect,
and no peak in I_c is therefore found. Moreover, a non-magnetic defect with an
attractive scattering potential, $U_0 = -0.5t$, leads to an enhancement of the charge
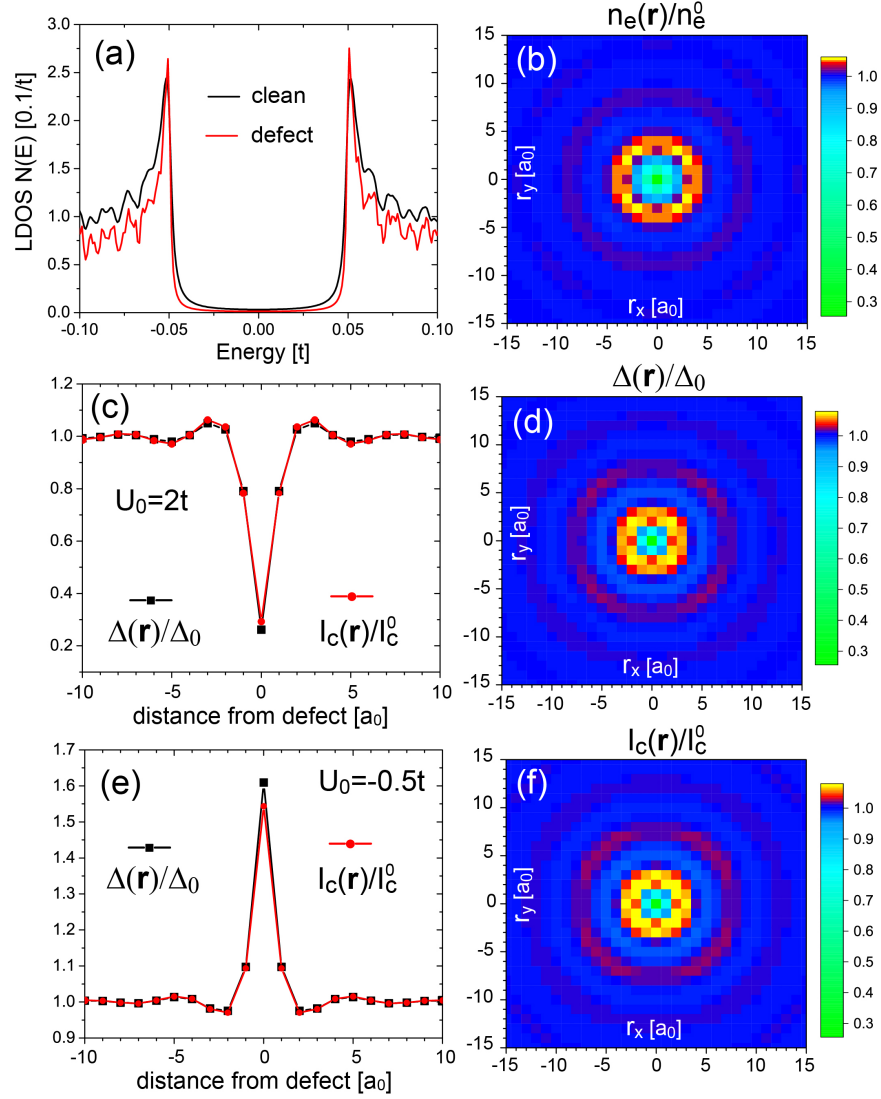
Figure 2.5: (a) LDOS at a distance $r = (+1, 0)$ from a potential defect with a repulsive scattering potential $U_0 = 2t$. (b), (d), and (f) present contour plots of the charge density $n_e(\mathbf{r})/n_e^0$, $\Delta(\mathbf{r})/\Delta_0$ and $I_C(\mathbf{r})/I_C^0$, respectively. (c) and (e) present a spatial cut of $\Delta(\mathbf{r})/\Delta_0$ and $I_C(\mathbf{r})/I_C^0$ along the $\mathbf{r} = (+\hat{x}, 0)$ direction for $\Delta_{\text{tip}} = 4\Delta_0$ and $U_0 = 2t$ (c) and $U_0 = -0.5t$ (e).
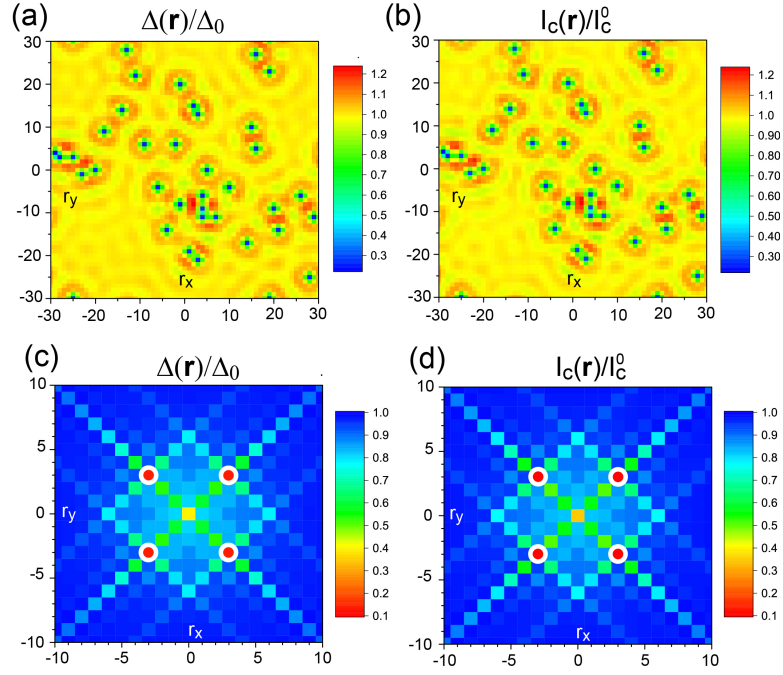
Figure 2.6: (a) $\Delta(\mathbf{r})/\Delta_0$ and (b) $I_C(\mathbf{r})/I_C^0$ for a 1% concentration of randomly distributed defects of magnitude $U_0 = 2t$. (c) $\Delta(\mathbf{r})/\Delta_0$ and (d) $I_C(\mathbf{r})/I_C^0$ for a configuration of four magnetic defects of magnitude $J_0 = t$, $\Delta_{\text{tip}} = 4\Delta_0$, $\mu = 0$

density and hence the superconducting order parameter near the defect that is also

reflected in the spatial form of $I_c(\mathbf{r})$ [see Fig. 2.5(e)]. Thus, the enhancement or de-

crease of the critical current in the vicinity of a non-magnetic defect can distinguish

between its attractive and repulsive scattering potential.

The ability to image spatial oscillations of the superconducting order parameter

via I_c are independent of the particular form of the material's Fermi surface or the

strength of the scattering potential. Moreover, $\Delta(\mathbf{r})$ can not only be mapped around

isolated defects, as discussed above, but also in disordered superconductors with

a random distribution of defects [9], as shown in Figs. 2.6(a) and (b). Here, we

present $\Delta(\mathbf{r})/\Delta_0$ and of $I_c(\mathbf{r})/I_c^0$, respectively, for a concentration of 1% randomly

distributed non-magnetic defects with $U_0 = 2t$.

While the interference of electrons scattered by multiple defects can lead to spa-

tial regions in which the superconducting order parameter is significantly enhanced

or suppressed, the spatial form of $I_c(\mathbf{r})$ again very well images that of $\Delta(\mathbf{r})$. The
critical Josephson current can even be employed to image "virtual defects", i.e., re-
gions in which the superconducting order parameter is strongly suppressed without
the existence of defects. Such virtual defects can be created using quantum inter-
ference effects, as shown in Fig. 2.6(c), where we present the superconducting
order parameter in the presence of four defects located at sites denoted by white
open circles and $\mu = 0$, yielding the dashed blue Fermi surface in Fig. 2.1. Inter-
ference effects give rise to an additional strong suppression of $\Delta(\mathbf{r})$ in the center
of the superconductor – the virtual defect – which is again captured by $I_c(\mathbf{r})$, as
shown in Fig. 2.6(d).

Throughout this chapter, we have demonstrated that the Josephson critical cur-
rent images the spatial dependence of the superconducting order parameter. In
the case of magnetic defects, this picture is slightly complicated by the appear-
ance of Shiba states; however, these are identifiable by a specific signature in both
the LDOS and a JSTS current map. The consistency of I_C calculations compared
to the order parameter throughout the varied s-wave systems we consider should
provide some reassurance that the experimental measurements of $|I_C|$ do, indeed,
correspond to short length-scale fluctuations in the SCOP. Although the discussion
throughout this chapter has been limited to BCS-type, isotropic superconductors, it
sets the stage to investigate Josephson tunneling in more complex unconventional
systems where, in some cases, even the microscopic origin of superconductivity
remains a mystery.

Chapter 3

Josephson spectroscopy in cuprate superconductors

This work was previously published as: M. Graham and D. K. Morr, "Josephson scanning tunneling spectroscopy in $d_{x^2-y^2}$-wave superconductors: A probe for the nature of the pseudogap in the cuprate superconductors," Phys. Rev. Lett., vol. 123, p. 017001, Jul 2019.

3.1   A nonlocal probe of the order parameter

Copper oxide-based superconductors, known as cuprates, are a class of widely-used unconventional superconductors that host many interesting microscopic properties.

Recent experiments [7, 39, 27] have performed Josephson scanning tunneling spectroscopy (JSTS) on this class of unconventional superconductors, with the intent of exploring the microscopic properties of the superconducting order parameter. The application of JSTS to cuprate superconductors specifically offers the unique possibility of exploring the magnetic-field induced Fulde-Ferrel-Larkin-

Ovchinnikov (FFLO) phase [13, 14, 40, 41, 42]. Although the presence of a FFLO phase has been proposed in several compounds, particularly in strongly type-II superconductors where Pauli paramagnetic pair-breaking suppresses superconductivity[42], most efforts to detect it have so far relied on indirect probes of the oscillating superconductor order parameter. In contrast, a direct measurement of an oscillating SCOP using JSTS could provide the incontrovertible proof of this phase that has so far been lacking.

Furthermore, JSTS could be employed to measure superconducting correlations in the pseudogap phase of cuprate superconductors, potentially offering evidence to settle the question of its origin[43, 44, 45]. In particular, some[46, 47, 48] have argued for phase-incoherent superconducting fluctuations dominating the pseudogap region, while others[49, 50, 51] have proposed more recent evidence that the superconducting correlations come from a pair-density wave effect. Recent JSTS experiments on $Bi_2Sr_2CaCu_2O_{8+x}$[7] have argued that the resulting nanometer-resolution I_C measurements provide evidence for the existence of a pair-density wave. However, experiments on these systems are complicated by the nonlocality of the $d_{x^2-y^2}$-wave superconducting order parameter, which requires a spatially extended tip. In order to resolve the question of whether nonlocal tunneling can result in such precise measurements of the superconducting correlations in the pseudogap regime, we use a Keldysh nonequilibrium Green's function formalism to model the Josephson current in a comparable system.

3.2   A model for the cuprates

The starting point for investigating the relation between the spatial form of the critical Josephson current and the SCOP in $d_{x^2-y^2}$-wave superconductors is the Hamil-
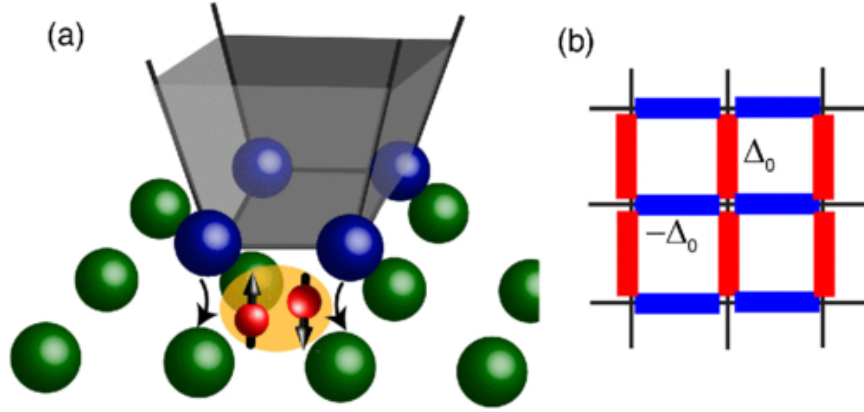
Figure 3.1: (a) An example of a spatially extended tip large enough allow nonlocal tunneling of Cooper pairs. (b) Sign structure of the $d_{x^2-y^2}$ order parameter in a rectangular lattice with next-nearest neighbor tunneling, in which the SCOP has opposite signs in the vertical/horizontal directions.

tonian $H = H_s + H_{\text{tip}} + H_{\text{tun}}$, where

$$
\begin{aligned}
H_s = & -\sum_{\mathbf{r},\mathbf{r}',\sigma} t_{\mathbf{r}\mathbf{r}'} c^{\dagger}_{\mathbf{r}\sigma} c_{\mathbf{r}'\sigma} - \mu \sum_{\mathbf{r},\sigma} c^{\dagger}_{\mathbf{r}\sigma} c_{\mathbf{r}\sigma} - \sum_{\mathbf{r},\mathbf{r}'} \left[\Delta_{\mathbf{r}\mathbf{r}'} c^{\dagger}_{\mathbf{r}\uparrow} c^{\dagger}_{\mathbf{r}\downarrow} + \text{H.c} \right] \\
& + U_0 \sum_{\sigma} c^{\dagger}_{\mathbf{R}\sigma} c_{\mathbf{R}\sigma} - \frac{g u_B}{2} \mathbf{B} \cdot \sum_{\mathbf{r},\alpha,\beta} c^{\dagger}_{\mathbf{r}\alpha} \boldsymbol{\sigma}_{\alpha\beta} c_{\mathbf{r}\beta}
\end{aligned} \tag{3.1}
$$

Here, $-t_{\mathbf{r}\mathbf{r}'}$ is the electronic hopping between sites $\mathbf{r}$ and $\mathbf{r}'$ in the superconductor, μ is the chemical potential, and $c^{\dagger}_{\mathbf{r}\sigma}$ ($c_{\mathbf{r}\sigma}$) creates (annihilates) an electron with spin σ at site $\mathbf{r}$. $\Delta_{\mathbf{r}\mathbf{r}'}$ is the nonlocal (bond) SCOP with $d_{x^2-y^2}$-wave symmetry, which is nonzero only between nearest-neighbor sites and changes sign between the x and y directions, i.e., $\Delta_{\mathbf{r}\mathbf{r}'} = \pm\Delta_0$, as shown in Fig. 3.1(b) for a translationally invariant system. U_0 is the scattering potential of a non- magnetic defect located at $\mathbf{R}$ and the last term represents the Zeeman coupling in a Pauli-limited superconductor, necessary to create the FFLO phase [52, 53]. We employ a set of parameters that is characteristic of the cuprate superconductors' electronic structure with next-nearest- neighbor hopping $t'/t = -0.4$, and $\mu/t = -1$. To account

for spatial oscillations of the SCOP, we compute it self-consistently via

$$\Delta_{\mathbf{rr'}} = -\frac{V_{\mathbf{rr'}}}{\pi} \int_{-\infty}^{\infty} d\omega\, n_F(\omega) \text{Im}[F_{\text{SC}}(\mathbf{r'},\downarrow;\mathbf{r},\uparrow,\omega)] \tag{3.2}$$

where $V_{\mathbf{rr'}}$ is the superconducting pairing potential between nearest-neighbor sites, $n_F(\omega)$ is the Fermi distribution function, and F_{SC} is the nonlocal, retarded anomalous Green's function of the $d_{x^2-y^2}$-wave superconductor (see Section 3.3). We model the JSTS tip as a spatially extended $d_{x^2-y^2}$-wave superconductor with $(n_x \times n_y)$ sites [see Fig.3.1(a)], described by the Hamiltonian $H_{\text{tip}} = H_{\text{tip}}^n + H_{\text{tip}}^{\text{sc}}$, where H_{tip}^n represents the normal state electronic structure of the tip (see Section 3.3), and

$$H_{\text{tip}}^{\text{sc}} = -\sum_{\mathbf{r},\mathbf{r'}} \Delta_{\mathbf{rr'}}^t d_{\mathbf{r}\uparrow}^\dagger d_{\mathbf{r'}\downarrow}^\dagger + \text{H.c.} \tag{3.3}$$

where $\Delta_{\mathbf{rr'}}^t = \pm\Delta_{\text{tip}}$ is the tip's superconducting $d_{x^2-y^2}$-wave order parameter, $d_\sigma^\dagger$ (d_σ) creates (annihilates) an electron with spin σ in the tip, and the sum runs over all tip sites. Finally, the tunneling Hamiltonian is given by

$$H_{\text{tun}} = -t_0 \sum_{\mathbf{r},\sigma} c_{\mathbf{r}\sigma}^\dagger d_{\mathbf{r}\sigma} + \text{H.c.} \tag{3.4}$$

where r denotes sites both in the tip and the $d_{x^2-y^2}$-wave superconductor between which electrons can tunnel. A dc Josephson current I_J [3] between the JSTS tip and the superconductor arises from a phase difference $\Delta\Phi$ between their SCOPs, which can be gauged away [29], yielding real SCOPs and a phase-dependent tunneling amplitude $t_T = t_0 e^{i\Delta\Phi/2}$. Using the Keldysh Green's function formalism[30, 31], one obtains $I_J = I_J^\uparrow + I_J^\downarrow$ to lowest order in the hopping t_T[29] as

$$I_J^\sigma = 4\frac{e}{\hbar} t_0^2 \sin(\Delta\Phi) \int \frac{d\omega}{2\pi} n_F(\omega)\sigma_{\mathbf{r},\mathbf{r'}}\text{Im}\left[F_t(\mathbf{r},\sigma;\mathbf{r'},\bar{\sigma},\omega)F_{\text{sc}}(\mathbf{r'},\bar{\sigma};\mathbf{r},\sigma,\omega)\right] \tag{3.5}$$

where F_t is the retarded anomalous Green's function of the tip, and the sum runs over all sites $\mathbf{r}, \mathbf{r}'$ in the tip and superconductor that are connected by a tunneling element. Finally, $I_J = I_C \sin(\Delta\Phi)$ with I_C being the critical Josephson current. Note that while $\Delta_{\mathbf{rr}'}$ is nonzero for nearest-neighbor sites only, F_{sc} is nonzero for further neighbor sites, which therefore need to be included in the summation in Eq.3.5.

3.3 Definition of Green's functions in real space

To compute the spatial dependence of the non-local $d_{x^2-y^2}$-wave order parameter, $\Delta_{\mathbf{rr}'}$, as well as the critical Josephson current, $I_C(\mathbf{r})$, in the presence of defects, we rewrite the Hamiltonian in Eq.3.1 using the spinor,

$$\Psi^\dagger = \left(c_{1\uparrow}^\dagger, c_{1\downarrow}, ..., c_{i\uparrow}^\dagger, c_{i\downarrow}, ..., c_{N\uparrow}^\dagger, c_{N\downarrow} \right) \tag{3.6}$$

where N is the number of sites in the $d_{x^2-y^2}$-wave superconductor, and $i = 1, ..., N$ is the index for a site $\mathbf{r}$ in the system. The Hamiltonian in Eq.3.1 can then be written as,

$$H_S = \Psi^\dagger \hat{H}_s \Psi$$

We define a retarded Green's function matrix of the system via,

$$\hat{G}_{SC}(\omega + i\delta) = \left[(\omega + i\delta)\hat{1} - \hat{H}_s \right]^{-1}$$

where $\hat{1}$ is the $(N \times N)$ identity matrix and $\delta = 0^+$. The non-local anomalous Green's function $F_{sc}(\mathbf{r}', \downarrow; \mathbf{r}, \uparrow, \omega)$ between sites $\mathbf{r}'$ (with index j) and $\mathbf{r}$ (with index i) that enters the calculation of $I_J^\uparrow$ [see Eq. 3.5] is then given by the $(2j, 2i - 1)$

element of $\hat{G}_s$. The anomalous Green's function $F_{SC}(\mathbf{r}', \uparrow; \mathbf{r}, \downarrow, \omega)$ involved in the calculations of $I_J^\downarrow$ is obtained from the relation,

$$F_{SC}(\mathbf{r}', \uparrow; \mathbf{r}, \downarrow, \omega) = -F_{SC}^*(\mathbf{r}', \downarrow; \mathbf{r}, \uparrow, -\omega)$$

Moreover, we take the anomalous Green's function of the tip, $F_t(\mathbf{r}, \uparrow; \mathbf{r}', \downarrow, \omega)$, to be that of a bulk system which can be computed from the momentum space form of the anomalous Green's function,

$$F_t(\mathbf{k}, \omega) = -\frac{\Delta_{\mathbf{k}}}{E_{\mathbf{k}}} \left[\frac{1}{\omega - E_{\mathbf{k}} + i\delta} - \frac{1}{\omega + E_{\mathbf{k}+i\delta}} \right]$$

via

$$F_t(\mathbf{r}, \uparrow; \mathbf{r}', \downarrow, \omega) = \int \frac{d^2 k}{(2\pi)^2} F_t(\mathbf{k}, \omega) e^{i\mathbf{k}(\mathbf{r}-\mathbf{r}')}$$

where

$$E_{\mathbf{k}} = \sqrt{\epsilon_{\mathbf{k}}^2 + \Delta_{\mathbf{k}}^2}$$

$$\epsilon_{\mathbf{k}} = -2t[\cos k_x + \cos k_y] - 4t' \cos k_x \cos k_y - \mu$$

$$\Delta_{\mathbf{k}} = \frac{\Delta_0}{2}[\cos k_x - \cos k_y]$$

3.4   Imaging defect perturbations

Before discussing the characteristic features of I_C in the pseudogap region of the cuprate superconductors, we first consider its hallmark signatures in a fully phase coherent $d_{x^2-y^2}$-wave superconductor. We begin by investigating the spatial form of the SCOP near a nonmagnetic defect, which gives rise to the emergence of an impurity resonance in the local density of states (LDOS) [28, 54, 55, 56, 57,
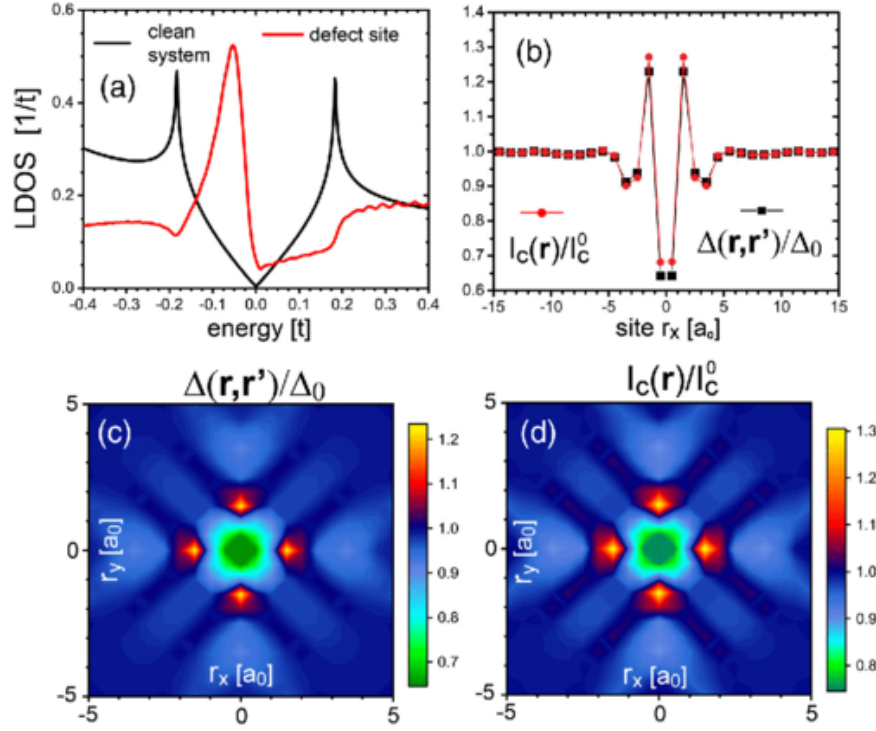
Figure 3.2: Potential disorder in an $d_{x^2-y^2}$ superconductor at $T = 0$ with (a) Local density of states for a clean system and at the site of a $U_0 = 1.5t$ defect. (b) Normalized linecuts of the SCOP and critical current in the $\mathbf{r} = (+1, 0)$ direction across the defect site. The tip is a 2-site superconductor with $\Delta_{\text{tip}} = 4\Delta_0$. (c) Spatial dependence of the normalized SCOP, (d) spatial dependence of the normalized Josephson critical current with $\Delta_{\text{tip}} = \Delta_0$.

36], as shown in Fig. 3.2(a). At the same time, the defect also induces spatial oscillations in the SCOP [see Figs. 3.2(b) and 3.2(c)], which cannot be measured via conventional scanning tunneling spectroscopy [7, 23, 58].

In Fig. 3.2 (b), we present the spatial form of the critical current, I_C, for a tip that consists of 2 sites, which is the smallest possible tip size that still exhibits non-local $d_{x^2-y^2}$-wave correlations. The tip is aligned either along the x or y direction, representing a $(2x1)$ or $(1x2)$ tip, respectively. The resulting I_C probes the superconducting correlations between nearest-neighbor sites only, thus providing direct insight into the nonlocal bond SCOP. The spatial form of I_C for $\Delta_{\text{tip}} = 4\Delta_0$ agrees very well with that of the SCOP [Fig. 3.2(b)], implying that the spatial structure of an unconventional $d_{x^2-y^2}$-wave order parameter can be spatially imaged by the

critical current. This good agreement is independent of the particular magnitude
of the SCOP in the tip, as follows from a comparison of the spatial structure of the
SCOP [Fig. 3.2(c)] and of I_C [Fig. 3.2(d)] for $\Delta_{\text{tip}} = \Delta_0$. The wavelength of the
oscillations along the x and y axis both in $\Delta(\mathbf{r}, \mathbf{r}')$ and I_C is approximately $4a_0$ [Fig.
3.2(b)], which is close to that observed by Hamidian et al. [6]. This wavelength
arises from scattering of electrons between the nearly parallel parts of the Fermi
surface near $(0, \pm\pi)$ and $(\pm\pi, 0)$. Finally, we note that the energy position of the
coherence peaks, as measured with a normal STM tip in conventional dI/dV, re-
mains unchanged in the vicinity of the defect, and hence does not reflect the local
SCOP (for a more detailed discussion, see Section 3.3). While the above results
were obtained with the smallest possible tip size still exhibiting $d_{x^2-y^2}$-wave cor-
relations, the JSTS tip employed by Hamidian et al. [7], was created by picking
up a nanometer-sized flake of $Bi_2Sr_2CaCu_2O_{8+x}$ with a tungsten tip. This immedi-
ately brings into question to what extent the critical current I_C measured by such a
spatially extended JSTS tip can still image the "local" SCOP.

3.5 Implementing an extended STM tip

To investigate this crucial question, we compare in Fig. 3.3 the critical current mea-
sured by several spatially extended JSTS tips of different sizes, with the SCOP
averaged over the area covered by the tip, $\langle\Delta\rangle_{\mathbf{r}}$. We find as expected that with
increasing tip size, the agreement between the I_C and the bond SCOP between
nearest neighbor sites (at the center of the tip) worsens [cf., e.g., $\Delta(\mathbf{r}, \mathbf{r}')$ in Fig.
3.2(b) with I_C in Fig. 3.3(c)]. However, the agreement between the spatial form of
I_C and the averaged SCOP $\langle\Delta\rangle$ remains very good, as shown in Fig. 3.3. More-
over, even for a large $(5x5)$ tip [Fig. 3.3(c)] (which is approximately the size of flake
of $Bi_2Sr_2CaCu_2O_{8+x}$ used by Hamidian et al. [7]) the $\lambda = 4\alpha_0$ spatial oscillations
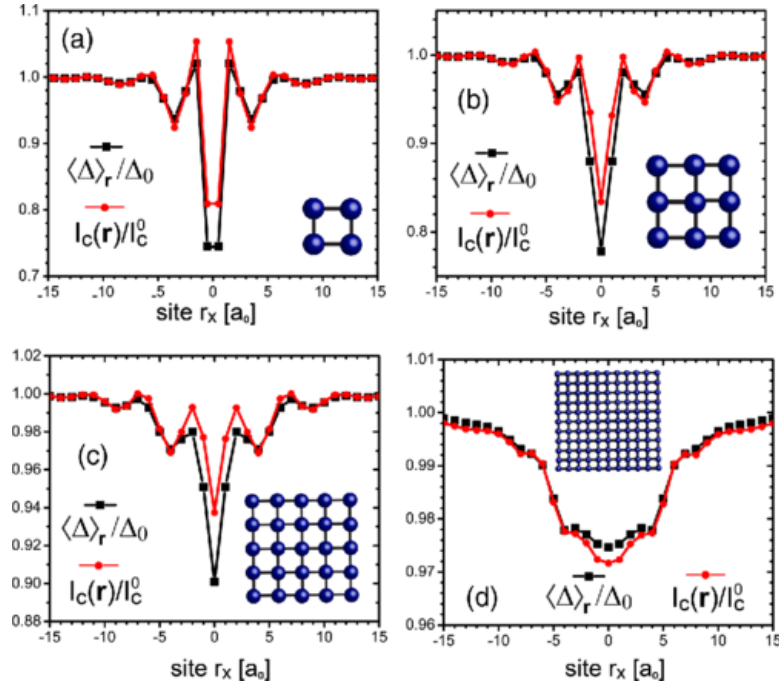
Figure 3.3: Comparison of $I_C(\mathbf{r})$, with $\mathbf{r}$ being the center of the tip, and the spatially average SCOP $\langle\Delta\rangle_\mathbf{r}$ for (a) (2×2), (b) (3×3), (c) (5×5), and (d) (11×11) JSTS tips (the tip sizes are shown as insets). $\langle\Delta\rangle_\mathbf{r}$ is calculated by averaging the magnitude of $\Delta_{\mathbf{rr'}}$ over the region covered by the JSTS tip.

are still visible. As with increasing tip size, the contribution to I_C from nearly unperturbed areas increases even when the tip is centered above the defect, the relative spatial variation of I_C around the defect becomes weaker, as follows from Figs. 3.3(a)–3.3(d). Thus, while with increasing tip size I_C does not any longer image the spatial structure of the bond order parameter $\Delta(\mathbf{r}, \mathbf{r'})$, it nevertheless provides insight into the form of the spatially averaged SCOP. We note that this result is largely robust against disorder in the tunneling amplitude (see Section 3.3), and thus also holds for disordered tips.

3.6 Effects of disorder in the JSTS tip

In the previous section, we considered highly ordered tips with identical tunneling amplitudes between the sites in the tip and the sites in the system. However, it
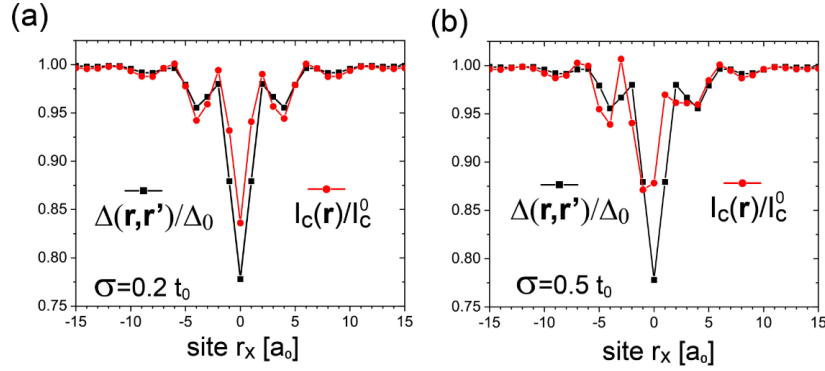
Figure 3.4: Normalized $\Delta(\mathbf{r}, \mathbf{r}')$ and I_C for a (3×3) tip in the presence of disorder in the tunneling amplitude with standard deviation (a) $\sigma = 0.2t_0$, and (b) $\sigma = 0.5t_0$, where t_0 is the tunneling amplitude in the clean case.

is very likely that in the experimental case, the tip is disordered to some extent, resulting in disorder in the tunneling amplitudes. To investigate the effects of such a disorder on the spatial structure of the measured Josephson current, we consider a spatially varying tunneling amplitude, $t_0(r)$. In this case, the Josephson current is given by

$$I_J^{\sigma} = 4\frac{e}{\hbar}\sin(\Delta\Psi)\sum_{\mathbf{r},\mathbf{r}'} t_0(\mathbf{r})t_0(\mathbf{r}')\int\frac{d\omega}{2\pi}n_F(\omega)\text{Im}[F_t(\mathbf{r},\sigma;\mathbf{r}',\bar{\sigma},\omega)F_{sc}(\mathbf{r}',\bar{\sigma};\mathbf{r},\sigma,\omega)] \text{ (3.7)}$$

In Fig. 3.4, we compare the normalized $\Delta(\mathbf{r}, \mathbf{r}')$ and I_C for a (3×3) tip in which the tunneling amplitude possesses a standard deviation of $\sigma = 0.2t_0$ [Fig. 3.4(a)] and $\sigma = 0.5t0$ [Fig. 3.4(b)], where t_0 is the tunneling amplitude in the clean case. We find that even for the case of $\sigma = 0.5t_0$ [Fig. 3.4(b)], which represents already a significant amount of disorder, the agreement between the spatial structure of $\Delta(\mathbf{r}, \mathbf{r}')$ and I_C is still quite good. The reason for the good agreement even in the stronger disorder case is that for the spatially extended tip considered here, the measured I_C is proportional to the spatially averaged superconducting order parameter, due to the summations over $\mathbf{r}$ and $\mathbf{r}'$. These summations also lead to an averaging out of the disorder effects, implying that site-dependent disorder has
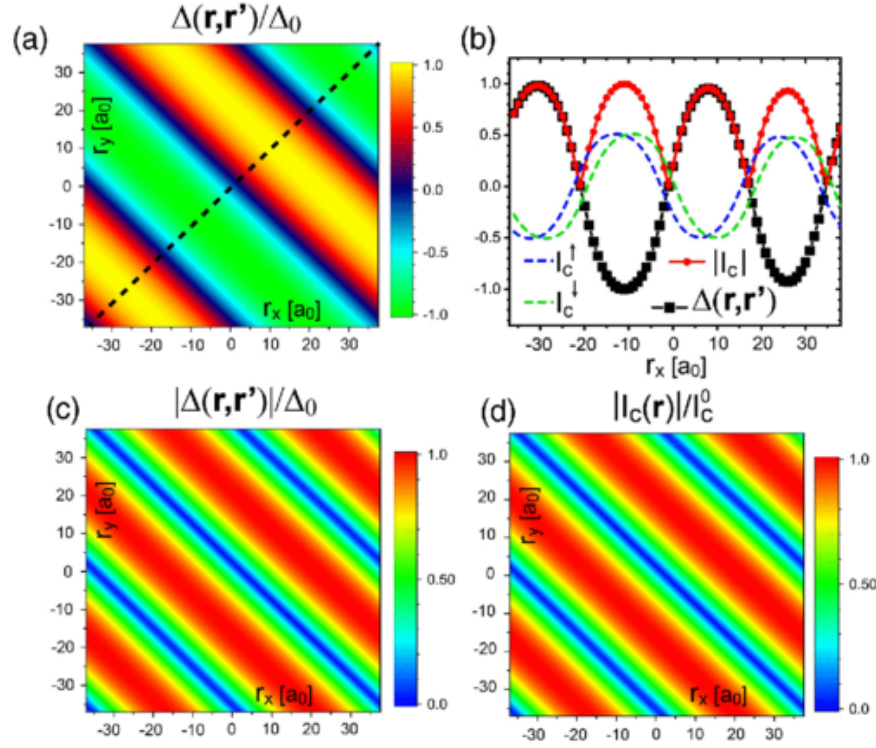
Figure 3.5: (a) $\Delta(\mathbf{r}, \mathbf{r}')$ in the FFLO phase for $g\mu_B B/2 = 0.1t$. (b) Line cut of $\Delta(\mathbf{r}, \mathbf{r}')$ and $I_C = I_C^{\uparrow} + I_C^{\downarrow}$ along the black dashed line in (a) with $\Delta_{\text{tip}} = \Delta_0$. (c) Modulus of $\Delta(\mathbf{r}, \mathbf{r}')$ and (d) I_C for a $(2 \times 1)/(1 \times 2)$ tip.

less of an impact for spatially extended tips. This demonstrates that the ability of I_C

to spatially image $\Delta(\mathbf{r}, \mathbf{r}')$ persists even in the presence of significant tip disorder.

3.7 Identification of the Fulde-Ferrell-Larkin-Ovchinikoff phase

The magnetic-field induced Fulde-Ferrell-Larkin-Ovchinikoff (FFLO) phase repre-

sents another example for a phase in which the SCOP exhibits characteristic spa-

tial oscillations. Such a phase might be realized in the heavy fermion superconduc-

tor CeCoIn$_5$ [40, 41, 42], which was argued to possess a superconducting $d_{x^2-y^2}$-

wave symmetry [59, 60].

Solving Eq. 3.2 for $\Delta_{\mathbf{r}\mathbf{r}'}$ in the presence of a magnetic field, we find that the

SCOP shows sinusoidal spatial oscillations accompanied by a sign change [see
Figs. 3.5(a) and 3.5(b)], reflecting a nonzero center-of-mass momentum of the
Cooper pairs in the FFLO phase [52, 53]. As current JSTS experiments can mea-
sure only the magnitude of I_C, but not I_J itself, we compare in Figs. 3.5(c) and
3.5(d) the spatial structures of the modulus of $\Delta(\mathbf{r}, \mathbf{r}')$ and I_C , which show very
good agreement. Moreover, a line cut of the SCOP and I_C in Fig. 3.5(b) reveals
that the sign change in $\Delta(\mathbf{r}, \mathbf{r}')$ leads to a characteristic $|\sin(kr)|$ structure in I_C .
Thus the measured I_C does not only reflect $|\Delta(\mathbf{r}, \mathbf{r}')|$, but its spatial form can also
detect sign changes in the SCOP. These results, taken together, show for the first
time that it is possible to detect the presence of the FFLO phase, and reveal its
much anticipated spatial SCOP structure via JSTS. Finally, we note that the Zee-
man splitting of the spin-↑ and spin-↓ bands [61] also possesses a counterpart in
I_C : its spin-↑ ($I_C^\uparrow$) and spin-↓ ($I_C^\downarrow$) contributions, shown by the dashed blue and
green lines in Fig. 3.5(b), respectively, are spatially split due to the SCOP's finite
center-of-mass momentum.

3.8   Critical current in the pseudogap regime

As the measurement of the critical current is a local probe, we expect that a
nonzero I_C is measured as long as a system exhibits local superconducting corre-
lations. As such, JSTS possesses the potential to probe the nature of the pseudo-
gap, and, in particular, its proposed origin arising from phase-incoherent supercon-
ducting correlations (precursor pairing) [46, 47, 48, 62]. To explore this possibility,
we start from the observations of conventional STS experiments[9, 63, 64] that re-
ported the existence of a heterogeneous, domainlike structure in the underdoped
cuprates at $T << T_C$: in one type of domain, the LDOS exhibits all the traits of
a $d_{x^2-y^2}$-wave superconductor with well-defined coherence peaks (the SC region),
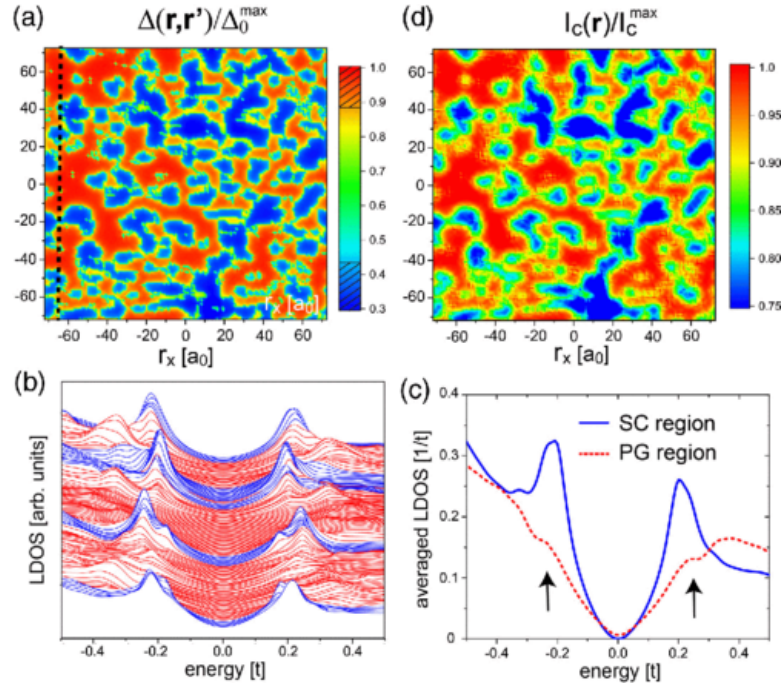
Figure 3.6: Theoretical (to-scale) model of the gapmap shown in Fig. 1(a) of Ref. [9]. (a) Spatial plot of $\Delta(\mathbf{r}, \mathbf{r}')$ with $\tau_{ph}^{-1} = 0.05t/\hbar$ for the PG regions (red) and $\tau_{ph}^{-1} \to 0$ for the SC regions (blue). (b) LDOS along the black dashed line in (a). Blue (red) curves correspond to the SC (PG) regions. (d) Spatial plot of $I_C(\mathbf{r})$ for a $(2 \times 1)/(1 \times 2)$ tip.

and one in which the gap appears larger than in the superconducting regions, but in which the coherence peaks are significantly broadened (the PG region). Below, we model the pseudogap as arising from phase incoherent superconducting correlations [48, 62], as characterized by a finite phase-coherence coherence time τ_{ph}, such that $\Delta(\mathbf{r}, \mathbf{r}')$ in the PG regions should be interpreted as a measure for the bond superconducting correlations, rather than a phase-coherent bond order parameter [48, 62]. To investigate the form of I_C in such a heterogeneous system, we created a theoretical real-space (to-scale) model of the experimental gap map shown in Fig. 1(a) of Ref. [9], which reflects the existence of the two domains.

The self-consistently computed OP shown in Fig. 3.6(a) reproduces well the

spatial structure of the experimental gap map. Here, $\Delta^{pg}_{\mathbf{rr'}}$ is calculated via,

$$\Delta^{pg}_{\mathbf{rr'}} = -\frac{V_{\mathbf{rr'}}}{\pi} \int_{-\infty}^{\infty} d\omega n_F(\omega) \mathsf{Im}[F_{pg}(\mathbf{r}, \mathbf{r'}, \omega)]$$

with

$$\hat{G}_{pg}(\omega + i\gamma) = \left[(\omega + i\gamma)\hat{1} - \hat{H}_s \right]^{-1}$$

and we describe the pseudo-gap regions as a phase-incoherent $d_{x^2-y^2}$-wave superconductor where the finite phase coherence time τ_{ph} is included in $\gamma = \hbar/\tau_{ph}$, as modeled elsewhere[62]. A finite τ_{ph} immediately leads to a broadening of the coherence peaks, as shown in Figs. 3.6(b) and 3.6(c), where we used $\gamma = 0.05t$ in the PG regions, and $\gamma = 0.005t$ in the SC regions. In order to achieve that the coherence peaks in the PG regions are located at higher energies (while at the same time being broadened), we increased the effective pairing interaction in the PG regions over that in the superconducting regions. As a result, the OP in the PG regions is larger than in the superconducting regions.

In a heterogeneous system, the theoretical OP is in general not identical to the gap which is experimentally determined from the position of the coherence peaks. In Fig. 3.6(b), we show a line cut of the LDOS [along the dashed black line in Fig. 3.6(a)], which exhibits the characteristic evolution of the LDOS between the SC and PG regions also found in STS experiments [see Fig. 3(a) of Ref. [9]]. To directly compare our results with the spatially averaged experimental dI/dV data [see Fig. 3(b) in Ref. [64]], we present in Fig. 3.6(c), the LDOS spatially averaged over the SC and PG regions along the line cut in Fig. 3.6(a) [these regions are defined by an OP that lies within the shaded blue (SC) or red (PG) regions of the legend in Fig. 3.6(a), respectively].

Our results reproduce a series of characteristic traits exhibited by the experi-

mentally averaged data [see Fig. 3(b) in Ref. [64]]: (i) while the gap in the PG
region is larger than in the SC region, the coherence peaks in the PG region are
smeared out, (ii) the LDOS in the PG regions (red dashed line) exhibits shoulderlike
features (see arrows) at the energies of the coherence peaks in the SC regions, (iii)
the shoulderlike feature is more pronounced at positive than at negative energies,
and(iv) the spectra exhibit overall a strong particle-hole asymmetry.

All of these results are in good agreement with the experimental findings, thus
supporting the validity of the model employed here. In Fig. 3.6(d), we present a
spatial plot of I_C obtained for the heterogeneous system shown in Fig. 3.6(a). We
again find that I_C spatially images the OP, and that despite the incoherent nature of
the PG region, the Josephson current in these regions is nonzero (though I_C in the
PG regions decreases with decreasing τ_{ph}). This implies that I_C indeed reflects
the presence of local superconducting correlations, rather than global phase co-
herence. In contrast, if the PG were to arise from nonsuperconducting correlations
or order parameters, such as charge- or spin-density wave correlations, I_C would
vanish. Thus, a nonzero measurement of I_C in the PG region would provide strong
evidence for precursor pairing as its origin.

Throughout this chapter, we have consistently shown that JSTS is able to
closely image the superconducting order parameter in $d_{x^2-y^2}$-wave superconduc-
tors. In the FFLO phase, the spatially oscillating SCOP was visible in a sign change
of the critical current, and variations in the SCOP's magnitude could be identified
in JSTS tips ranging from atomic- to flake-sized. Furthermore, the ability of JSTS
to detect the presence of phase-incoherent superconducting correlations offers the
potential to use it as a probe to discriminate between precursor pairing and other
possible mechanisms underlying superconductivity in the PG regime.

Chapter 4

Topological superconductivity in skyrmion lattices

This chapter is based off of an unpublished manuscript[65],

    Mascot, E., J. Bedow, M. Graham, S. Rachel, and D. K. Morr (2020, April). Topological Superconductivity in Skyrmion Lattices. *arXiv e-prints*, arXiv:2005.00027.

4.1   Motivating a topologically tunable system

Detection, operation, and manipulation of fault-tolerant qubits is essential for the realization of a quantum computer, one of the holy grails of modern physics. One of the most promising ways to construct fault-tolerant qubits relies on the topological protection offered by non-Abelian braiding operations on Majorana zero modes[66]. These modes have been observed in one-[67, 68, 69, 70, 71] and two-dimensional (2D) topological superconductors [72, 73, 74], with 2D systems also exhibiting chiral Majorana edge currents [75, 76, 77]. Magnet-superconductor hybrid (MSH) systems consisting of chains, islands or layers of magnetic adatoms deposited on the surface of conventional s-wave superconductors have proven to be suitable candi-

dates for the creation of topological superconductivity via atomic manipulation[71], interface engineering techniques[76], and for the study of Majorana modes using STS. 2D MSH systems, in particular, offer a rich topological phase diagram characterized by a topologically invariant Chern number [78, 79, 80]. However, tuning these systems between topological phases, a key requirement for the operation of qubits, remains experimentally inaccessible.

In the following chapter, we propose a magnetic skyrmion lattice as an example of an MSH system that offers a complex topological phase diagram along with the potential to tune the system through phase transitions by changing the applied magnetic field and thus the skyrmion radius[81]. In the skyrmion lattice, this tunability is realized by a magnetically-induced Rashba spin-orbit interaction that images the local skyrmion charge and is reflect in the spatial structure of the zero-energy LDOS. Finally, we show that the superconducting spin-triplet correlations underlying the emergence of topological superconductivity can be visualized by Josephson scanning tunneling spectroscopy (JSTS). Taken together, these results demonstrate the viability of 2D skyrmion MSH systems, which can be constructed with current techniques[81], as an avenue to explore topological superconductivity and manipulate Majorana zero modes.

4.2   Model of a skyrmion lattice

We investigate the emergence of topological superconductivity in a 2D MSH system, in which a magnetic skyrmion lattice (see Fig. 4.1a) is placed on the surface of a conventional s-wave superconductor, as described by the Hamiltonian

$$H = \sum_{\mathbf{r},\mathbf{r}',\sigma}(-t_{\mathbf{r}\mathbf{r}'} - \mu\delta_{\mathbf{r},\mathbf{r}'})c^\dagger_{\mathbf{r}\sigma}c_{\mathbf{r}'\sigma} + \Delta\sum_{\mathbf{r}}\left(c^\dagger_{\mathbf{r}\uparrow}c^\dagger_{\mathbf{r}\downarrow} + \text{H.c.}\right) + J\sum_{\mathbf{r},\alpha,\beta}\mathbf{S_r}\cdot c^\dagger_{\mathbf{r}\alpha}\sigma_{\alpha\beta}c \quad (4.1)$$

where $c_{\mathbf{r}\alpha}^{\dagger}$ creates an electron at lattice site $\mathbf{r}$ with spin α, and σ is the vector of

spin Pauli matrices. We consider a triangular lattice with lattice constant a_0, chem-

ical potential μ, and hopping amplitude $-t_{\mathbf{r}\mathbf{r}'} = -t$ between nearest-neighbor sites

only. Δ is the superconducting s-wave order parameter. The spatial spin struc-

ture of the skyrmion lattice is encoded in $\mathbf{S_r}$, which represents the direction of an

adatom's spin located at site $\mathbf{r}$, and J is its exchange coupling with the conduction

electron spin. Note that the creation of Majorana modes in single skyrmions has

previously been discussed in Refs [82, 83]. As Kondo screening is suppressed

by the full superconducting gap, the spins $S_{\mathbf{r}}$ are taken to be classical vectors of

length S. We assume that the triangular lattice of skyrmions is commensurate with

the underlying triangular surface lattice, thus allowing the skyrmion radius R to

take integer and half-integer values of a_0. Note that in contrast to earlier studies of

2D MSH systems [78, 79, 80], the above Hamiltonian does not contain an intrinsic

Rashba spin-orbit (RSO) interaction. Moreover, due to the broken time-reversal

symmetry arising from the presence of magnetic moments, and the particle-hole

symmetry of the superconducting state, the topological superconductor belongs to

class D [84].

To characterize the topological superconducting phases of the system, we com-

pute the topological invariant - the Chern number C - given by

$$
\begin{aligned}
C &= \frac{1}{2\pi} \int_{\mathsf{BZ}} d^2k \mathsf{Tr}(P_{\mathbf{k}}[\partial_{k_x} P_{\mathbf{k}}, \partial_{k_y} P_{\mathbf{k}}]) \qquad (4.2) \\
P_{\mathbf{k}} &= \sum_{E_n(\mathbf{k})<0} |\Psi_n(\mathbf{k})\rangle\langle\Psi_n(\mathbf{k})| \qquad (4.3)
\end{aligned}
$$

where $E_n(\mathbf{k})$ and $|\Psi_n(\mathbf{k})\rangle$ are the eigenenergies and the eigenvectors of the

Hamiltonian in Eq.4.1, with n being a band index, and the trace is taken over

Nambu and spin-space. Further insight into the origin underlying the emergence

of topological superconductivity in skyrmion MSH systems can be gained by con-
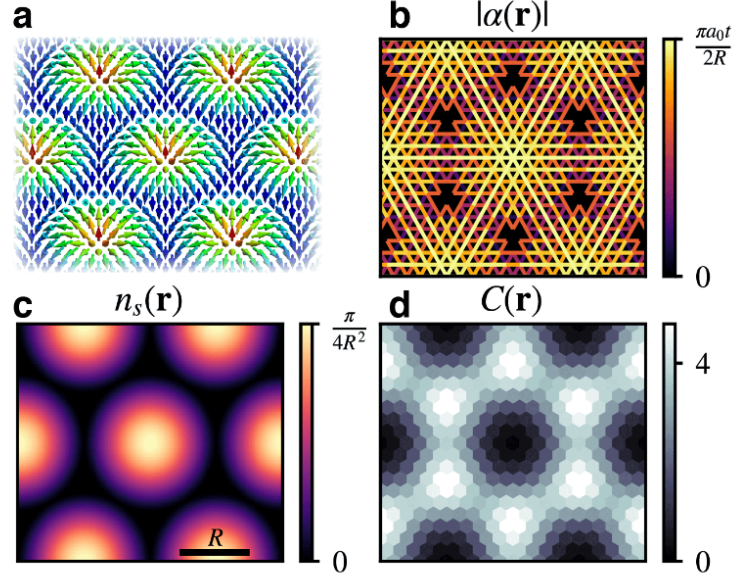
Figure 4.1: MSH system with a magnetic skyrmion lattice. **a** Schematic picture of a skyrmion lattice. Spatial plot of **b** the magnitude of the induced Rashba spin orbit interaction, $|\alpha(\mathbf{r})|$, **c** the skyrmion number density, $n_S(\mathbf{r})$, and **d** the Chern number density $C(\mathbf{r})$ for skyrmion radius $R = 5a_0$, and parameters $(\mu, \Delta, JS) = (-5, 0.4, 0.5)t$.

sidering the spatial structure of the skyrmion and Chern number densities, $n_s(\mathbf{r})$ and $C(\mathbf{r})$, respectively. The former is given by

$$n_s(\mathbf{r}) = \frac{1}{4\pi}\mathbf{S}(\mathbf{r}) \cdot [\partial_x\mathbf{S}(\mathbf{r}) \times \partial_y\mathbf{S}(\mathbf{r})] \tag{4.4}$$

yielding a skyrmion number $n_s = \sum_{\mathbf{r}} n_s(\mathbf{r})$. The latter, $C(\mathbf{r})$ [85, 86], represents the real-space analog of the Berry curvature, and allows[87, 88] a real space calculation of the Chern number $C = 1/N^2 \sum_{\mathbf{r}} C(\mathbf{r})$ that coincides with that obtained from Eq. 4.2.

4.3   Topological phase diagram

A crucial aspect for the emergence of topological superconductivity in 2D skyrmion
MSH systems is that the magnetic skyrmion lattice induces an effective, spatially
varying Rashba spin-orbit interaction. To demonstrate this, a unitary transforma-
tion [89] may be applied to the Hamiltonian in Eq.4.1 that rotates the local spin $\mathbf{S}(\mathbf{r})$
to the $\hat{z}$ axis, yielding an out-of-plane ferromagnetic order and a spatially inhomo-
geneous RSO interaction, $\alpha(\mathbf{r})$ (see Fig.4.1b). $\alpha(\mathbf{r})$ possesses the same spatial
structure as the skyrmion number density, $n_s(\mathbf{r})$, (see Fig.4.1c) – reflecting its ori-
gin in the local topological charge of the skyrmion lattice – with its largest value,
$\alpha_{\mathsf{max}} = \pi a_0 t/(2R)$, in the center of the skyrmion and a vanishing $\alpha(\mathbf{r})$ at the cor-
ners of the skyrmion lattice Wigner-Seitz unit cell. The existence of a non-zero
$\alpha(\mathbf{r})$, of an out-of-plane ferromagnetic order in the rotated basis, and of a hard
s-wave gap, satisfies all necessary requirements for the emergence of topologi-
cal superconductivity [78, 79, 80], resulting in the rich topological phase diagram
shown in Fig.4.2. The phase diagram in the (μ, R) plane (see Fig.4.2a) reveals
the intriguing result that it is possible to tune a skyrmion MSH system between
different topological phases by changing the skyrmion radius R, which can be ex-
perimentally achieved through the application of an external magnetic field [81].
This unprecedented ability arises from the facts that (a) varying the skyrmion ra-
dius leads to changes in the induced $\alpha(\mathbf{r})$, and (b) in contrast to MSH systems with
a homogeneous ferromagnetic structure, topological phase transitions in magnet-
ically inhomogeneous MSH systems (as given here) are controlled not only by μ
and J, but also by α.

Indeed, the results in Fig.4.2a reveal that the phase transition lines in the (μ, R)
plane are determined $u = A_i + B_i/R^2$ (see dashed lines) with constants A_i, B_i.
Since $\alpha_{\mathsf{max}} \sim 1/R$, our result suggests that the induced RSO interaction leads
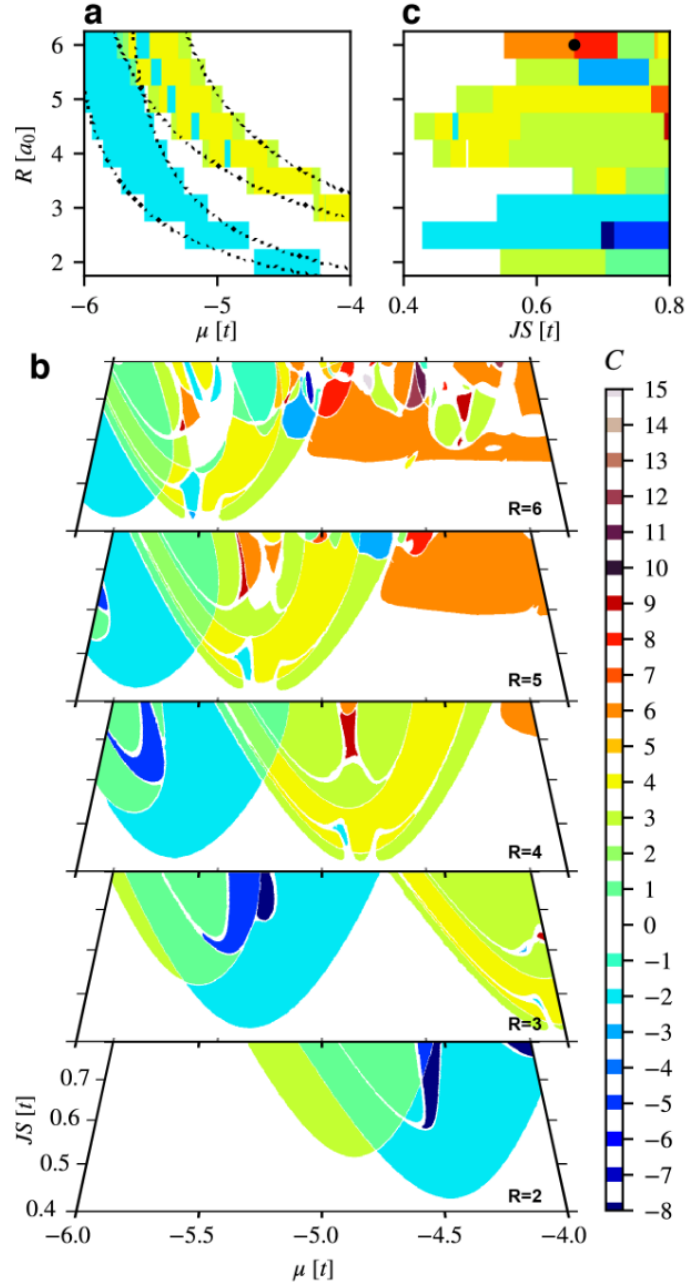
Figure 4.2: Topological phase diagrams of a skyrmion MSH system. Topological phase diagrams representing the Chern number, C, in the **a** (μ, R) plane for $JS = 0.5t$, **b** (μ, JS) planes for various skyrmion radii R, and **c** the (JS, R) plane for $\mu = -5t$ and $\Delta = 0.4t$. Dashed lines in **a** represent phase transition lines described by $\mu = A_i + B_i/R^2$ with constants A_i, B_i.

to an effective renormalization of the chemical potential [82], thus facilitating the
ability to tune between topological phases. This dependence of the phase transi-
tion lines on R is also revealed when considering the phase diagrams in the (μ, J)
plane for different skyrmion radii (see Fig. 4.2b). These phase diagrams show a
very similar structure of topological phases for different R, with the phases moving
to lower values of μ with increasing R. We note that the topological phases that
are accessible through tuning of R strongly depend on JS(see Fig. 4.2c): for suf-
ficiently large JS, every change in the skyrmion radius by a half-integer leads to
a change in the system's Chern number. Thus, a rich topological phase diagram
can be accessed and explored through changes in the skyrmion radius R. The
inhomogeneous magnetic structure of the MSH system also allows us to reveal
an intriguing connection between the Chern number density, $C(\mathbf{r})$, which is a local
marker for the topological nature of the system, and the Berry curvature in momen-
tum space. In particular, the spatial structure of $C(\mathbf{r})$ (see Fig. 4.1d) reflects that
of the skyrmion lattice, but is complementary to that of the induced $\alpha(\mathbf{r})$ (see Fig.
4.1b), with the maximum in $C(\mathbf{r})$ occurring at the corners of the skyrmion lattice
unit cell. However, it is in these regions that the lowest energy states possess their
largest spectral weight, establishing a real space analogue of the observation that
the lowest energy states in momentum space in general possess the largest Berry
curvature.

4.4   Electronic structure at a topological phase tran-
sition

The real space structure of the induced RSO interaction, and hence that of the
local topological skyrmion charge, is reflected in the electronic structure of the

MSH system, and becomes particularly evident at a topological phase transition.
To demonstrate this, we consider the transition between a $C = 8$ and $C = 6$ phase,
as indicated by the solid black dot in Fig. 4.2c. While the system possesses a
topological gap on either side of the transition, the gap at the transition closes at
the K,K'-points (see Fig. 4.3a), as confirmed by a plot of the dispersion $E_{\mathbf{k}}$ of
the lowest energy band (see Fig.4.3b) in the reduced Brillouin zone (RBZ). This
gap closing is reflected in a unique spatial and energy structure of the zero-energy
local density of states (LDOS) [see (xy)-plane in Fig.4.3c]. In particular, the spatial
structure of the LDOS reveals that the largest (smallest) spectral weight of the zero-
energy state, associated with the phase transition, is located where the induced
RSO interaction is the smallest (largest), at the corners of the Wigner-Seitz unit
cell (the skyrmion center). Thus, the spatial pattern of the zero-energy LDOS is
complementary to that of the local topological skyrmion charge, $n_s(\mathbf{r})$. Moreover,
as the topological gap in general increases with increasing RSO interaction, we find
that the large induced RSO interaction in the skyrmion center leads to a dome-
like region in energy in which the LDOS is suppressed [see (x, E)- and (y, E)-
planes in Fig. 3c]. The electronic structure of the skyrmion MSH systems also
provides a unique example to demonstrate that the multiplicity m of the momenta
in the Brillouin zone, at which the gap closing occurs, determines and is equal to
the change in the Chern number at the transition. For the time-reversal invariant
$\Gamma, M, (K, K')$ points, the multiplicity is $m = 1, 3, 2$ (note that by symmetry, a gap
closing at the K point implies a gap closing at K' as well), respectively, as each M
(K, K') point is shared by 2(3) BZs, leading to a change in the Chern number by
$\Delta C = 1, 3, 2$ at the transition.

Gap closings can also occur at non-TRI points, e.g., at points along the $\Gamma - M$
line, which possess a multiplicity of $m = 6$, resulting in a change of the Chern
number by $\Delta C = 6$. While all of the above gap closings exhibit a Dirac cone (see
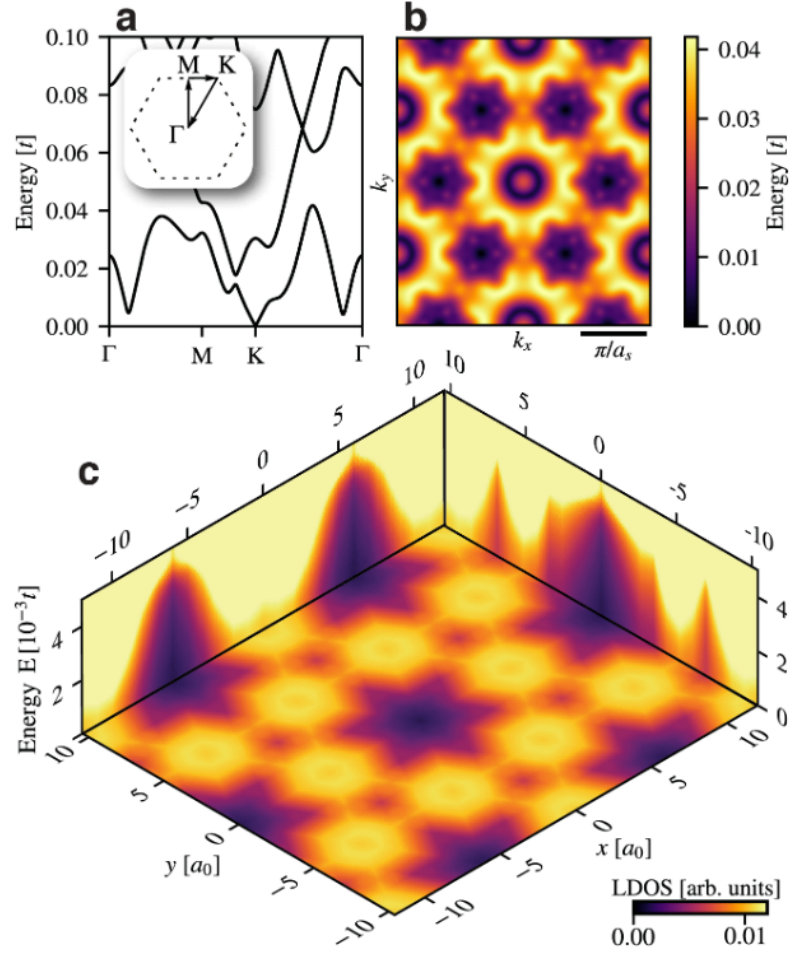
Figure 4.3: Electronic band structure at a topological phase transition. **a** Electronic bands at the phase transition between two topological phases with $C = 6$ and $C = 8$ (as indicated by the solid black dot in Fig. 4.2c) for $R = 6a_0$ and parameters $(\mu, \Delta, JS) = (-5, 0.4, 0.657)t$. Shown is the Brillouin zone(BZ) of the skyrmion lattice, i.e., the reduced BZ (RBZ) of the underlying surface lattice. Spatial plot of **b** the dispersion E_k of the lowest energy band in the RBZ ($a_s = 2R$ is the lattice constant of the skyrmion lattice), and **c** the LDOS at the phase transition, as a function of position and energy.

Fig. 4.3a), there also exist gap closings that exhibit lines of zero-energy, rather than discrete zero energy Dirac points. These gap closings, however, are not accompanied by a change in the Chern number.

4.5   MSH system with a skyrmion ribbon

To study the emergence of chiral Majorana edge modes in a skyrmion MSH system, we next consider a skyrmion ribbon placed on the surface of an s-wave superconductor (see Fig. 4.4a). In a topological phase with Chern number C, the bulk-boundary requires that such a MSH system possess $|C|$ chiral Majorana edge modes per edge. These modes traverse the superconducting gap and disperse linearly near the chemical potential as a function of the momentum along the ribbon edge, as shown in the inset of Fig. 4.4b for the $C = 3$ phase. A spatial plot of the zero-energy LDOS (see Fig. 4.4b) demonstrates that the chiral Majorana mode is as expected localized along the edges of the ribbon, and that its spatial structure is complementary to that of the local skyrmion topological charge. The spatial structure of the skyrmion lattice, and hence of the induced $\alpha(\mathbf{r})$, is also reflected in the combined energy and spatial dependence of the LDOS (see Fig. 4.4c) as revealed by a line-cut of the LDOS from the bottom to the top of the ribbon along $x = 0$ (left edge of Fig. 4.4b). In particular, in the center of the skyrmions, where α is the largest, the spectral weight in the LDOS is pushed to higher energies. The spatial structure of the LDOS is therefore similar to that exhibited by the MSH system at a phase transition (see Fig. 4.3c).

In addition to the chiral Majorana edge modes, the magnetic structure of the skyrmion ribbon leads to two unique physical features. The first one is the spatial form of persistent supercurrents that are induced by the broken time-reversal symmetry. While these supercurrents are generally confined to the edges of an
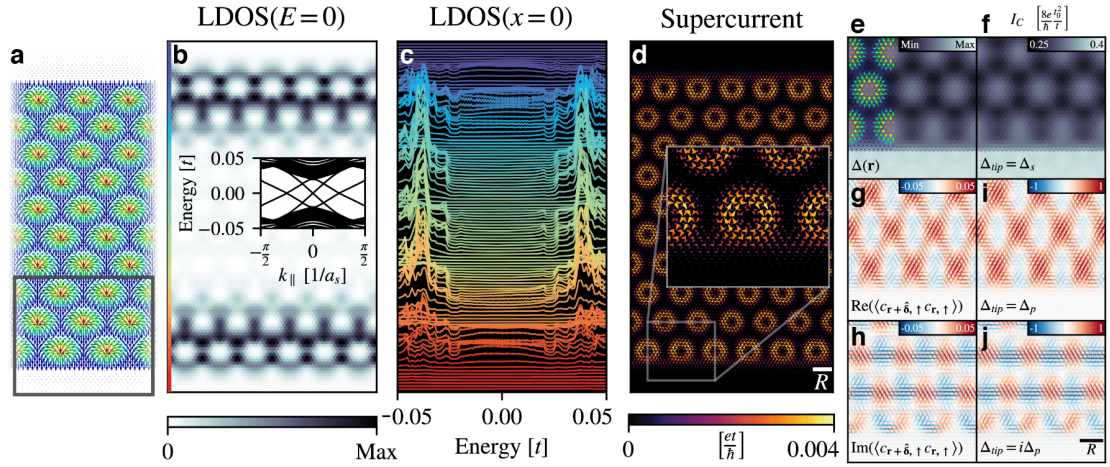
Figure 4.4: MSH system with a skyrmion ribbon. **a** Schematic form of a skyrmion lattice ribbon on the surface of an s-wave superconductor. **b** Spatial plot of the zero energy LDOS. Inset: electronic band structure as a function of momentum, $k_\parallel$ long the ribbon with a width of 27 skyrmions in the $C = 3$ phase. **c** Energy-dependent LDOS for positions from the bottom to the top of the ribbon at $x = 0$ as shown in **b**. **d** Persistent supercurrents in the skyrmion ribbon. Spatial structure of **e** the superconducting s-wave order parameter, $\Delta(\mathbf{r})$, and **f** the critical Josephson current I_c measured via JSTS using an s-wave order parameter in the tip (shown area corresponds to black square in **a**). Spatial structure of the **g** real and **h** imaginary part of the superconducting triplet correlations between nearest neighbor sites. Spatial structure of $I_c(\mathbf{r})$ measured via JSTS with the tip possessing a **i** purely real, and **j** purely imaginary triplet superconducting order parameter. Parameters are $(JS, \Delta, \mu) = (0.5, 0.4, -5.5)t$ and $R = 5a_0$, corresponding to the $C = 3$ phase, with a width of 10 skyrmions.

MSH system [80], the inhomogeneous magnetic structure of the skyrmion lattice
leads to supercurrents that circulate each skyrmion, not only along the ribbon's
edge, but also in its interior (see Fig. 4.4d). These supercurrents screen the out-
of-plane component of the local magnetic moments, similar to the case of a vortex
lattice, and are carried by both the in-gap and bulk states. The second unique fea-
ture is the presence of spin-triplet superconducting correlations which are a crucial
requirement for the emergence of topological superconductivity [80].

4.6   Spatial imaging of the spin-triplet superconduct-ing correlations

The development of Josephson scanning tunneling spectroscopy (JSTS) [26, 7,
23, 27, 8] has provided a unique opportunity to visualize not only these correla-
tions in real space at the atomic level, but also to investigate the effects of the
inhomogeneous magnetic structure of the skyrmion lattice on the superconduct-
ing s-wave order parameter, $\Delta(\mathbf{r})$ [90]. Specifically, pair-breaking effects of the
magnetic moments lead to a spatially non-uniform suppression of $\Delta(\mathbf{r})$ inside the
skyrmion ribbon (see Fig. 4.4e), with the largest suppression occurring where the
induced RSO interaction is the weakest. This spatial structure of $\Delta(\mathbf{r})$ is well im-
aged by that of the critical Josephson current, $I_C(\mathbf{r})$ (see Fig. 4.4f), measured via
JSTS using a tip with an s-wave superconducting order parameter [90], thus pro-
viding direct insight into the strength of local pair breaking effects. Moreover, the
inhomogeneous magnetic structure of the skyrmion lattice enables the emergence
of superconducting spin-triplet correlations not only in the equal-spin channels $|\uparrow\uparrow\rangle$
and $|\downarrow\downarrow\rangle$ (corresponding to Cooper pair spin states $S_z = \pm 1$), but also in the mixed-
spin ($S_z = 0$) channel, $|\uparrow\downarrow\rangle + |\downarrow\uparrow\rangle$. These correlations are a direct consequence
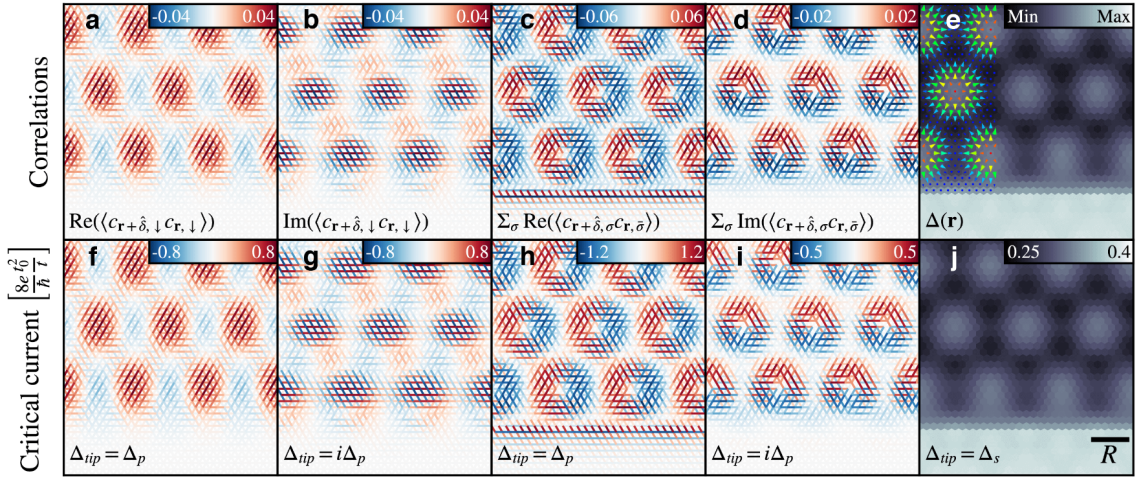
Figure 4.5: **a-d** Spatial structure of the superconducting triplet correlations be-
tween nearest-neighbor sites (red corresponding to positive in $+x$ direction) and **f-i**
the Josephson current measured with a superconducting spin-triplet JSTS tip. **e**
Spatial structure of the local superconducting singlet correlations and **j** the Joseph-
son current measured with an s-wave JSTS tip as shown in Fig. 4.4 for comparison.
Parameters used are $(JS, \Delta, \mu) = (0.5, 0.4, -5)t$ and $R = 5a_0$.

of the magnetic structure of the skyrmions, and thus vanish outside the ribbon.

The spatial spin-triplet superconducting correlations between nearest-neighbor

sites $\mathbf{r}$ and $\mathbf{r} + \delta$ in the equal-spin-pairing states $|\uparrow\uparrow\rangle$ and $|\downarrow\downarrow\rangle$, and in the opposite

spin-pairing state $|\uparrow\downarrow\rangle + |\downarrow\uparrow\rangle$ are given by,

$$
\begin{aligned}
\langle c_{\mathbf{r}+\delta,\uparrow} c_{\mathbf{r},\uparrow}\rangle &= \frac{1}{2\pi i} \int d\omega g_{14}^{<}(\mathbf{r}, \mathbf{r} + \delta, \omega) \\
\langle c_{\mathbf{r}+\delta,\downarrow} c_{\mathbf{r},\downarrow}\rangle &= \frac{1}{2\pi i} \int d\omega g_{23}^{<}(\mathbf{r}, \mathbf{r} + \delta, \omega) \\
\langle c_{\mathbf{r}+\delta,\uparrow} c_{\mathbf{r},\downarrow}\rangle + \langle c_{\mathbf{r}+\delta,\downarrow} c_{\mathbf{r},\uparrow}\rangle &= \frac{1}{2\pi i} \int d\omega [g_{24}^{<}(\mathbf{r}, \mathbf{r} + \delta, \omega) + g_{13}^{<}(\mathbf{r}, \mathbf{r} + \delta, \omega)]
\end{aligned}
$$

(4.5)

Here, $g_{mn}^{r,a,<}(\mathbf{r}, \mathbf{r} + \delta, \omega)$ is the (m, n)-th element of the retarded, advanced, or

lesser Green's function matrix in Nambu space. The Green's function is defined in

Matsubara time via,

$$\hat{g}(\mathbf{r}, \mathbf{r} + \delta, \tau) = -\left\langle T_\tau \Psi_\mathbf{r}(\tau) \Psi_{\mathbf{r}+\delta}^\dagger(0) \right\rangle \tag{4.6}$$

with spinor,

$$\Psi_\mathbf{r}^\dagger = \left(c_{\mathbf{r},\uparrow}^\dagger, c_{\mathbf{r},\downarrow}^\dagger, c_{\mathbf{r},\downarrow}, c_{\mathbf{r},\uparrow} \right) \tag{4.7}$$

The Green's functions in Eq.4.5 are calculated by diagonalizing the Hamiltonian
(Eq.4.1). This produces energy eigenvalues E_k and eigenvectors $u_{mk}(\mathbf{r})$, so that
the Green's functions can be calculated as:

$$g_{mn}^r(\mathbf{r}, \mathbf{r}', \omega) = \sum_k \frac{u_{mk}(\mathbf{r})u_{nk}^*(\mathbf{r}')}{\omega - E_k + i\delta} \tag{4.8}$$

$$g_{mn}^a(\mathbf{r}, \mathbf{r}', \omega) = \sum_k \frac{u_{mk}(\mathbf{r})u_{nk}^*(\mathbf{r}')}{\omega - E_k - i\delta} \tag{4.9}$$

$$g_{mn}^<(\mathbf{r}, \mathbf{r}', \omega) = 2\pi i n_F(\omega) \sum_k u_{mk}(\mathbf{r})u_{nk}^*(\mathbf{r}')\delta(\omega - E_k) \tag{4.10}$$

We are considering superconducting correlations between nearest-neighbor
sites only, as would be expected, for example, for a triplet superconductor with
a $(p_x + ip_y)$-wave symmetry. Similarly, the local spatial correlations in the super-
conducting spin-singlet channel with s-wave symmetry are obtained via

$$\langle c_{\mathbf{r}+\delta,\uparrow}c_{\mathbf{r},\downarrow}\rangle - \langle c_{\mathbf{r}+\delta,\downarrow}c_{\mathbf{r},\uparrow}\rangle = \frac{1}{2\pi i}\int d\omega[g_{24}^<(\mathbf{r}, \mathbf{r} + \delta, \omega) - g_{13}^<(\mathbf{r}, \mathbf{r} + \delta, \omega)] \tag{4.11}$$

The spatial form of the local superconducting correlations in the s-wave chan-
nel are shown in Fig. 4.4e, and for the real and imaginary parts of $\langle c_{\mathbf{r}+\delta,\uparrow}c_{\mathbf{r},\uparrow}\rangle$ in
Figs. 4.4g and h, respectively.. The real and imaginary parts of $\langle c_{\mathbf{r}+\delta,\downarrow}c_{\mathbf{r},\downarrow}\rangle$ and of
$\langle c_{\mathbf{r}+\delta,\uparrow}c_{\mathbf{r},\downarrow}\rangle + \langle c_{\mathbf{r}+\delta,\downarrow}c_{\mathbf{r},\uparrow}\rangle$ are shown in Fig. 4.5a-b, and Figs.4.5c-d, respectively. To

spatially image these correlations via JSTS, the superconducting order parameter

in the JSTS tip needs to possess the same symmetry and spin-structure as the

correlations we intend to probe. The spin-singlet, s-wave channel was previously

described in Chapter 1 (see also [90]). For that case, a JSTS tip ending in a single

site is sufficient to probe the s-wave correlations, and the resulting spatial structure

of the critical Josephson current, I_c, is shown in Fig. 4.4. In contrast, the triplet

superconducting correlations are by definition odd in real space, implying that they

are non-local. To probe them via JSTS thus requires a tip that also exhibits a non-

local superconducting order parameter (similar to the case of a $d_{x^2-y^2}$-wave order

parameter, discussed in chapter 2). This implies that the JSTS tip has to end in

at least 2 sites from which electrons can tunnel into the system, a case we will

consider in the following (we refer to such a JSTS tip as a 2-site tip). As in chapter

2 (see also [91]), using tips with a larger number of end sites does not change

our qualitative conclusions. Assuming equal-spin-pairing states $|\uparrow\uparrow\rangle$ and $|\downarrow\downarrow\rangle$,

and the opposite spin-pairing state $|\uparrow\downarrow\rangle + |\downarrow\uparrow\rangle$ in the tip then leads to the follow-

ing expressions for the critical Josephson current between the tip and the system,

respectively,

$$
\begin{aligned}
I_c^{\uparrow\uparrow} &= \frac{ie}{\hbar} \sum_{\mathbf{r}_t,\mathbf{r}_t',\mathbf{r}_s,\mathbf{r}_s'} \int \frac{d\omega}{2\pi} [g_{14}^r(\mathbf{r}_t',\mathbf{r}_t,\omega)g_{41}^<(\mathbf{r}_s,\mathbf{r}_s',\omega) + g_{14}^<(\mathbf{r}_t',\mathbf{r}_t,\omega)g_{41}^a(\mathbf{r}_s,\mathbf{r}_s',\omega) \\
&\qquad + g_{14}^r(\mathbf{r}_s',\mathbf{r}_s,\omega)g_{41}^<(\mathbf{r}_t,\mathbf{r}_t',\omega) + g_{14}^<(\mathbf{r}_s',\mathbf{r}_s,\omega)g_{41}^a(\mathbf{r}_t,\mathbf{r}_t',\omega)] \\
I_c^{\downarrow\downarrow} &= \frac{ie}{\hbar} \sum_{\mathbf{r}_t,\mathbf{r}_t',\mathbf{r}_s,\mathbf{r}_s'} \int \frac{d\omega}{2\pi} [g_{23}^r(\mathbf{r}_t',\mathbf{r}_t,\omega)g_{32}^<(\mathbf{r}_s,\mathbf{r}_s',\omega) + g_{23}^<(\mathbf{r}_t',\mathbf{r}_t,\omega)g_{32}^a(\mathbf{r}_s,\mathbf{r}_s',\omega) \\
&\qquad + g_{23}^r(\mathbf{r}_s',\mathbf{r}_s,\omega)g_{32}^<(\mathbf{r}_t,\mathbf{r}_t',\omega) + g_{23}^<(\mathbf{r}_s',\mathbf{r}_s,\omega)g_{32}^a(\mathbf{r}_t,\mathbf{r}_t',\omega)] \\
I_c^{\uparrow\downarrow+\downarrow\uparrow} &= \frac{ie}{\hbar} \sum_{\mathbf{r}_t,\mathbf{r}_t',\mathbf{r}_s,\mathbf{r}_s'} \int \frac{d\omega}{2\pi} [g_{24}^r(\mathbf{r}_t',\mathbf{r}_t,\omega)g_{42}^<(\mathbf{r}_s,\mathbf{r}_s',\omega) + g_{24}^<(\mathbf{r}_t',\mathbf{r}_t,\omega)g_{42}^a(\mathbf{r}_s,\mathbf{r}_s',\omega) \\
&\qquad + g_{24}^r(\mathbf{r}_s',\mathbf{r}_s,\omega)g_{42}^<(\mathbf{r}_t,\mathbf{r}_t',\omega) + g_{24}^<(\mathbf{r}_s',\mathbf{r}_s,\omega)g_{42}^a(\mathbf{r}_t,\mathbf{r}_t',\omega) \\
&\qquad + g_{13}^r(\mathbf{r}_t',\mathbf{r}_t,\omega)g_{31}^<(\mathbf{r}_s,\mathbf{r}_s',\omega) + g_{13}^<(\mathbf{r}_t',\mathbf{r}_t,\omega)g_{31}^a(\mathbf{r}_s,\mathbf{r}_s',\omega) \\
&\qquad + g_{13}^r(\mathbf{r}_s',\mathbf{r}_s,\omega)g_{31}^<(\mathbf{r}_t,\mathbf{r}_t',\omega) + g_{13}^<(\mathbf{r}_s',\mathbf{r}_s,\omega)g_{31}^a(\mathbf{r}_t,\mathbf{r}_t',\omega)]
\end{aligned}
$$

Here, the sums over r_s, r_s' (r_t, r_t') run over all sites in the system (tip), with a non-zero tunneling amplitude t_{r_t,r_s} ($t_{r_t',r_s'}$) between sites r_s and r_t (sites r_t' and r_s'). Thus, the above equations for the critical Josephson currents are valid for an arbitrary number of sites in the tip. Moreover, we take the tunneling amplitude between sites to be the same for all sites, i.e., $t_{r_t,r_s} = t_0$ if electrons can tunnel between site r_t and r_s. Note that all Greens functions in Eq.4.12 are anomalous, non-local Greens functions.

To image the spatial structure of the non-local triplet correlations, we compute $I_C(\mathbf{r})$ using an extended (2×1) JSTS tip with a superconducting triplet order parameter. We assume that the 2-site JSTS tip is always perfectly aligned with the bond connecting two nearest-neighbor sites in the triangular lattice. If the tip's order parameter is chosen to be either purely real (see Fig. 4.4i) or purely imaginary (see Fig. 4.4j), the resulting Josephson current very well images the spatial structure of the real or imaginary parts, respectively, of the superconducting triplet correlations. We note that these triplet correlations can be imaged despite the fact that the MSH system possesses neither a long-range nor a local triplet superconducting order parameter. Thus JSTS can provide unprecedented insight into the existence of one of the most crucial aspects of topological superconductivity, the existence of spin-triplet correlations. Finally, the Josephson current is given by $I_J = I_c \sin(\Delta \psi)$ where $\Delta \psi$ is the spatially-invariant phase difference between the superconducting order parameters in the tip and the system. To compute the Greens function of the 2-site JSTS tip, we consider for simplicity the two cases where the triplet superconducting order parameter in the tip is either completely real or completely imaginary. Note that in an infinitely large square lattice with a $(p_x + ip_y)$-wave superconducting order parameter, such a change in the phase of the triplet superconducting order parameter can be achieved by rotating the lattice by $\pi/2$. To compute the non-local

anomalous Greens function for the two sites at the tip end, we use

$$g_{nm}^{r,a}(\mathbf{r}_t, \mathbf{r}_t', \omega) = \int \frac{d^2k}{(2\pi)^2} \frac{\Delta(\mathbf{k})e^{ik_i}}{(\omega \pm i\delta)^2 - \epsilon(\mathbf{k})^2 - |\Delta(\mathbf{k})|^2} \qquad (4.12)$$

$$g_{nm}^{<}(\mathbf{r}_t, \mathbf{r}_t', \omega) = -n_F(\omega)[g_{nm}^r(\mathbf{r}_t, \mathbf{r}_t', \omega) - g_{nm}^a(\mathbf{r}_t, \mathbf{r}_t', \omega)] \qquad (4.13)$$

where

$$\epsilon(\mathbf{k}) = -2t(\cos k_x + \cos k_y) - \mu; \qquad \Delta(\mathbf{k}) = -i\frac{\Delta_0}{2}(\sin k_x + i\sin k_y) \qquad (4.14)$$

with $\mu = -0.3t$, $\Delta_0 = 0.3t$. The indices (n,m) denote the spin structure of the superconducting gap in the JSTS tip. For $k_i = k_x$, the superconducting order parameter along the bond of the 2-site tip is real, for $k_i = k_y$, it is imaginary. In Figs. 4.4i-j, we denote these two cases by $\Delta_{\text{tip}} = \Delta_p$ and $\Delta_{\text{tip}} = i\Delta_p$, respectively. Our results imply that by changing the phase of the superconducting order parameter in the tip, we can probe the real and imaginary parts of the triplet superconducting correlations in the system. These results can be straightforwardly generalized to an arbitrary complex order parameter in the tip. In Figs.4.5f-g, we present the critical Josephson current in the $|\downarrow\downarrow\rangle$ channel for $\Delta_{\text{tip}} = i\Delta_p$ and $\Delta_{\text{tip}} = \Delta_p$,respectively, while in Figs.4.5h-i, we show I_c in the opposite spin-pairing state ($|\uparrow\downarrow\rangle + |\downarrow\uparrow\rangle$ for $\Delta_{\text{tip}} = i\Delta_p$ and $\Delta_{\text{tip}} = \Delta_p$, respectively. For the 2-site tip, we plot the corresponding $I_c(\mathbf{r})$ as a bond quantity. For all of these cases, the spatial form of the critical current very well images that of the superconducting triplet correlations. For comparison, we also present the spatial structure of the superconducting s-wave order parameter, $\Delta(\mathbf{r})$ (see Fig. 4.5e) and the corresponding $I_c(\mathbf{r})$ (see Fig. 4.5j).

As we have seen, magnetic-superconductor hybrid systems like skyrmions possess a rich topological phase diagram. By varying the skyrmion radius through an externally applied magnetic field, these systems can be tuned into different topological phases and through topological phase transitions. This tuning is possible because of a spatially inhomogenous Rashba spin-orbit interaction that is induced by the magnetic skyrmion lattice and which carries a spatial signature in the zero-energy LDOS that can be observed at a topological phase transition. Skyrmions offer a possible venue to engineer Majorana zero modes and chiral Majorana edge currents, but these features can be notoriously hard to measure. As an avenue to investigate these systems experimentally, we have shown that JSTS is able to visualize the MSH's underlying spin-triplet superconducting correlations. The detail of the information that JSTS can provide varies according to how feasible microscopic manipulations of the tip are, however, it's ability to detect both real and imaginary superconducting correlations via a $90°$ rotation between the tip and the system could offer a precise way to detect and study topological superconductivity.

Chapter 5

Engineering zero-energy modes in FeSe$_{0.45}$Te$_{0.55}$

This chapter was previously published as:

Z. Wang, J. O. Rodriguez, L. Jiao, S. Howard, M. Graham, G. D. Gu, T. L. Hughes, D. K. Morr, and V. Madhavan, "Evidence for dispersing 1D Majorana channels in an iron-based superconductor," Science, vol. 367, no. 6473, pp. 104–108, 2020.

5.1   Background

In recent years, the realization of Majorana zero modes, strong candidates for qubit registers in topological quantum computing[66], has been greeted with much excitement. Evidence for these unique emergent modes has been observed in numerous 1D and 2D topological superconductors[67, 69, 70, 71, 75, 76], where zero-energy states are typically identified via spectroscopic measurements[68, 77, 72, 73]. Recently, the iron-based superconductor FeSe$_{0.45}$Te$_{0.55}$ has been predicted to host topological superconductivity, as indicated by the observation of a Dirac

cone[92], vortex core measurements[72, 73], and topological edge modes[18, 77]. In addition, this material has a number of features that make it experimentally attractive including a large superconducting gap (on the order of a few meV[20]), ease of thin-film fabrication[93], and the ability to modify T_C by doping, pressure, and strain[93, 94]. Despite strong experimental and theoretical interest, however, the microscopic mechanism underlying the onset of topological superconductivity remains unclear. Furthermore, the spectroscopic identification of Majorana zero modes in this system is complicated by the presence of defect-induced trivial states close to zero energy. In this chapter, we address these outstanding questions by proposing a magnetic-superconductor hybrid model for topological superconductivity in FeSe$_{0.45}$Te$_{0.55}$, contrast the zero-energy Majorana modes it can host with trivial defect-induced states close to zero energy, and propose a method to distinguish between them.

5.2   A 5-band model for FeSeTe

To begin, we consider a topologically trivial 5-band model that has been established to match differential conductance measurements on FeSe$_{0.45}$Te$_{0.55}$[20], with an experimentally-consistent definition of the superconducting order parameter[1] and Fermi surface[19].

In real space, the Hamiltonian is given by,

$$
\begin{aligned}
H =& H_0 + H_{\text{SC}}^{\text{MF}} \\
H_0 =& \sum_{\mathbf{r},\sigma} \sum_{\alpha=1}^{5} (\epsilon_{\alpha\alpha} - \mu) c_{\mathbf{r},\alpha,\sigma}^{\dagger} c_{\mathbf{r},\alpha,\sigma} - \sum_{\mathbf{r},\mathbf{r}',\sigma} \sum_{\alpha,\beta=1}^{5} t_{\mathbf{r},\mathbf{r}'}^{\alpha\beta} c_{\mathbf{r},\alpha,\sigma}^{\dagger} c_{\mathbf{r}',\beta,\sigma} \\
H_{\text{SC}}^{\text{MF}} =& \sum_{\langle\mathbf{r},\mathbf{r}'\rangle} \sum_{\alpha=1}^{5} \Delta_{\alpha\alpha} c_{\mathbf{r},\alpha,\uparrow}^{\dagger} c_{\mathbf{r}',\alpha,\downarrow}^{\dagger} + \text{H.c.}
\end{aligned}
\tag{5.1}
$$

where $\alpha, \beta = 1, ..., 5$ are the orbital indices corresponding to the d_{xz}-, d_{yz}-, $d_{x^2-y^2}$-, d_{xy}-, and $d_{3z^2-r^2}$-orbitals, respectively, $-t_{\mathbf{r},\mathbf{r}'}^{\alpha\beta}$ represents the electronic hopping amplitude between orbital α at site $\mathbf{r}$ and orbital β at site $\mathbf{r}'$, $\epsilon_{\alpha\alpha}$ is the on-site energy of orbital α, μ represents the overall chemical potential, and $c_{\mathbf{r},\alpha,\sigma}^{\dagger}(c_{\mathbf{r},\alpha,\sigma})$ creates (annihilates) an electron with spin σ at site $\mathbf{r}$ in orbital α. $-t_{\mathbf{r},\mathbf{r}'}^{\alpha\beta}$ is nonzero to the fifth-nearest neighbor, where $|\mathbf{r} - \mathbf{r}'| = 3$.

In momentum space, the hopping parameters lead to the following dispersions:

$$\varepsilon_{11/22}(\mathbf{k}) = 2t_{x/y}^{11} \cos k_x + 2t_{y/x}^{11} \cos k_y + 4t_{xy}^{11} \cos k_x \cos k_y \pm 2t_{xx}^{11}(\cos 2k_x - \cos 2k_y)$$
$$+ 4t_{xxy/xyy}^{11} \cos 2k_x \cos k_y + 4t_{xyy/xxy}^{11} \cos 2k_y \cos k_x + 4t_{xxyy}^{11} \cos 2k_x \cos 2k_y$$

$$\varepsilon_{33}(\mathbf{k}) = 2t_x^{33}(\cos k_x + \cos k_y) + 4t_{xy}^{33} \cos k_x \cos k_y + 2t_{xx}^{33}(\cos 2k_x + \cos 2k_y)$$

$$\varepsilon_{44}(\mathbf{k}) = 2t_x^{44}(\cos k_x + \cos k_y) + 4t_{xy}^{44} \cos k_x \cos k_y + 2t_{xx}^{44}(\cos 2k_x + \cos 2k_y)$$
$$+ 4t_{xxy}^{44}(\cos 2k_x \cos k_y + \cos 2k_y \cos k_x) + 4t_{xxyy}^{44} \cos 2k_x \cos 2k_y$$

$$\varepsilon_{55}(\mathbf{k}) = 2t_x^{55}(\cos k_x + \cos k_y) + 2t_{xx}^{55}(\cos 2k_x + \cos 2k_y)$$
$$+ 4t_{xxy}^{55}(\cos 2k_x \cos k_y + \cos 2k_y \cos k_x) + 4t_{xxyy}^{55} \cos 2k_x \cos 2k_y$$

$$\varepsilon_{12}(\mathbf{k}) = - 4t_{xy}^{12} \sin k_x \sin k_y - 4t_{xxy}^{12}(\sin 2k_x \sin k_y + \sin 2k_y \sin k_x) - 4t_{xxyy}^{12} \sin 2k_x \sin 2k_y$$

$$\varepsilon_{13/23}(\mathbf{k}) = \pm 2it_x^{13} \sin k_{y/x} \pm 4it_{xy}^{13} \sin k_{y/x} \cos k_{x/y} \mp 4it_{xxy}^{13}(\sin 2k_{y/x} \cos k_{x/y} - \cos 2k_{x/y} \sin k_{y/x})$$

$$\varepsilon_{14/24}(\mathbf{k}) = 2it_x^{14} \sin k_{x/y} + 4it_{xy}^{14} \cos k_{y/x} \sin k_{x/y} + 4it_{xxy}^{14} \sin 2k_{x/y} \cos k_{y/x}$$

$$\varepsilon_{15/25}(\mathbf{k}) = 2it_x^{15} \sin k_{y/x} - 4it_{xy}^{15} \sin k_{y/x} \cos k_{x/y} - 4it_{xxyy}^{15} \sin 2k_{y/x} \cos 2k_{x/y}$$

$$\varepsilon_{34}(\mathbf{k}) = 4t_{xy}^{34}(\sin 2k_y \sin k_x - \sin 2k_x \sin k_y)$$

$$\varepsilon_{35}(\mathbf{k}) = 2t_x^{35}(\cos k_x - \cos k_y) + 4t_{xxy}^{35}(\cos 2k_x \cos k_y - \cos 2k_y \cos k_x)$$

$$\varepsilon_{45}(\mathbf{k}) = 4t_{xy}^{45} \sin k_x \sin k_y + 4t_{xxyy}^{45} \sin 2k_x \sin 2k_y$$

The onsite orbital energies are given by $\epsilon_1 =$ 7.0 meV, $\epsilon_2 =$7.0meV, $\epsilon_3 =$-25.0meV, $\epsilon_4 =$20.0meV, and $\epsilon_5 =$-25.1 meV, while the hopping parameters are given in tables

t_i^{mm}	$i = x$	$i = y$	$i = xy$	$i = xx$	$i = xxy$	$i = xyy$	$i = xxyy$
$m = 1$	-11.0	-43.0	28.0	2.0	-3.5	0.5	3.5
$m = 3$	32.0		-10.5	-2.0			
$m = 4$	22.0		15.0	-2.0	-3.0		-3.0
$m = 5$	-10.0			-4.0	2.0		-1.0

Table 5.1: Intra-orbital hoppings (meV) for the FeSe$_{0.45}$Te$_{0.55}$ 5-band model

t_i^{mm}	$i = x$	$i = xy$	$i = xxy$	$i = xxyy$
$mm = 12$		5.0	-1.5	3.5
$mm = 13$	-35.4	9.9	2.1	
$mm = 14$	33.9	1.4	2.8	
$mm = 15$	-19.8	-8.5		-1.4
$mm = 34$			-1.0	
$mm = 35$	-30.0		-5.0	
$mm = 45$		-15.0		1.0

Table 5.2: Inter-orbital hoppings (meV) for the FeSe$_{0.45}$Te$_{0.55}$ 5-band model

5.1 and 5.2.

To obtain the mean-field form of H_{SC} given in Eq. 5.1, we decouple the super-conducting pairing interaction,

$$H_{\text{SC}} = -\sum_{\langle \mathbf{r}, \mathbf{r}' \rangle} \sum_{\alpha=1}^{5} I_{\mathbf{r},\mathbf{r}'}^{\alpha} c_{\mathbf{r},\alpha,\uparrow}^{\dagger} c_{\mathbf{r}',\alpha,\downarrow}^{\dagger} c_{\mathbf{r},\alpha\downarrow} c_{\mathbf{r}',\alpha,\uparrow}$$

such that,

$$\Delta_{\alpha\alpha} = I_{\mathbf{r},\mathbf{r}'}^{\alpha} \langle c_{\mathbf{r}\alpha\downarrow} c_{\mathbf{r}'\alpha\uparrow} \rangle = I_{\mathbf{r},\mathbf{r}'}^{\alpha} \langle c_{\mathbf{r}\alpha\uparrow}^{\dagger} c_{\mathbf{r}'\alpha\downarrow}^{\dagger} \rangle$$

and set the intra-orbital superconducting order parameters to match the three spectroscopically-observed coherence peaks,

$$\Delta_{xz} = \Delta_{yz} = 0.55\text{meV}$$

$$\Delta_{xy} = 0.38\text{meV}$$

with $\Delta_{\alpha\beta} = 0$ in all other orbitals. Assuming pairing between next-nearest Fe sites (with hopping parameters aligned with the square Fe-Fe lattice) then yields an $s_{\pm}$-wave order parameter.

5.3 Evidence for dispersing 1D Majorana channels in a 1D iron-based superconductor

In a recent measurement on FeSe$_{0.45}$Te$_{0.55}$, 1D dispersing Majorana modes were reported near a domain-wall defect[77]. This defect was discovered with atomically resolved topography as a 1D feature on the surface represented by a bright line (Fig. 5.1A). A zoomed-in view (Fig. 5.1D) reveals that this bright line separates two crystal domains where the lattice shows a relative phase shift. This shift is reflected as a split in reciprocal-space Bragg peaks of the Fourier transform of the image (Fig. 5.1). The magnitude of the split in reciprocal space corresponds to a spatial scale of 12 nm (half of the field of view of Fig. 5.1), which is consistent with the domain size in this FOV. Accompanying the split, a displacement analysis indicated that the lattice underwent a half-unit-cell shift at the crystal domain wall. In comparison to other crystallographic defects, this half-unit-cell shift was essential for the realization of dispersing Majorana modes.

Differential conductance spectra obtained along three distinct paths traversing the domain wall (Fig. 5.1F) reveal an intriguing evolution. As one approaches the domain wall, the superconducting coherence peaks in the dI/dV spectra are suppressed and new electronic states emerge inside the gap, resulting in a nearly featureless, constant finite dI/dV inside the gap at the domain wall center as indicated with the highlighted lines in Fig. 5.1F, inset. Despite the constant DOS inside the superconducting gap, the DOS at the domain wall still exhibits supercon-
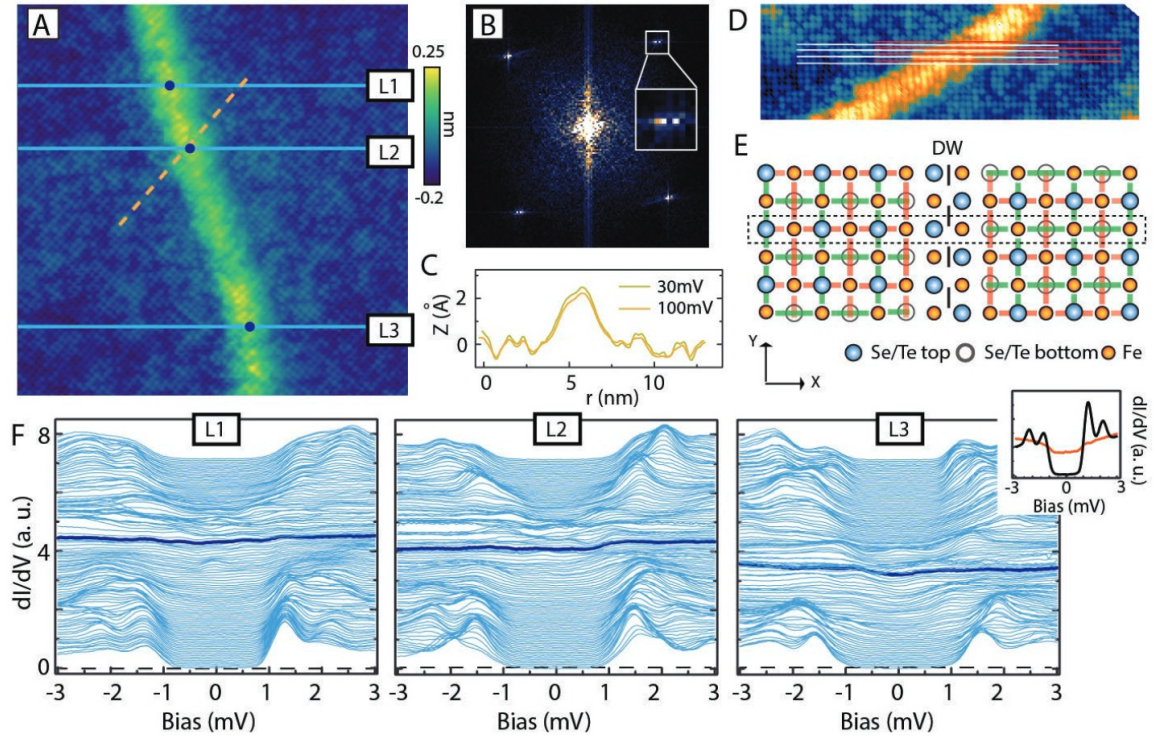
Figure 5.1: Signature of dispersing 1D Majorana modes on a domain wall. a. 25nm X 25nm topographic image showing a domain wall. b. 2D FFT of a, showing the splitting of the Bragg peaks which indicates the presence of domains in this image. Inset: zoom-in near one of the Bragg peaks. c. Height scans taken at different bias voltage along the yellow dashed line in a. d. Zoom in of the domain wall. The dashed lines track the atomic lattice on both sides of the domain wall. A half-unit cell shift can be observed between one side and the other. e. Schematic of the half unit cell shift across the domain wall. The schematic also depicts how one might obtain a π-phase in the superconducting order parameter shift across such a domain wall. Superimposed on the lattice are red and green bars, which denote the parity of next-nearest neighbor pairing[95, 1]. Concentrating now on the atoms inside the dashed box, one observes that the parity shifts from red on the left of the domain wall, to green on the right. This creates a π-phase shift in the superconducting order parameter. f. Linecut profiles of dI/dV spectra along the three blue lines in a (L1, L2 and L3 shown in sequence from left to right), which cross the domain wall. The spectra shape obtained right on the domain wall (at position of dots in a) are highlighted with a dark blue color. A direct comparison of the spectra taken on the domain wall (orange) and far away (dark) is shown in the inset.

ducting signatures (Fig. 5.1F and inset), which indicates that the flat DOS is not simply caused by a region of normal metal. One explanation for this observation

is the presence of linearly dispersing Majorana states at the domain wall because it would naturally give rise to a constant dI/dV in one dimension. According to the Fu-Kane model [96], realizing 1D dispersing Majorana states requires three ingredients: nontrivial topological surface states, s-wave superconductivity that gaps the surface states, and a π-phase shift in the superconducting order parameter across the domain wall. Detailed gap maps already indicate the presence of proximity-gapped Dirac surface states, thus satisfying the first two criteria. This leaves us with the question of how to generate a superconducting phase shift. For the pairing symmetries allowed in Fe(Se,Te), it is possible to have an interplay between the crystal structure and the phase of the superconducting order parameter. One possibility comes from the predicted odd parity s-wave pairing in iron-based superconductors, which encodes pairing between next-nearest-neighbor sites [95, 97] in the 2-Fe unit cell. In this case, the order parameters on the two Fe-sublattices have a π-phase difference. A half-unit-cell shift of the lattice in such a system would naturally create a π-phase shift across the domains (Fig. 5.1E). It has also been argued that the s$\pm$ pairing in iron-based superconductors can generate a π-phase shift at the intersections of crystal terminations with different orientations [98]. Thus, Fe(Se,Te) is an excellent candidate, with all the essential ingredients necessary for hosting dispersing Majorana modes.

One might wonder whether the experimentally observed domain wall modes could also possess a topologically trivial origin, unrelated to existence of a topological surface state. On the basis of previous studies, the superconducting order parameter in Fe(Se,Te) is expected to be a sign-changing s$\pm$ state [99, 1]. In such a state, defects, regardless of their magnetic properties, would induce impurity states inside the superconducting gap. The experimentally observed domain wall representing a 1D defect could therefore lead to the emergence of an impurity band inside the superconducting gap even in a topologically trivial phase. To

distinguish this possibility from other scenarios, we studied other extended defects (Section 5.4) that are not expected to give rise to a π-phase shift and found that the flat DOS signature is absent; 1D defects without the half-unit-cell shift have the effect of decreasing the gap magnitude, whereas step edges, which are strong potential scatterers, induce resonant bound states inside the superconducting gap (Fig. 5.2).

To investigate this, we used a theoretical model for a topologically trivial super-conducting state of Fe(Se,Te) [20] and represented the domain wall as a line of potential scatterers (Fig. 5.3). We found, as expected, that the domain wall gives rise to impurity states inside the superconducting gap. However, these states do not in general traverse the superconducting gap (only for fine-tuned values of the scattering potential do impurity states near zero energy emerge). Moreover, such states are not uniformly distributed in energy inside the gap and cannot result in the observed constant density of states. The same conclusion holds if the domain wall-separated, π-phase–shifted superconducting regions are present in an otherwise topologically trivial phase. Although such domain walls give rise to a suppression of the superconducting gap, they do not result in a constant DOS. These theoretical and experimental findings, taken together, make it unlikely that the observed constant DOS near the domain wall can arise in a topologically trivial superconducting phase, which further emphasizes the important role played by nontrivial topology of FeSe$_{0.45}$Te$_{0.55}$ in creating the observed domain wall modes.

5.4   Domain walls in the topologically trivial model

To model a step-edge boundary in the model presented in Section5.2, in which a Dirac cone is absent, we introduce an on-site non-magnetic scattering defect given

by

$$H_{\text{scat}} = \sum_{\mathbf{R},\sigma} \sum_{\alpha=1}^{5} U_0 c_{\mathbf{R},\alpha,\sigma}^{\dagger} c_{\mathbf{R},\alpha,\sigma} \ . \tag{5.2}$$

where the sum runs over all defect sites in a line along the crystal axis. The total Hamiltonian in real space in the superconducting state is then given by $H = H_0 + H_{\text{SC}}^{\text{MF}} + H_{\text{scat}}$. Using Nambu spinors $\Psi^{\dagger}, \Psi$, the Hamiltonian can be written as

$$H = \Psi^{\dagger} \hat{H} \Psi \tag{5.3}$$

Diagonalization of $\hat{H}$ then yields the eigenenergies of the system. The local, orbitally-summed density of states is then obtained from

$$N(\mathbf{r}, E) = -\frac{1}{\pi} \sum_{\alpha} \text{Im} G_{\alpha,\alpha}(\mathbf{r}, \mathbf{r}, E) \tag{5.4}$$

where $G_{\alpha,\alpha}(\mathbf{r}, \mathbf{r}, E)$ is the local retarded Greens function of orbital α. These are given as the diagonal elements of the Greens function matrix

$$\hat{G}^{-1} = (\omega + i\delta)\hat{1} - \hat{H} \tag{5.5}$$

In Fig. 5.2(a), we present the lowest eigenenergies of the system as a function of the defect line's scattering strength, U_0. For comparison, we present the DOS of the clean system in Fig.5.2(b). With increasing U_0, impurity states are pulled into the gap, and cross zero energy around $U_0 \approx 60$ meV and $U_0 \approx 90$ meV. However, the defect line does not give rise to generic (or symmetry protected) zero energy states – thus, as expected, this topologically trivial model cannot support the in-gap modes observed in Fig. 5.1.

Next, we consider the effects of a linear domain wall in the superconductor that
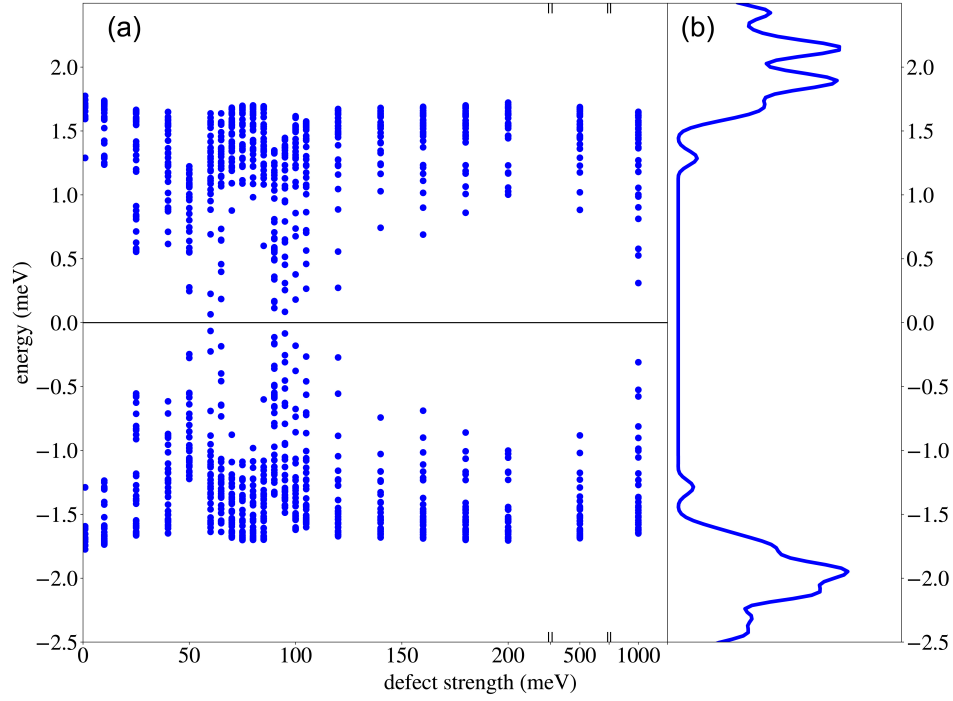
Figure 5.2: Eigenenergies of a 1D potential scattering line defect (a) Lowest-energy electronic states for a 121x121-site system, as a function of the defect line's scattering strength U_0. (b) Density of states spectra for a clean system.

separates two regions in which the SCOPs possess a π-phase shift, and hence differ in their overall sign. In this case, the SCOP is position-dependent,

$$H_{\text{SC}}^{\text{MF}} \rightarrow H_{\text{SC(r)}}^{\text{MF}} = \sum_{\langle \mathbf{r},\mathbf{r}' \rangle} \sum_{\alpha=1}^{5} \Delta_{\alpha\alpha}(\mathbf{r}) c_{\mathbf{r},\alpha,\uparrow}^{\dagger} c_{\mathbf{r}',\alpha,\downarrow}^{\dagger} + H.c. \tag{5.6}$$

Such that the full Hamiltonian for the topologically trivial π-phase shift is,

$$H = H_0 + H_{\text{SC(r)}}^{\text{MF}}$$

Fig.   5.3(a), presents the LDOS near the domain wall [Fig.5.3(b) shows a
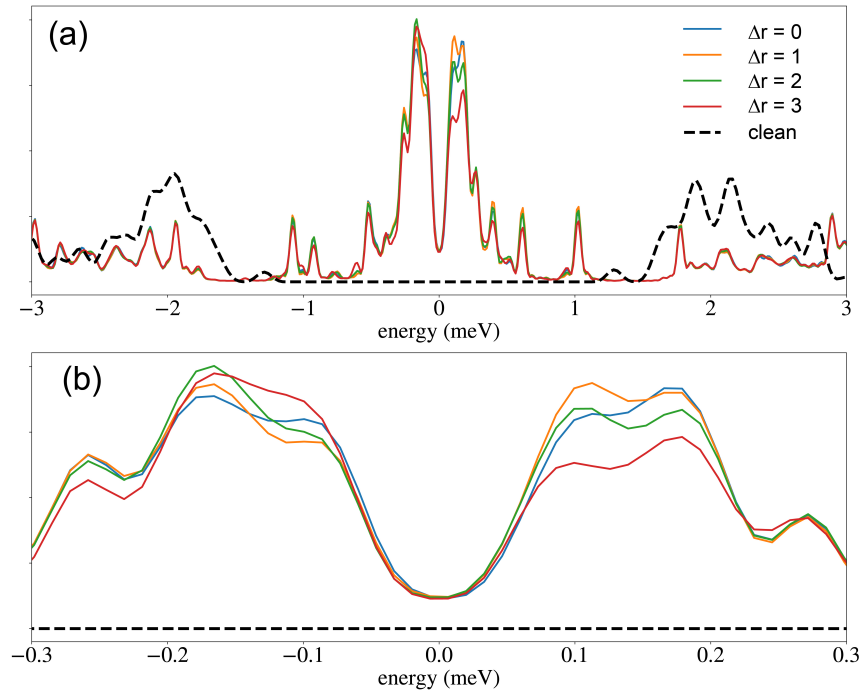
Figure 5.3: (a) Orbitally-summed LDOS $N(\mathbf{r}, E)$ at various distances from the π-phase domain wall. The LDOS for a clean system (dashed line) is provided as a guide to the eye. (b) Zoom-in of the results shown in (a).

zoomed-in view]. While the π-phase domain wall created here clearly leads to the emergence of in-gap states, these in-gap states are located at finite energy (we do not find that these energy states move to lower energies with increasing system size). Thus, a topologically trivial π-phase domain wall does not lead to the emergence of generic zero-energy states (though states can be located close to the zero energy).

5.5   Revising the 5-band model

As we have seen, the 1D defects in Section 5.4 were unable to recreate the broadly dispersing Majorana modes found in FeSe$_{0.45}$Te$_{0.55}$, further corroborating the explanation that their origin came from the topological surface states that have so far been absent from our model[77]. To further address the question of how to distinguish topological zero-energy states from those that appear in a trivial model, we modify the Hamiltonian from Eq. 5.1 to include two elements which were essential for the engineering of Majorana modes and chiral Majorana currents in the MSH system in chapter 3 and elsewhere[100, 85, 76]: surface magnetism and a non-zero Rashba spin-orbit (RSO) interaction. For FeSe$_x$Te$_{1-x}$, a recent photoemission experiment near T_C[101] has shown evidence consistent with the formation of a ferromagnetic surface layer; there is also strong evidence of short-range magnetism near T_C in the parent compound, FeSe[102]. Correspondingly, recent evidence of inversion symmetry breaking[18] in FeSe$_{0.45}$Te$_{0.55}$ suggests that Rashba spin-orbit coupling is present.

For the purposes of our model we include the Rashba effect and a possible out-of-plane magnetic alignment in each of the 5 orbitals via,

$$\begin{aligned}
H_{\mathsf{RSO}} &= i\alpha \sum_{\mathbf{r},\alpha\beta} c_{\mathbf{r},\alpha}^{\dagger} \left(\hat{\boldsymbol{\delta}} \times \boldsymbol{\sigma} \right)_{\alpha\beta}^{z} c_{\mathbf{r}+\hat{\boldsymbol{\delta}},\beta} \\
H_{\mathsf{J}} &= J \sum_{\mathbf{R},\alpha,\beta} \mathbf{S_R} \cdot c_{\mathbf{R}\alpha}^{\dagger} \boldsymbol{\sigma}_{\alpha\beta} c_{\mathbf{R}\beta} + \mathrm{H.c.}
\end{aligned} \qquad (5.7)$$

Here, α represents the Rashba spin-orbit coupling arising from broken inversion symmetry[18], $\hat{\delta}$ connects nearest-neighbor sites, $\mathbf{S_R}$ is a classical vector denoting the direction of a surface atom's spin at position $\mathbf{R}$ with an exchange coupling J to a conduction electron, and σ is a vector of Pauli matrices. Throughout the following, we assume an out-of-plane magnetic alignment such that $\mathbf{S_R} = \mathbf{S}_{\hat{z}}$. The inclusion
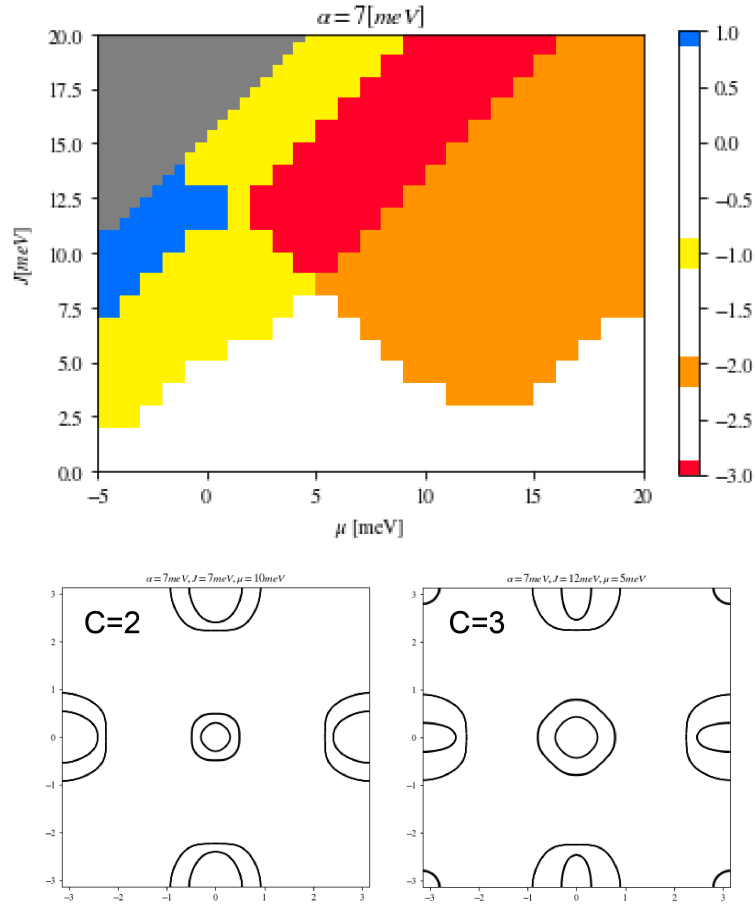
Figure 5.4: Topological phase diagram of FeSe$_{0.45}$Te$_{0.55}$ in the a.) (μ, J)-plane with $\alpha = 7.0$meV. Fermi surfaces are shown for b. $C = 2$ and c. $C = 3$ phases. (Source: Private correspondence with Dirk Morr and Sagen Cocklin, included with permission)

of these contributions leaves us with an overall Hamiltonian,

$$H = H_0 + H_{\mathsf{SC}}^{\mathsf{MF}} + H_{\mathsf{RSO}} + H_{\mathsf{J}} \tag{5.8}$$

To explore the topological phase diagram of this model, the Chern number may be calculated (see Fig. 5.4) as in Chapter 3 using,

$$C = \frac{1}{2\pi} \int_{\text{BZ}} d^2k \text{Tr}(P_{\mathbf{k}}[\partial_{k_x} P_{\mathbf{k}}, \partial_{k_y} P_{\mathbf{k}}]) \tag{5.9}$$

$$P_{\mathbf{k}} = \sum_{E_n(\mathbf{k})<0} |\Psi_n(\mathbf{k})\rangle\langle\Psi_n(\mathbf{k})| \tag{5.10}$$

where $E_n(\mathbf{k})$ and $|\Psi_n(\mathbf{k})\rangle$ are the eigenenergies and the eigenvectors of the Hamiltonian in Eq. 5.8, with n being a band index, and the trace is taken over Nambu and spin-space.

As we can see from Fig. 5.4a, the phase diagram of the modified Hamiltonian now hosts a rich interplay of topological phases, even for relatively small variations in the exchange coupling J. In order to create a domain wall for FeSe$_{0.45}$Te$_{0.55}$ that can support Majorana modes while maintaining close agreement with the spectroscopic accuracy of the model, we take $\mu = 0$, $J = 7.0$meV, $\alpha = 7.5$meV.

5.6   Domain walls in a topological model

To investigate the appearance of Majorana modes across a domain wall, we consider the trivial model with the addition of the Rashba spin-orbit interaction and out-of-plane magnetic moment from Eq. 5.7, in a ribbon geometry. Using parameters $\mu = 0$, $\alpha = 7.0$meV, $J = 7.5$meV places the system in a $C = -1$ phase (see Fig. 5.4). In this case, to maintain the model's agreement with spectroscopically-measured coherence peaks [20], we further modify the orbitally-selective superconducting order parameter such that,

$$\Delta_{xz} = \Delta_{yz} = 1.10\text{meV}$$

$$\Delta_{xy} = 0.76\text{meV}$$

This represents a change from $\Delta_{\alpha\alpha} \to 2\Delta_{\alpha\alpha}$ from the trivial model, and is a consequence of the onset of magnetic pair-breaking effects that were absent from the original time-reversal invariant model presented in section 5.2. Furthermore, propose for comparison a spin-domain wall such that $\mathbf{S_R} \to -\mathbf{S_R}$ across the 1D edge defect. Continuing to use the definition of a 1D π-phase shift in Eq. 5.6, we find (see Fig. 5.5a) several linearly dispersive Majorana modes (solid red lines) for the spin-domain wall, but none for the π-phase domain (although the π-phase domain generates strong spectral weight at zero energy).

To understand this result, we note that bulk-boundary correspondence only requires the emergence of Majorana modes at topological domain edges. In our configuration, the ribbon's periodic boundary conditions generate two domain walls for both the π-phase and spin-domain walls, however only the spin-domain walls are associated with a change in Chern number across the domain. There, the change across the domain wall is entirely due to the change in sign of the magnetic alignment[85]. Corresponding to the move from a $C = -1$ phase with $J = 7.5$meV to $C = +1$ and $J = -7.5$meV, we find a total number of Majorana modes corresponding to $2|\Delta C| = 4$, as expected for two domain walls.

In contrast, the π-phase shift in the SCOP does not change the Chern number, and thus is not associated with a topological domain edge generating a chiral Majorana edge current. Additionally, upon closer examination of the π-phase domain, while the many in-gap bands generate a heavy spectral weight (Fig. 5.5b, d) which is strongly localized at the domain wall (Fig. 5.5f), upper and lower bands do not connect across the Fermi level to form a Dirac cone, instead resulting in other avoided crossings and sometimes small electron- or hole-like pockets.

To more quantitatively investigate the difference between the trivial (π-phase) and topological (spin-reversed) domain walls, we calculate the supercurrents along
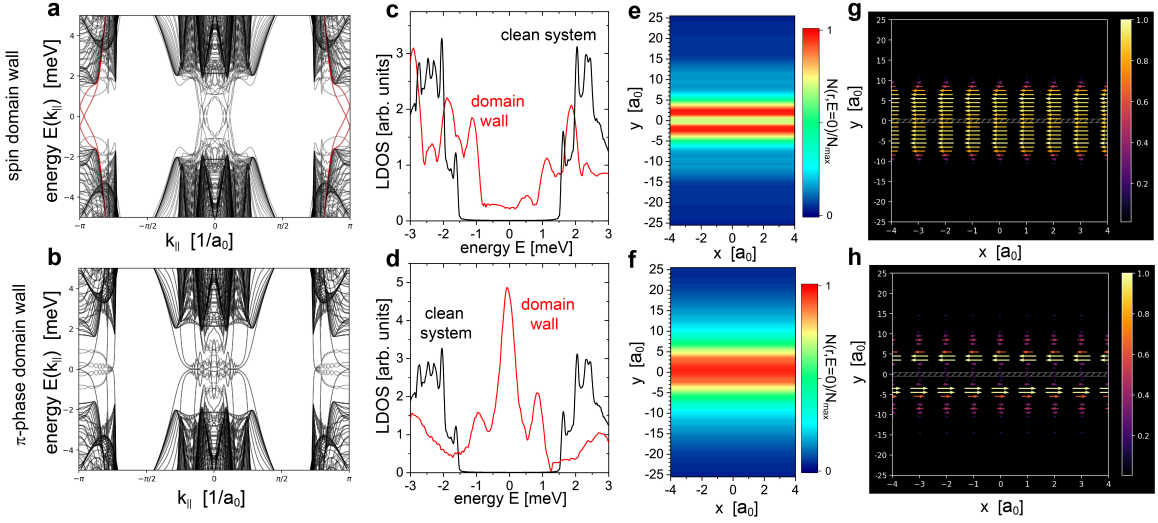
Figure 5.5: Domain walls in the topological FeSe$_{0.45}$Te$_{0.55}$ model with a ribbon geometry. a.) Dispersion in a system with a spin-reversed domain wall ($J \rightarrow -J$) and in b.) a system with a π-phase domain wall ($\Delta_{\alpha\alpha} \rightarrow -\Delta_{\alpha\alpha}$). The two The LDOS across the domain walls are shown for the spin-reversed and π-phase walls as a function of energy in c.) and d.) respectively, and the spatial distribution of spectral weight at $E = 0$ is shown in e.) for the spin-reversed wall and f.) for the π-phase domain wall. The equilibrium current at the domain wall edge is shown in g.) for the spin-reversed domain wall and h.) for the π-phase domain wall.

the domain wall edges, using

$$I_{\alpha\beta} = -\frac{2e}{\hbar} \int \frac{d\omega}{2\pi} \text{Re} \left[t_{\alpha\beta} G^{<}_{\alpha\beta}(\mathbf{r}, \mathbf{r} + \hat{\mathbf{x}}, \omega) \right] \qquad (5.11)$$

Where $t_{\alpha\beta}$ corresponds to the electronic hopping connecting bands α, β along the direction parallel to the domain wall, and $G^{<}_{\alpha\beta}(\mathbf{r}, \mathbf{r} + \hat{\mathbf{x}}, \omega)$ is the lesser Green's function connecting $\mathbf{r}$ and $\mathbf{r} + \hat{\mathbf{x}}$. In our results, these were calculated according to the kernel polynomial method[103] for a 64x64-site system with periodic domain walls. Comparison with Tables 5.1 and 5.2 reveals nine non-zero intra- and inter-orbital supercurrents (see Fig. 5.6). Overall, the relative current magnitudes are roughly proportional to each bands' respective hopping elements (note that here the domain wall is aligned with the y-axis), which were pre-determined by matching

a tight-binding model to $FeSe_{0.45}Te_{0.55}$'s band structure. The key feature, shared by the current in all orbitals, is the even (odd) spatial distribution of the current in the spin (π-phase) domain cases.
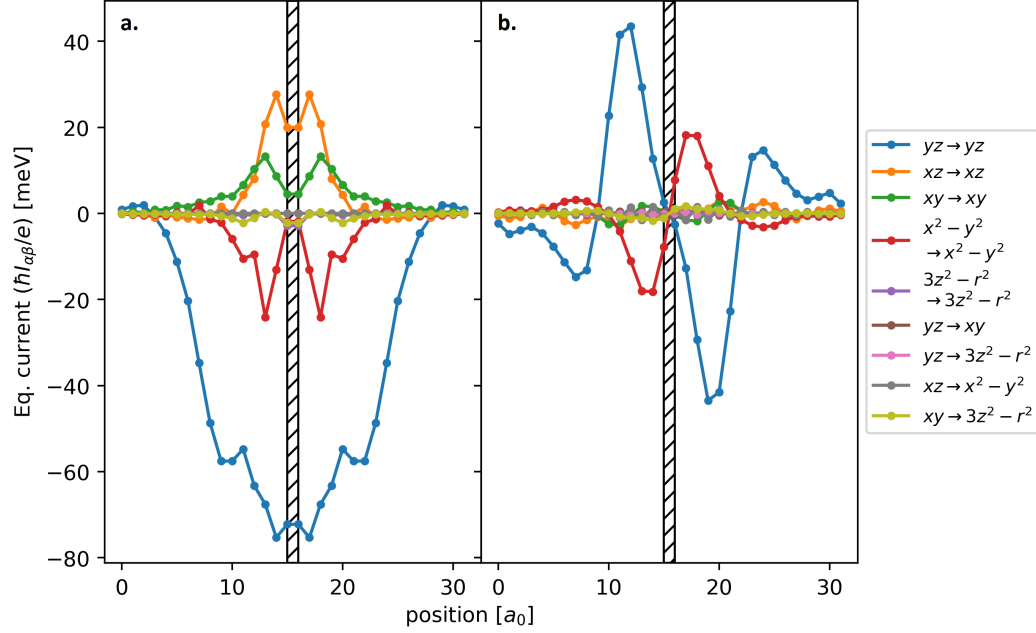
Figure 5.6: Orbitally-resolved equilibrium current parallel to the domain walls for a.) a spin-domain wall configuration and for b.) a π-phase domain wall.

In Fig. 5.5g (spin-domain) and h (π-phase domain), which present the total of the orbitally-resolved currents from Fig. 5.6a and b, we see a crucial difference in behavior that is a direct consequence of the topological phase defined on either side of the domain walls. In the π-phase shift case, the superconductors on opposite sides of the domain wall have an identical Chern number, and thus produce the anti-aligned currents with identical chirality that effectively cancel at the domain wall. In contrast, opposing sides of the spin-domain wall are associated with an opposite Chern number, leading to supercurrents with reversed chirality that combine to produce a non-vanishing supercurrent parallel to the domain wall. This qualitatively different edge current behavior represents a topological signature that can be used to distinguish between near zero-energy trivial states (as in the π-phase

domain considered here) and non-trivial Majorana modes (as in the spin-domain wall case). In the future, we hope that this fundamental difference in edge current behavior will be measured experimentally, since recent superconducting quantum interference device (SQUID) measurements[104] have demonstrated a capability to do so.

Throughout this chapter, we have considered a series of domain wall models of FeSe$_{0.45}$Te$_{0.55}$ in which the presence of Majorana modes is difficult to distinguish from trivial in-gap states located close to zero energy. In the case of the π-phase domain wall specifically, the strong spectral weight in the zero-energy LDOS points toward zero-energy states which, even if they occur within a topologically nontrivial phase, are not necessarily associated with a Majorana zero mode. To address the problem of how to detect topologically non-trivial states in a domain wall configuration like the experiment by Wang, et. al[77], we propose measuring the supercurrent parallel to the domain wall. Within our FeSe$_{0.45}$Te$_{0.55}$ model, we find that topologically distinct domains are associated with a qualitative difference in the supercurrent, allowing for more reliable identification of Majorana modes as compared to STS measurements. Taken together, these results offer an exciting new possibility for the detection and manipulation of the topological edge modes proposed to exist in FeSe$_{0.45}$Te$_{0.55}$.

Chapter 6

Conclusion

In the preceding chapters, we have analyzed a series of novel superconducting systems to find possible experimental signatures of their microscopic behavior. Our overarching findings have been that transport measurements are typically extremely useful for these purposes, if indeed the experimental difficulty of performing them can be overcome. In the case of the BCS superconductor we considered in Chapter 2, we simulated current measurements obtainable through Josephson scanning tunneling spectroscopy. Although this technique itself is well-established, our comparison of the critical current deviations with the s-wave superconducting correlations on the substrate provided a missing proof that the Josephson current could be used to image the superconducting order parameter directly.

Building from the connection between the Josephson current and the superconducting correlations in the s-wave superconductor, we then extended the current calculation to a cuprate model with a non-local, anisotropic order parameter. There, we tested the imaging capability of JSTS extensively using potential and magnetic scattering defects, a spatially oscillating order parameter in the FFLO phase, spatially extended, optionally disordered tips, and a to-scale model of a cuprate's highly localized heterogenous superconducting and pseudogap regions.

Throughout, we found that the critical current generally images the SCOP, offering defining evidence of the FFLO phase and a unique way to test for precursor pairing as a microscopic origin for the cuprates' pseudogap phase.

Recently, the question of how to build a quantum computer has motivated intense study of topological superconductors capable of hosting and manipulating Majorana zero modes. In Chapter 4, we demonstrated an MSH system where tunability can be engineered by an applied magnetic field, generating a complex topological phase diagram. Through application of JSTS to this system, we were able to image the unconventional spin-triplet superconducting correlations that are essential for topological superconductivity. Furthermore, introducing topological superconductivity into a 5-band model of $FeSe_{0.45}Te_{0.55}$ allowed us to discriminate between topologically trivial and non-trivial in-gap states that can be induced along domain walls. Using this model, we showed that the dissimilarity in the equilibrium current between spin-domain and π-phase domain walls can identify whether a chiral Majorana edge mode is present even when it is unclear from the local density of states. Our hope is that these methods of detection will provide an experimentally accessible way to gain insight into the many unique properties of unconventional and topological superconductors.

Chapter 7

Appendix A: Copyright Permissions

21-Jul-2020

This license agreement between the American Physical Society ("APS") and Martin Graham ("You") consists of your license details and the terms and conditions provided by the American Physical Society and SciPris.

Licensed Content Information

License Number:	**RNP/20/JUL/028592**
License date:	21-Jul-2020
DOI:	10.1103/PhysRevLett.123.017001
Title:	Josephson Scanning Tunneling Spectroscopy in ${d}_{{x}^{2}-{y}^{2}}$-Wave Superconductors: A Probe for the Nature of the Pseudogap in the Cuprate Superconductors
Author:	Martin Graham and Dirk K. Morr
Publication:	Physical Review Letters
Publisher:	American Physical Society
Cost:	USD $ 0.00

Request Details

Does your reuse require significant modifications: No

Specify intended distribution locations:	United States
Reuse Category:	Reuse in a thesis/dissertation
Requestor Type:	Author of requested content
Items for Reuse:	Whole Article
Format for Reuse:	Electronic

Information about New Publication:

University/Publisher:	University of Illinois at Chicago
Title of dissertation/thesis:	Imaging Novel States in Unconventional Superconductors
Author(s):	Martin Graham
Expected completion date:	Jul. 2020

License Requestor Information

Name:	Martin Graham
Affiliation:	Individual
Email Id:	graham40@uic.edu
Country:	United States

American Physical Society
Reuse and Permissions License

TERMS AND CONDITIONS

The American Physical Society (APS) is pleased to grant the Requestor of this license a non-exclusive, non-transferable permission, limited to Electronic format, provided all criteria outlined below are followed.

1. You must also obtain permission from at least one of the lead authors for each separate work, if you haven't done so already. The author's name and affiliation can be found on the first page of the published Article.

2. For electronic format permissions, Requestor agrees to provide a hyperlink from the reprinted APS material using the source material's DOI on the web page where the work appears. The hyperlink should use the standard DOI resolution URL, http://dx.doi.org/{DOI}. The hyperlink may be embedded in the copyright credit line.

3. For print format permissions, Requestor agrees to print the required copyright credit line on the first page where the material appears: "Reprinted (abstract/excerpt/figure) with permission from [(FULL REFERENCE CITATION) as follows: Author's Names, APS Journal Title, Volume Number, Page Number and Year of Publication.] Copyright (YEAR) by the American Physical Society."

4. Permission granted in this license is for a one-time use and does not include permission for any future editions, updates, databases, formats or other matters. Permission must be sought for any additional use.
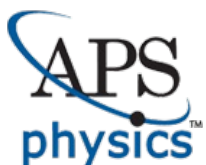
5. Use of the material does not and must not imply any endorsement by APS.

6. APS does not imply, purport or intend to grant permission to reuse materials to which it does not hold copyright. It is the requestor's sole responsibility to ensure the licensed material is original to APS and does not contain the copyright of another entity, and that the copyright notice of the figure, photograph, cover or table does not indicate it was reprinted by APS with permission from another source.

7. The permission granted herein is personal to the Requestor for the use specified and is not transferable or assignable without express written permission of APS. This license may not be amended except in writing by APS.

8. You may not alter, edit or modify the material in any manner.

9. You may translate the materials only when translation rights have been granted.

10. APS is not responsible for any errors or omissions due to translation.

11. You may not use the material for promotional, sales, advertising or marketing purposes.

12. The foregoing license shall not take effect unless and until APS or its agent, Aptara, receives payment in full in accordance with Aptara Billing and Payment Terms and Conditions, which are incorporated herein by reference.

13. Should the terms of this license be violated at any time, APS or Aptara may revoke the license with no refund to you and seek relief to the fullest extent of the laws of the USA. Official written notice will be made using the contact information provided with the permission request. Failure to receive such notice will not nullify revocation of the permission.

14. APS reserves all rights not specifically granted herein.

15. This document, including the Aptara Billing and Payment Terms and Conditions, shall be the entire agreement between the parties relating to the subject matter hereof.

American Physical Society
Reuse and Permissions License

21-Jul-2020

This license agreement between the American Physical Society ("APS") and Martin Graham ("You") consists of your license details and the terms and conditions provided by the American Physical Society and SciPris.

Licensed Content Information

License Number:	RNP/20/JUL/028593
License date:	21-Jul-2020
DOI:	10.1103/PhysRevB.96.184501
Title:	Imaging the spatial form of a superconducting order parameter via Josephson scanning tunneling spectroscopy
Author:	Martin Graham and Dirk K. Morr
Publication:	Physical Review B
Publisher:	American Physical Society
Cost:	USD $ 0.00

Request Details

Does your reuse require significant modifications: No

Specify intended distribution locations:	United States
Reuse Category:	Reuse in a thesis/dissertation
Requestor Type:	Author of requested content
Items for Reuse:	Whole Article
Format for Reuse:	Electronic

Information about New Publication:

University/Publisher:	University of Illinois at Chicago
Title of dissertation/thesis:	Imaging Novel States in Unconventional Superconductors
Author(s):	Martin Graham
Expected completion date:	Jul. 2020

License Requestor Information

Name:	Martin Graham
Affiliation:	Individual
Email Id:	graham40@uic.edu
Country:	United States

American Physical Society
Reuse and Permissions License

TERMS AND CONDITIONS

The American Physical Society (APS) is pleased to grant the Requestor of this license a non-exclusive, non-transferable permission, limited to Electronic format, provided all criteria outlined below are followed.

1. You must also obtain permission from at least one of the lead authors for each separate work, if you haven't done so already. The author's name and affiliation can be found on the first page of the published Article.

2. For electronic format permissions, Requestor agrees to provide a hyperlink from the reprinted APS material using the source material's DOI on the web page where the work appears. The hyperlink should use the standard DOI resolution URL, http://dx.doi.org/{DOI}. The hyperlink may be embedded in the copyright credit line.

3. For print format permissions, Requestor agrees to print the required copyright credit line on the first page where the material appears: "Reprinted (abstract/excerpt/figure) with permission from [(FULL REFERENCE CITATION) as follows: Author's Names, APS Journal Title, Volume Number, Page Number and Year of Publication.] Copyright (YEAR) by the American Physical Society."

4. Permission granted in this license is for a one-time use and does not include permission for any future editions, updates, databases, formats or other matters. Permission must be sought for any additional use.

5. Use of the material does not and must not imply any endorsement by APS.

6. APS does not imply, purport or intend to grant permission to reuse materials to which it does not hold copyright. It is the requestor's sole responsibility to ensure the licensed material is original to APS and does not contain the copyright of another entity, and that the copyright notice of the figure, photograph, cover or table does not indicate it was reprinted by APS with permission from another source.

7. The permission granted herein is personal to the Requestor for the use specified and is not transferable or assignable without express written permission of APS. This license may not be amended except in writing by APS.

8. You may not alter, edit or modify the material in any manner.

9. You may translate the materials only when translation rights have been granted.

10. APS is not responsible for any errors or omissions due to translation.

11. You may not use the material for promotional, sales, advertising or marketing purposes.

12. The foregoing license shall not take effect unless and until APS or its agent, Aptara, receives payment in full in accordance with Aptara Billing and Payment Terms and Conditions, which are incorporated herein by reference.

13. Should the terms of this license be violated at any time, APS or Aptara may revoke the license with no refund to you and seek relief to the fullest extent of the laws of the USA. Official written notice will be made using the contact information provided with the permission request. Failure to receive such notice will not nullify revocation of the permission.

14. APS reserves all rights not specifically granted herein.

15. This document, including the Aptara Billing and Payment Terms and Conditions, shall be the entire agreement between the parties relating to the subject matter hereof.

THE AMERICAN ASSOCIATION FOR THE ADVANCEMENT OF SCIENCE LICENSE TERMS AND CONDITIONS

Jul 21, 2020

This Agreement between Martin Graham ("You") and The American Association for the Advancement of Science ("The American Association for the Advancement of Science") consists of your license details and the terms and conditions provided by The American Association for the Advancement of Science and Copyright Clearance Center.

License Number	4873831117914
License date	Jul 21, 2020
Licensed Content Publisher	The American Association for the Advancement of Science
Licensed Content Publication	Science
Licensed Content Title	Evidence for dispersing 1D Majorana channels in an iron-based superconductor
Licensed Content Author	Zhenyu Wang,Jorge Olivares Rodriguez,Lin Jiao,Sean Howard,Martin Graham,G. D. Gu,Taylor L. Hughes,Dirk K. Morr,Vidya Madhavan
Licensed Content Date	Jan 3, 2020
Licensed Content Volume	367
Licensed Content Issue	6473

Volume number	367
Issue number	6473
Type of Use	Thesis / Dissertation
Requestor type	Author of the AAAS published paper
Format	Print and electronic
Portion	Full Text
Title	Imaging Novel States in Unconventional Superconductors
Institution name	University of Illinois at Chicago
Expected presentation date	Jul 2020
Order reference number	1
Requestor Location	Martin Graham 1448 W. Lexington St Unit 1 CHICAGO, IL 60607 United States Attn: Martin Graham
Total	0.00 USD

Terms and Conditions

American Association for the Advancement of Science TERMS AND CONDITIONS

Regarding your request, we are pleased to grant you non-exclusive, non-transferable permission, to republish the AAAS material identified above in your work identified above,

subject to the terms and conditions herein. We must be contacted for permission for any uses other than those specifically identified in your request above.

The following credit line must be printed along with the AAAS material: "From [Full Reference Citation]. Reprinted with permission from AAAS."

All required credit lines and notices must be visible any time a user accesses any part of the AAAS material and must appear on any printed copies and authorized user might make.

This permission does not apply to figures / photos / artwork or any other content or materials included in your work that are credited to non-AAAS sources. If the requested material is sourced to or references non-AAAS sources, you must obtain authorization from that source as well before using that material. You agree to hold harmless and indemnify AAAS against any claims arising from your use of any content in your work that is credited to non-AAAS sources.

If the AAAS material covered by this permission was published in Science during the years 1974 - 1994, you must also obtain permission from the author, who may grant or withhold permission, and who may or may not charge a fee if permission is granted. See original article for author's address. This condition does not apply to news articles.

The AAAS material may not be modified or altered except that figures and tables may be modified with permission from the author. Author permission for any such changes must be secured prior to your use.

Whenever possible, we ask that electronic uses of the AAAS material permitted herein include a hyperlink to the original work on AAAS's website (hyperlink may be embedded in the reference citation).

AAAS material reproduced in your work identified herein must not account for more than 30% of the total contents of that work.

AAAS must publish the full paper prior to use of any text.

AAAS material must not imply any endorsement by the American Association for the Advancement of Science.

This permission is not valid for the use of the AAAS and/or Science logos.

AAAS makes no representations or warranties as to the accuracy of any information contained in the AAAS material covered by this permission, including any warranties of

merchantability or fitness for a particular purpose.

If permission fees for this use are waived, please note that AAAS reserves the right to charge for reproduction of this material in the future.

Permission is not valid unless payment is received within sixty (60) days of the issuance of this permission. If payment is not received within this time period then all rights granted herein shall be revoked and this permission will be considered null and void.

In the event of breach of any of the terms and conditions herein or any of CCC's Billing and Payment terms and conditions, all rights granted herein shall be revoked and this permission

will be considered null and void.

AAAS reserves the right to terminate this permission and all rights granted herein at its discretion, for any purpose, at any time. In the event that AAAS elects to terminate this permission, you will have no further right to publish, publicly perform, publicly display, distribute or otherwise use any matter in which the AAAS content had been included, and all fees paid hereunder shall be fully refunded to you. Notification of termination will be sent to the contact information as supplied by you during the request process and termination shall be immediate upon sending the notice. Neither AAAS nor CCC shall be liable for any costs, expenses, or damages you may incur as a result of the termination of this permission, beyond the refund noted above.

This Permission may not be amended except by written document signed by both parties.

The terms above are applicable to all permissions granted for the use of AAAS material. Below you will find additional conditions that apply to your particular type of use.

FOR A THESIS OR DISSERTATION
If you are using figure(s)/table(s), permission is granted for use in print and electronic versions of your dissertation or thesis. A full text article may be used in print versions only of a dissertation or thesis.

Permission covers the distribution of your dissertation or thesis on demand by ProQuest / UMI, provided the AAAS material covered by this permission remains in situ.

If you are an Original Author on the AAAS article being reproduced, please refer to your License to Publish for rules on reproducing your paper in a dissertation or thesis.

FOR JOURNALS:
Permission covers both print and electronic versions of your journal article, however the AAAS material may not be used in any manner other than within the context of your article.

FOR BOOKS/TEXTBOOKS:
If this license is to reuse figures/tables, then permission is granted for non-exclusive world rights in all languages in both print and electronic formats (electronic formats are defined below).

If this license is to reuse a text excerpt or a full text article, then permission is granted for non-exclusive world rights in English only. You have the option of securing either print or electronic rights or both, but electronic rights are not automatically granted and do garner additional fees. Permission for translations of text excerpts or full text articles into other languages must be obtained separately.

Licenses granted for use of AAAS material in electronic format books/textbooks are valid only in cases where the electronic version is equivalent to or substitutes for the print version of the book/textbook. The AAAS material reproduced as permitted herein must remain in situ and must not be exploited separately (for example, if permission covers the use of a full text article, the article may not be offered for access or for purchase as a stand-alone unit), except in the case of permitted textbook companions as noted below.

You must include the following notice in any electronic versions, either adjacent to the reprinted AAAS material or in the terms and conditions for use of your electronic products: "Readers may view, browse, and/or download material for temporary copying purposes only,

provided these uses are for noncommercial personal purposes. Except as provided by law, this material may not be further reproduced, distributed, transmitted, modified, adapted, performed, displayed, published, or sold in whole or in part, without prior written permission from the publisher."

If your book is an academic textbook, permission covers the following companions to your textbook, provided such companions are distributed only in conjunction with your textbook at no additional cost to the user:

- Password-protected website
- Instructor's image CD/DVD and/or PowerPoint resource
- Student CD/DVD

All companions must contain instructions to users that the AAAS material may be used for non-commercial, classroom purposes only. Any other uses require the prior written permission from AAAS.

If your license is for the use of AAAS Figures/Tables, then the electronic rights granted herein permit use of the Licensed Material in any Custom Databases that you distribute the electronic versions of your textbook through, so long as the Licensed Material remains within the context of a chapter of the title identified in your request and cannot be downloaded by a user as an independent image file.

Rights also extend to copies/files of your Work (as described above) that you are required to provide for use by the visually and/or print disabled in compliance with state and federal laws.

This permission only covers a single edition of your work as identified in your request.

FOR NEWSLETTERS:
Permission covers print and/or electronic versions, provided the AAAS material reproduced as permitted herein remains in situ and is not exploited separately (for example, if permission covers the use of a full text article, the article may not be offered for access or for purchase as a stand-alone unit)

FOR ANNUAL REPORTS:
Permission covers print and electronic versions provided the AAAS material reproduced as permitted herein remains in situ and is not exploited separately (for example, if permission covers the use of a full text article, the article may not be offered for access or for purchase as a stand-alone unit)

FOR PROMOTIONAL/MARKETING USES:
Permission covers the use of AAAS material in promotional or marketing pieces such as information packets, media kits, product slide kits, brochures, or flyers limited to a single print run. The AAAS Material may not be used in any manner which implies endorsement or promotion by the American Association for the Advancement of Science (AAAS) or Science of any product or service. AAAS does not permit the reproduction of its name, logo or text on promotional literature.

If permission to use a full text article is permitted, The Science article covered by this permission must not be altered in any way. No additional printing may be set onto an article

copy other than the copyright credit line required above. Any alterations must be approved in advance and in writing by AAAS. This includes, but is not limited to, the placement of sponsorship identifiers, trademarks, logos, rubber stamping or self-adhesive stickers onto the article copies.

Additionally, article copies must be a freestanding part of any information package (i.e. media kit) into which they are inserted. They may not be physically attached to anything, such as an advertising insert, or have anything attached to them, such as a sample product. Article copies must be easily removable from any kits or informational packages in which they are used. The only exception is that article copies may be inserted into three-ring binders.

FOR CORPORATE INTERNAL USE:
The AAAS material covered by this permission may not be altered in any way. No additional printing may be set onto an article copy other than the required credit line. Any alterations must be approved in advance and in writing by AAAS. This includes, but is not limited to the placement of sponsorship identifiers, trademarks, logos, rubber stamping or self-adhesive stickers onto article copies.

If you are making article copies, copies are restricted to the number indicated in your request and must be distributed only to internal employees for internal use.

If you are using AAAS Material in Presentation Slides, the required credit line must be visible on the slide where the AAAS material will be reprinted

If you are using AAAS Material on a CD, DVD, Flash Drive, or the World Wide Web, you must include the following notice in any electronic versions, either adjacent to the reprinted AAAS material or in the terms and conditions for use of your electronic products: "Readers may view, browse, and/or download material for temporary copying purposes only, provided these uses are for noncommercial personal purposes. Except as provided by law, this material may not be further reproduced, distributed, transmitted, modified, adapted, performed, displayed, published, or sold in whole or in part, without prior written permission from the publisher." Access to any such CD, DVD, Flash Drive or Web page must be restricted to your organization's employees only.

FOR CME COURSE and SCIENTIFIC SOCIETY MEETINGS:
Permission is restricted to the particular Course, Seminar, Conference, or Meeting indicated in your request. If this license covers a text excerpt or a Full Text Article, access to the reprinted AAAS material must be restricted to attendees of your event only (if you have been granted electronic rights for use of a full text article on your website, your website must be password protected, or access restricted so that only attendees can access the content on your site).

If you are using AAAS Material on a CD, DVD, Flash Drive, or the World Wide Web, you must include the following notice in any electronic versions, either adjacent to the reprinted AAAS material or in the terms and conditions for use of your electronic products: "Readers may view, browse, and/or download material for temporary copying purposes only, provided these uses are for noncommercial personal purposes. Except as provided by law, this material may not be further reproduced, distributed, transmitted, modified, adapted, performed, displayed, published, or sold in whole or in part, without prior written permission from the publisher."

FOR POLICY REPORTS:

These rights are granted only to non-profit organizations and/or government agencies. Permission covers print and electronic versions of a report, provided the required credit line appears in both versions and provided the AAAS material reproduced as permitted herein remains in situ and is not exploited separately.

FOR CLASSROOM PHOTOCOPIES:

Permission covers distribution in print copy format only. Article copies must be freestanding and not part of a course pack. They may not be physically attached to anything or have anything attached to them.

FOR COURSEPACKS OR COURSE WEBSITES:

These rights cover use of the AAAS material in one class at one institution. Permission is valid only for a single semester after which the AAAS material must be removed from the Electronic Course website, unless new permission is obtained for an additional semester. If the material is to be distributed online, access must be restricted to students and instructors enrolled in that particular course by some means of password or access control.

FOR WEBSITES:

You must include the following notice in any electronic versions, either adjacent to the reprinted AAAS material or in the terms and conditions for use of your electronic products: "Readers may view, browse, and/or download material for temporary copying purposes only, provided these uses are for noncommercial personal purposes. Except as provided by law, this material may not be further reproduced, distributed, transmitted, modified, adapted, performed, displayed, published, or sold in whole or in part, without prior written permission from the publisher."

Permissions for the use of Full Text articles on third party websites are granted on a case by case basis and only in cases where access to the AAAS Material is restricted by some means of password or access control. Alternately, an E-Print may be purchased through our reprints department (brocheleau@rockwaterinc.com).

REGARDING FULL TEXT ARTICLE USE ON THE WORLD WIDE WEB IF YOU ARE AN 'ORIGINAL AUTHOR' OF A SCIENCE PAPER

If you chose "Original Author" as the Requestor Type, you are warranting that you are one of authors listed on the License Agreement as a "Licensed content author" or that you are acting on that author's behalf to use the Licensed content in a new work that one of the authors listed on the License Agreement as a "Licensed content author" has written.

Original Authors may post the 'Accepted Version' of their full text article on their personal or on their University website and not on any other website. The 'Accepted Version' is the version of the paper accepted for publication by AAAS including changes resulting from peer review but prior to AAAS's copy editing and production (in other words not the AAAS published version).

FOR MOVIES / FILM / TELEVISION:

Permission is granted to use, record, film, photograph, and/or tape the AAAS material in connection with your program/film and in any medium your program/film may be shown or heard, including but not limited to broadcast and cable television, radio, print, world wide web, and videocassette.

The required credit line should run in the program/film's end credits.

FOR MUSEUM EXHIBITIONS:
Permission is granted to use the AAAS material as part of a single exhibition for the duration of that exhibit. Permission for use of the material in promotional materials for the exhibit must be cleared separately with AAAS (please contact us at permissions@aaas.org).

FOR TRANSLATIONS:
Translation rights apply only to the language identified in your request summary above.

The following disclaimer must appear with your translation, on the first page of the article, after the credit line: "This translation is not an official translation by AAAS staff, nor is it endorsed by AAAS as accurate. In crucial matters, please refer to the official English-language version originally published by AAAS."

FOR USE ON A COVER:
Permission is granted to use the AAAS material on the cover of a journal issue, newsletter issue, book, textbook, or annual report in print and electronic formats provided the AAAS material reproduced as permitted herein remains in situ and is not exploited separately

By using the AAAS Material identified in your request, you agree to abide by all the terms and conditions herein.

Questions about these terms can be directed to the AAAS Permissions department permissions@aaas.org.

Other Terms and Conditions:

v 2

Questions? customercare@copyright.com or +1-855-239-3415 (toll free in the US) or +1-978-646-2777.

Bibliography

[1] Hirschfeld, P. J., M. M. Korshunov, and I. I. Mazin (2011, oct). Gap symmetry and structure of fe-based superconductors. *Reports on Progress in Physics 74*(12), 124508.

[2] Wollman, D. A., D. J. Van Harlingen, W. C. Lee, D. M. Ginsberg, and A. J. Leggett (1993). Experimental determination of the superconducting pairing state in YBCO from the phase coherence of YBCO-Pb dc SQUIDs. *Physical Review Letters 71*(13), 2134–2137.

[3] Josephson, B. D. (1962). Possible new effects in superconductive tunnelling. *Physics Letters 1*(7), 251–253.

[4] Bardeen, J., L. N. Cooper, and J. R. Schrieffer (1957, Apr). Microscopic theory of superconductivity. *Phys. Rev. 106*, 162–164.

[5] Tinkham, M. (2004). *Introduction to Superconductivity*. Dover Books on Physics Series. Dover Publications.

[6] Edkins, S. (2017). *Visualising the Charge and Cooper-Pair Density Waves in Cuprates*. Springer Theses. Springer International Publishing.

[7] Hamidian, M. H., S. D. Edkins, S. H. Joo, A. Kostin, H. Eisaki, S. Uchida, M. J. Lawler, E. A. Kim, A. P. Mackenzie, K. Fujita, J. Lee, and J. C. Davis (2016). De-

tection of a Cooper-pair density wave in Bi2Sr2CaCu2O8+x. *Nature 532*(7599), 343–347.

[8] Cho, D., K. M. Bastiaans, D. Chatzopoulos, G. D. Gu, and M. P. Allan (2019). A strongly inhomogeneous superfluid in an iron-based superconductor. *Nature 571*(7766), 541–545.

[9] Lang, K. M., V. Madhavan, J. E. Hoffman, E. W. Hudson, H. Eisaki, S. Uchida, and J. C. Davis (2002). Imaging the granular structure of high-Tc superconductivity in underdoped Bi2Sr2CaCu2O8+delta. *Nature 415*(6870), 412–416.

[10] Flatté, M. E. and J. M. Byers (1997, Nov). Local electronic structure of defects in superconductors. *Phys. Rev. B 56*, 11213–11231.

[11] Yang, K. and D. F. Agterberg (2000, May). Josephson effect in fulde-ferrell-larkin-ovchinnikov superconductors. *Phys. Rev. Lett. 84*, 4970–4973.

[12] Tanaka, Y. and S. Kashiwaya (1997, Jul). Theory of josephson effects in anisotropic superconductors. *Phys. Rev. B 56*, 892–912.

[13] Fulde, P. and R. A. Ferrell (1964). Superconductivity in a strong spin-exchange field. *Physical Review 135*(3A).

[14] Larkin, A. and Y. N. Ovchinnikov (1965). Zh. é ksp. teor. fiz. 47, 1136 1964 sov. phys. *JETP 20*, 762.

[15] Sato, M. and Y. Ando (2017, May). Topological superconductors: a review. *Reports on Progress in Physics 80*(7), 076501.

[16] Tanaka, Y., M. Sato, and N. Nagaosa (2012, Jan). Symmetry and topology in superconductors –odd-frequency pairing and edge states–. *Journal of the Physical Society of Japan 81*(1), 011013.

[17] Kitaev, A. Y. (2001). Unpaired Majorana fermions in quantum wires. *Physics-Uspekhi 44*(10S), 131–136.

[18] Chen, L., H. Liu, C. Jiang, C. Shi, D. Wang, G. Cui, X. Li, and Q. Zhuang (2019). Topological edge states in high-temperature superconductiving FeSe/SrTiO3 films with Te substitution. *Scientific Reports 9*(1), 4154.

[19] Graser, S., T. A. Maier, P. J. Hirschfeld, and D. J. Scalapino (2009). Near-degeneracy of several pairing channels in multiorbital models for the Fe pnictides. *New Journal of Physics 11*.

[20] Sarkar, S., J. Van Dyke, P. O. Sprau, F. Massee, U. Welp, W. K. Kwok, J. C. Davis, and D. K. Morr (2017). Orbital superconductivity, defects, and pinned nematic fluctuations in the doped iron chalcogenide FeSe0.45Te0.55. *Physical Review B 96*(6), 060504.

[21] Ambegaokar, V. and A. Baratoff (1963a). Tunneling between superconductors. *Physical Review Letters 11*(2), 104.

[22] Ambegaokar, V. and A. Baratoff (1963b). Tunneling Between Superconductors Errata. *11*(2), 1963.

[23] Randeria, M. T., B. E. Feldman, I. K. Drozdov, and A. Yazdani (2016). Scanning Josephson spectroscopy on the atomic scale. *Physical Review B - Condensed Matter and Materials Physics 93*(16), 1–5.

[24] Naaman, O., W. Teizer, and R. C. Dynes (2001). Fluctuation Dominated Josephson Tunneling with a Scanning Tunneling Microscope. *Physical Review Letters 87*(9), 097004.

[25] Suderow, H., I. Guillamón, J. G. Rodrigo, and S. Vieira (2014, may). Imaging

superconducting vortex cores and lattices with a scanning tunneling microscope. *Superconductor Science and Technology 27*(6), 063001.

[26] Rodrigo, J. G., H. Suderow, and S. Vieira (2004). On the use of STM superconducting tips at very low temperatures. *European Physical Journal B 40*(4), 483–488.

[27] Jäck, B., M. Eltschka, M. Assig, M. Etzkorn, C. R. Ast, and K. Kern (2016). Critical Josephson current in the dynamical Coulomb blockade regime. *Physical Review B 93*(2), 1–5.

[28] Balatsky, A. V., I. Vekhter, and J. X. Zhu (2006). Impurity-induced states in conventional and unconventional superconductors. *Reviews of Modern Physics 78*(2), 373–433.

[29] Cuevas, J., a. Martín-Rodero, and a. Yeyati (1996). Hamiltonian approach to the transport properties of superconducting quantum point contacts. *Physical Review B 54*(10), 7366–7379.

[30] Keldysh, L. Diagram Technique for nonequilibrium processes.

[31] Rammer, J. and H. Smith (1986, Apr). Quantum field-theoretical methods in transport theory of metals. *Rev. Mod. Phys. 58*, 323–359.

[32] Shiba, H. (1968). Classical Spins in Superconductors. *40*(3).

[33] Yazdani, A., B. A. Jones, C. P. Lutz, M. F. Crommie, and D. M. Eigler (1997). Probing the local effects of magnetic impurities on superconductivity. *Science 275*(5307), 1767–1770.

[34] Hatter, N., B. W. Heinrich, M. Ruby, J. I. Pascual, and K. J. Franke (2015). Magnetic anisotropy in Shiba bound states across a quantum phase transition. *Nature Communications 6*.

[35] Sakurai, A. (1970). Comment on SupeFconductoll with Magnetic Impuritie. *Progress of Theoretical Physics 44*(6).

[36] Salkola, M. I., a. V. Balatsky, and J. R. Schrieffer (1997). Spectral properties of quasiparticle excitations induced by magnetic moments in superconductors. *Physical Review B 55*(18), 12648–12661.

[37] Morr, D. K. and J. Yoon (2006). Impurities, quantum interference, and quantum phase transitions in s -wave superconductors. *Physical Review B - Condensed Matter and Materials Physics 73*(22), 1–11.

[38] Anderson, P. W. (1959). Theory of dirty superconductors. *Journal of Physics and Chemistry of Solids 11*(1-2), 26–30.

[39] Kimura, H., R. P. Barber, S. Ono, Y. Ando, and R. C. Dynes (2009). Josephson scanning tunneling microscopy: A local and direct probe of the superconducting order parameter. *Physical Review B - Condensed Matter and Materials Physics 80*(14), 1–16.

[40] Bianchi, A., R. Movshovich, C. Capan, P. G. Pagliuso, and J. L. Sarrao (2003). Possible fulde-ferrell-larkin-ovchinnikov superconducting state in [formula presented]. *Physical Review Letters 91*(18), 16–19.

[41] Radovan, H. A., N. A. Fortune, T. P. Murphy, S. T. Hannahs, E. C. Palm, S. W. Tozer, and D. Hall (2003). Magnetic enhancement of superconductivity from electron spin domains. *Nature 425*(6953), 51–55.

[42] Matsuda, Y. and H. Shimahara (2007). Fulde-Ferrell-Larkin-Ovchinnikov state in heavy fermion superconductors. *Journal of the Physical Society of Japan 76*(5), 1–16.

[43] Šmakov, J., I. Martin, and A. V. Balatsky (2001). Josephson scanning tunneling microscopy. *Physical Review B 64*(21), 212506.

[44] Bergeal, N., Y. Noat, T. Cren, T. Proslier, V. Dubost, F. Debontridder, A. Zimmers, D. Roditchev, W. Sacks, and J. Marcus (2008). Mapping the superconducting condensate surrounding a vortex in superconducting V3Si using a superconducting MgB2 tip in a scanning tunneling microscope. *Physical Review B - Condensed Matter and Materials Physics 78*(14), 1–4.

[45] Jacobs, T., S. O. Katterwe, and V. M. Krasnov (2016). Superconducting correlations above Tc in the pseudogap state of Bi2Sr2CaCu2 O8+δ cuprates revealed by angular-dependent magnetotunneling. *Physical Review B 94*(22), 1–6.

[46] Emery, V. J. and S. A. Kivelson (1995). Importance of phase fluctuations in superconductors with small superfluid density. *Nature 374*(6521), 434–437.

[47] Franz, M. and A. Millis (1998). Phase fluctuations and spectral properties of underdoped cuprates. *Physical Review B - Condensed Matter and Materials Physics 58*(21), 14572–14580.

[48] Chen, Q., J. Stajic, S. Tan, and K. Levin (2005). BCS-BEC crossover: From high temperature superconductors to ultracold superfluids. *Physics Reports 412*(1), 1–88.

[49] Chen, H.-D., O. Vafek, A. Yazdani, and S.-C. Zhang (2004). Pair density wave in the pseudogap state of high temperature superconductors. *Physical review letters 93*(18), 187002.

[50] Berg, E., E. Fradkin, and S. A. Kivelson (2009). Charge-4e superconductivity from pair-density-wave order in certain high-temperature superconductors. *Nature Physics 5*(11), 830–833.

[51] Lee, P. A. (2014). Amperean pairing and the pseudogap phase of cuprate superconductors. *Physical Review X 4*(3), 1–13.

[52] Yanase, Y. and M. Sigrist (2009). Antiferromagnetic Order and π-Triplet Pairing in the Fulde–Ferrell–Larkin–Ovchinnikov State. *Journal of the Physical Society of Japan 78*(11), 114715.

[53] Liu, S. L. and T. Zhou (2012). Phase transition in the Fulde-Ferrell-Larkin-Ovchinnikov states for the d-wave superconductor in the two-dimensional orthorhombic lattice. *Journal of Superconductivity and Novel Magnetism 25*(4), 913–921.

[54] Hudson, E. W., S. H. Pan, A. K. Gupta, K.-W. Ng, and J. C. Davis (1999). Atomic-scale quasi-particle scattering resonances in bi2sr2cacu2o8+δ. *Science 285*(5424), 88–91.

[55] Pan, S. H., E. W. Hudson, K. M. Lang, H. Elsaki, S. Uchida, and J. C. Davis (2000). Imaging the effects of individual zinc impurity atoms on superconductivity in Bi2Sr2CaCu2O(8+δ). *Nature 403*(6771), 746–750.

[56] Balatsky, A. V., M. I. Salkola, and A. Rosengren (1995). Impurity-induced virtual bound states in d-wave superconductors. *Physical Review B 51*(21), 15547–15551.

[57] Salkola, M. I., A. V. Balatsky, and D. J. Scalapino (1996). Theory of scanning tunneling microscopy probe of impurity states in a D-wave superconductor. *Physical Review Letters 77*(9), 1841–1844.

[58] Hudson, E. W., K. M. Lang, V. Madhavan, S. H. Pan, H. Eisaki, S. Uchida, and J. C. Davis (2001). Interplay of magnetism and high-Tc superconductivity at individual Ni impurity atoms in Bi2Sr2CaCu2O8+δ. *Nature 411*(6840), 920–924.

[59] Allan, M. P., F. Massee, D. K. Morr, J. Van Dyke, A. W. Rost, A. P. Mackenzie, C. Petrovic, and J. C. Davis (2013). Imaging Cooper pairing of heavy fermions in CeCoIn 5. *Nature Physics 9*(8), 468–473.

[60] Van Dyke, J. S., F. Massee, M. P. Allan, J. C. S. Davis, C. Petrovic, and D. K. Morr (2014). Direct evidence for a magnetic f-electron-mediated pairing mechanism of heavy-fermion superconductivity in CeCoIn5. *Proceedings of the National Academy of Sciences 111*(32), 11663–11667.

[61] Vorontsov, A. B., J. A. Sauls, and M. J. Graf (2005). Phase diagram and spectroscopy of Fulde-Ferrell-Larkin-Ovchinnikov states of two-dimensional d-wave superconductors. *Physical Review B - Condensed Matter and Materials Physics 72*(18), 1–9.

[62] Wulin, D., Y. He, C. C. Chien, D. K. Morr, and K. Levin (2009). Model for the temperature dependence of the quasiparticle interference pattern in the measured scanning tunneling spectra of underdoped cuprate superconductors. *Physical Review B - Condensed Matter and Materials Physics 80*(13), 1–5.

[63] Howald, C., A. Kapitulnik, and P. Fournier (2001). Inherent inhomogeneities in tunneling spectra of (formula presented) crystals in the superconducting state. *Physical Review B - Condensed Matter and Materials Physics 64*(10), 2–5.

[64] Schmidt, A. R., K. Fujita, E. A. Kim, M. J. Lawler, H. Eisaki, S. Uchida, D. H. Lee, and J. C. Davis (2011). Electronic structure of the cuprate superconducting and pseudogap phases from spectroscopic imaging STM. *New Journal of Physics 13*.

[65] Mascot, E., J. Bedow, M. Graham, S. Rachel, and D. K. Morr (2020, April). Topological Superconductivity in Skyrmion Lattices. *arXiv e-prints*, arXiv:2005.00027.

[66] Nayak, C., S. H. Simon, A. Stern, M. Freedman, and S. Das Sarma (2008). Non-Abelian anyons and topological quantum computation. *Reviews of Modern Physics 80*(3), 1083–1159.

[67] Mourik, V., K. Zuo, S. M. Frolov, S. R. Plissard, E. P. A. M. Bakkers, and L. P. Kouwenhoven (2012, may). Signatures of Majorana Fermions in Hybrid Superconductor-Semiconductor Nanowire Devices. *Science 336*(6084), 1003 LP – 1007.

[68] Nadj-Perge, S., I. K. Drozdov, J. Li, H. Chen, S. Jeon, J. Seo, A. H. MacDonald, B. A. Bernevig, and A. Yazdani (2014). Observation of Majorana fermions in ferromagnetic atomic chains on a superconductor. *Science 346*(6209), 602–607.

[69] Ruby, M., F. Pientka, Y. Peng, F. Von Oppen, B. W. Heinrich, and K. J. Franke (2015). End States and Subgap Structure in Proximity-Coupled Chains of Magnetic Adatoms. *Physical Review Letters 115*(19), 1–5.

[70] Pawlak, R., M. Kisiel, J. A. Klinovaja, T. Meier, S. Kawai, T. Glatzel, D. Loss, and E. Meyer (2016). Probing atomic structure and majorana wavefunctions in mono-atomic fe chains on superconducting Pb surface. *npj Quantum Information 2*(1).

[71] Kim, H., A. Palacio-Morales, T. Posske, L. Rózsa, K. Palotás, L. Szunyogh, M. Thorwart, and R. Wiesendanger (2018). Toward tailoring Majorana bound states in artificially constructed magnetic atom chains on elemental superconductors. *Science Advances 4*(5), 1–7.

[72] Wang, D., L. Kong, P. Fan, H. Chen, S. Zhu, W. Liu, L. Cao, Y. Sun, S. Du, J. Schneeloch, R. Zhong, G. Gu, L. Fu, H. Ding, and H. J. Gao (2018). Evidence

for Majorana bound states in an iron-based superconductor. *Science 362*(6412), 333–335.

[73] Machida, T., Y. Sun, S. Pyon, S. Takeda, Y. Kohsaka, T. Hanaguri, T. Sasagawa, and T. Tamegai (2019). Zero-energy vortex bound state in the superconducting topological surface state of Fe(Se,Te). *Nature Materials 18*(8), 811–815.

[74] Ménard, G. C., A. Mesaros, C. Brun, F. Debontridder, D. Roditchev, P. Simon, and T. Cren (2019). Isolated pairs of Majorana zero modes in a disordered superconducting lead monolayer. *Nature Communications 10*(1), 1–7.

[75] Ménard, G. C., S. Guissart, C. Brun, R. T. Leriche, M. Trif, F. Debontridder, D. Demaille, D. Roditchev, P. Simon, and T. Cren (2017). Two-dimensional topological superconductivity in Pb/Co/Si(111). *Nature Communications 8*(1), 1–6.

[76] Palacio-Morales, A., E. Mascot, S. Cocklin, H. Kim, S. Rachel, D. K. Morr, and R. Wiesendanger (2019). Atomic-scale interface engineering of Majorana edge modes in a 2D magnet-superconductor hybrid system. *Science Advances 5*(7), 1–8.

[77] Wang, Z., J. O. Rodriguez, L. Jiao, S. Howard, M. Graham, G. D. Gu, T. L. Hughes, D. K. Morr, and V. Madhavan (2020). Evidence for dispersing 1D Majorana channels in an iron-based superconductor. *Science 367*(6473), 104–108.

[78] Röntynen, J. and T. Ojanen (2015). Topological Superconductivity and High Chern Numbers in 2D Ferromagnetic Shiba Lattices. *Physical Review Letters 114*(23), 1–5.

[79] Li, J., T. Neupert, Z. Wang, A. H. Macdonald, A. Yazdani, and B. Andrei Bernevig (2016). Two-dimensional chiral topological superconductivity in Shiba lattices. *Nature Communications 7*, 1–7.

[80] Rachel, S., E. Mascot, S. Cocklin, M. Vojta, and D. K. Morr (2017). Quantized charge transport in chiral Majorana edge modes. *Physical Review B 96*(20), 1–11.

[81] Romming, N., A. Kubetzka, C. Hanneken, K. Von Bergmann, and R. Wiesendanger (2015). Field-dependent size and shape of single magnetic Skyrmions. *Physical Review Letters 114*(17), 1–5.

[82] Yang, G., P. Stano, J. Klinovaja, and D. Loss (2016). Majorana bound states in magnetic skyrmions. *Physical Review B 93*(22), 1–8.

[83] Garnier, M., A. Mesaros, and P. Simon (2019). Topological superconductivity with deformable magnetic skyrmions. *Communications Physics 2*(1), 1–8.

[84] Ryu, S., A. P. Schnyder, A. Furusaki, and A. W. Ludwig (2010). Topological insulators and superconductors: Tenfold way and dimensional hierarchy. *New Journal of Physics 12*.

[85] Mascot, E., S. Cocklin, S. Rachel, and D. K. Morr (2019). Dimensional tuning of Majorana fermions and real space counting of the Chern number. *Physical Review B 100*(18), 1–7.

[86] Bianco, R. and R. Resta (2011). Mapping topological order in coordinate space. *Physical Review B - Condensed Matter and Materials Physics 84*(24), 4–7.

[87] Prodan, E. (2011, feb). Disordered topological insulators: a non-commutative geometry perspective. *Journal of Physics A: Mathematical and Theoretical 44*(11), 113001.

[88] Prodan, E. (2016, nov). A Computational Non-Commutative Geometry Program for Disordered Topological Insulators.

[89] Chen, W. and A. P. Schnyder (2015).   Majorana edge states in superconductor-noncollinear magnet interfaces. *Physical Review B - Condensed Matter and Materials Physics 92*(21), 1–5.

[90] Graham, M. and D. K. Morr (2017). Imaging the spatial form of a superconducting order parameter via Josephson scanning tunneling spectroscopy. *Physical Review B 96*(18), 1–7.

[91] Graham, M. and D. K. Morr (2019, Jul). Josephson scanning tunneling spectroscopy in $d_{x^2-y^2}$-wave superconductors: A probe for the nature of the pseudogap in the cuprate superconductors. *Phys. Rev. Lett. 123*, 017001.

[92] Zhang, P., K. Yaji, T. Hashimoto, Y. Ota, T. Kondo, K. Okazaki, Z. Wang, J. Wen, G. D. Gu, H. Ding, and S. Shin (2018). Observation of topological superconductivity on the surface of an iron-based superconductor. *Science 360*(6385), 182–186.

[93] Mele, P. (2012, oct). Superconducting properties of iron chalcogenide thin films. *Science and Technology of Advanced Materials 13*(5), 054301.

[94] Horigane, K., N. Takeshita, C.-H. Lee, H. Hiraka, and K. Yamada (2009). First investigation of pressure effects on transition from superconductive to metallic phase in fese0.5te0.5. *Journal of the Physical Society of Japan 78*(6), 063705.

[95] Hu, J. (2013, Jul). Iron-based superconductors as odd-parity superconductors. *Phys. Rev. X 3*, 031004.

[96] Fu, L. and C. L. Kane (2008, Mar). Superconducting proximity effect and majorana fermions at the surface of a topological insulator. *Phys. Rev. Lett. 100*, 096407.

[97] Hao, N. and J. Hu (2014, Jan). Odd parity pairing and nodeless antiphase $s^{\pm}$ in iron-based superconductors. *Phys. Rev. B 89*, 045144.

[98] Zhang, R.-X., W. S. Cole, and S. Das Sarma (2019, May). Helical hinge majorana modes in iron-based superconductors. *Phys. Rev. Lett. 122*, 187001.

[99] Hanaguri, T., S. Niitaka, K. Kuroki, and H. Takagi (2010). Unconventional s-wave superconductivity in fe(se,te). *Science 328*(5977), 474–476.

[100] Bedow, J., E. Mascot, T. Posske, G. S. Uhrig, R. Wiesendanger, S. Rachel, and D. K. Morr (2020, June). Topological superconductivity induced by a triple-Q magnetic structure. *arXiv e-prints*, arXiv:2006.02039.

[101] Zaki, N., G. Gu, A. M. Tsvelik, C. Wu, and P. D. Johnson (2019, July). Time Reversal Symmetry Breaking in the Fe-Chalcogenide Superconductors. *arXiv e-prints*, arXiv:1907.11602.

[102] Wang, Q., Y. Shen, B. Pan, X. Zhang, K. Ikeuchi, K. Iida, A. D. Christianson, H. C. Walker, D. T. Adroja, M. Abdel-Hafiez, X. Chen, D. A. Chareev, A. N. Vasiliev, and J. Zhao (2016). Magnetic ground state of FeSe. *Nature Communications 7*(1), 12182.

[103] Weiße, A., G. Wellein, A. Alvermann, and H. Fehske (2006). The kernel polynomial method. *Reviews of Modern Physics 78*(1), 275–306.

[104] Spanton, E. M., K. C. Nowack, L. Du, G. Sullivan, R.-R. Du, and K. A. Moler (2014, Jul). Images of edge current in $\mathrm{InAs/GaSb}$ quantum wells. *Phys. Rev. Lett. 113*, 026804.

VITA

NAME: Martin Graham

EDUCATION: Ph.D., Condensed Matter Physics
        University of Illinois at Chicago
            Chicago IL 2020
            Thesis: Imaging Novel States in Unconventional Superconductors
        M.S., Condensed Matter Physics
        Ohio University
            Athens OH 2015
        B.S., Physics
        University of Illinois at Urbana-Champaign
            Urbana IL 2013
            Undergraduate thesis: Adaptive Error Analysis in Diffusion Monte Carlo

PUBLICATIONS: 1. Mascot, E., J. Bedow, M. Graham, S. Rachel, and D. K. Morr (2020, April). Topological Superconductivity in Skyrmion Lattices. *arXiv e-prints* , arXiv:2005.00027.

2. Wang, Z., J. O. Rodriguez, L. Jiao, S. Howard, M. Graham, G. D. Gu, T. L. Hughes, D. K. Morr, and V. Madhavan (2020). Evidence for dispersing 1D Majorana channels in an iron-based superconductor. *Science* 367(6473), 104–108.

3. Graham, M. and D. K. Morr (2019, Jul). Josephson scanning tunneling spectroscopy in $d_{x^2-y^2}$-wave superconductors: A probe for the nature of the pseudogap in the cuprate superconductors. *Phys. Rev. Lett.* 123, 017001.

4. Graham, M. and D. K. Morr (2017). Imaging the spatial form of a superconducting order parameter via Josephson scanning tunneling spectroscopy. *Physical Review B* 96(18), 1–7.

5. Hill, A. D., Nash, J., Graham, M., Hervas, D. & Kwiat, P. G. (2014). Adaptive Optics for Single-Photon Fiber Coupling of Ions. *CLEO: 2014* JW2A.128.

RESEARCH
PRESENTATIONS:

Poster Presentations:

- Imaging the superconducting order parameter using Josephson scanning tunneling spectroscopy, Fine Theoretical Physics Institute, 2019
- Josephson scanning tunneling spectroscopy in $d_{x^2-y^2}$-wave superconductors, International Centre for Theoretical Physics, 2018

Talks:

- Josephson Scanning Tunneling Spectroscopy. UIC Physics Fest 2017

AWARDS AND
HONORS:

Image of Research finalist, University of Illinois at Chicago (2019)

ICTP Conference attendee, International Centre for Theoretical Physics (2018)

Shell Scholar, University of Illinois at Urbana-Champaign (2012)

McCormack Scholar, Illinois Valley Community College (2011)

TEACHING
EXPERIENCE:

University of Illinois at Chicago

Instructor:
- PHYS144 (Calculus-based Physics I)

Lab Instructor:
- PHYS241 (Quantum Physics)
- PHYS142 (Calculus-based Physics II)
- PHYS141 (Calculus-based Physics I)
- PHYS106 (Algebra-based Physics I)
- PHYS109 (Algebra-based Physics II)

Teaching Assistant:
PHYS215 (Computational Physics)
PHYS131 (Algebra-based Physics I)
PHYS141 (Calculus-based Physics I)